Exploring the Microstructure and Bulk Shear Mechanics of Reconstituted Collagen I Gels

Joint Master thesis
MSc. Nanobiology and MSc. Biomedical Engineering

Risa Togo

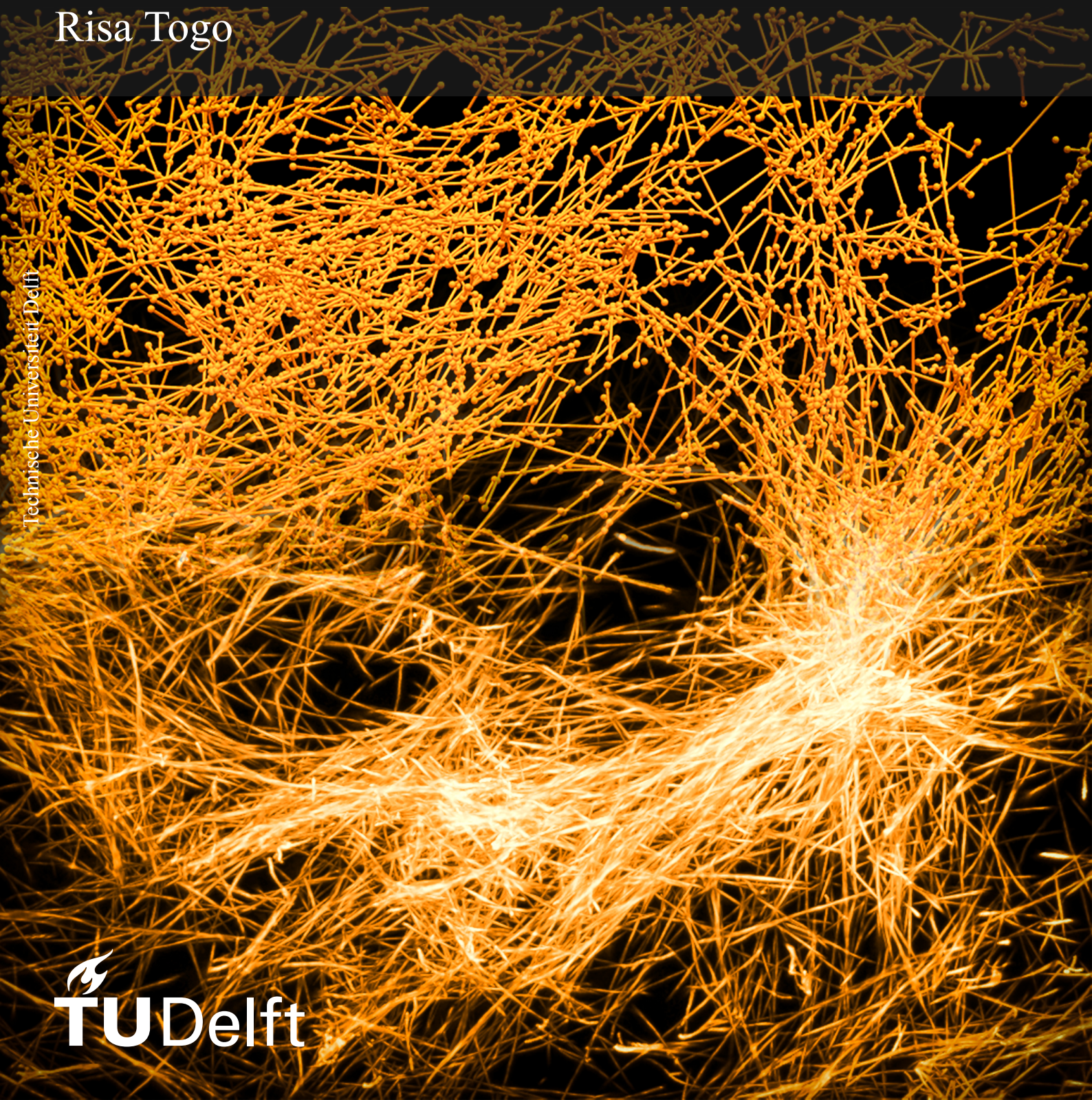

Technische Universiteit Delft

TU Delft

Exploring the Microstructure and Bulk Shear Mechanics of Reconstituted Collagen I Gels

by

Risa Togo

in partial fulfilment of the requirements of

Master of Science Nanobiology
Master of Science Biomedical Engineering,
Track Medical Devices

at the Delft University of Technology,
to be defended publicly on Thursday February 20, 2025 at 11:00.

Student number:	4774310	
Date:	May 2024 – February 2025	
Thesis advisors:	MSc. ir. Sara Cardona,	TU Delft, daily supervisor
	Dr. ir. Irène Nagle,	TU Delft, daily supervisor
	Prof. dr. Gijsje Koenderink,	TU Delft, supervisor
	Prof. dr. ir. Mathias Peirlinck,	TU Delft, supervisor, Chair
	Prof. dr. ir. Behrooz Fereidoonnezhad,	TU Delft, supervisor
	Prof. dr. ir. Sebastien Callens,	TU Eindhoven, supervisor
Thesis commitee:	Prof. dr. Roderick Tas,	TU Delft, external
	Prof. dr. Jos Zwanikken,	TU Delft, external

This thesis is confidential and cannot be made public until February 20, 2026.

TU Delft

Abstract

Collagen networks are key structural components of connective tissues, and their unique mechanical properties are linked to their hierarchical structure. Changes to the network architecture are often associated with altered mechanics and pathological conditions such as fibrosis. While prior works have shown that collagen network topology (i.e. connectivity) dominantly controls the nonlinear elasticity and fracture behavior, network topology is primarily inferred from model fitting to rheological measurements, and it is unknown how the microstructure may influence other aspects of the mechanical behavior. In this thesis, we explore the microstructure and bulk shear mechanics of collagen I networks with a confocal fluorescence microscope and a stress-controlled rheometer. In the first chapter of the thesis, we present ToFiE, a topologically-aware fiber extraction workflow we developed and validate its ability to capture the network connectivity using simulated images of synthetic networks. We successfully apply the ToFiE workflow to real 3D confocal fluorescence images of collagen networks and find a non-monotonic change in the fiber length, the degree of bundling, and the average connectivity of the network at different collagen concentrations and polymerization temperatures. Our findings provide quantitative insights into the different collagen microstructures, and also introduce an automated image analysis tool to extract topology from microscopy images. In the second chapter of the thesis, we investigate the stress-dependent deformation dynamics of collagen networks, an unexplored side of their mechanics. We demonstrate for the first time that collagen networks exhibit two transient peaks in viscosity in the nonlinear elastic regime: one at the onset of stretching-dominated rigidity corresponding to a second order mechanical phase transition, and one at the maximum stiffness. These findings advance our fundamental understanding of their mechanics. Altogether, the thesis establishes a strong foundation for further exploration of the structure and mechanics of collagen networks.

Acknowledgement

The master project evolved into something beyond what I could have imagined just a year ago. I am extremely thankful for the rich experiences I have gained which further confirms my passion for biophysics and research that lies at the interface of physics and engineering. It would not have been possible without the support of my team, and the synergistic collaboration between the Koenderink, Fereidoonnezhad, and Peirlinck Lab. The project and all of the experiments were hosted at the Koenderink Lab. Gijsje, thank you for giving me this open-ended project where I could explore collagen freely, and for your endless trust in my progress, and your understanding and guidance throughout. Thank you Mathias, Behrooz for your support throughout the internship and master project, and your help with navigating the double degree. I am grateful to Fred MacKintosh for the multiple discussions and *critical* suggestions, which significantly helped me in understanding and developing my findings. Sara, since the internship, thank you for your whole-hearted mentorship throughout, and your shared excitement for collagen. The internship was the perfect bridge to the master project, and equipped me with improved research skills to tackle new challenges, the wet lab. Irène, thank you for supporting and advising me every step of the way, whether it was for research, experimental failures, the PhD search, and in general. I am very grateful for your guidance in the wet lab, which helped me to be confident (the rheology room still is, dare I say, the most fascinating room of them all.). Between the last minute experiments and writing sprint, you made sure I was grounded. Sebastien, thank you for your fresh input and enthusiasm for my project in our numerous meetings even after your professorship in Eindhoven started. Margherita, thanks for your help with using the rheoconfocal setup, and for fabricating PDMS molds for me to try out with imaging. Thank you to all the members of the Koenderink lab, it was a joyful experience to work in the lab together and go for workout sessions at X (shoutout to X-plorers). Charu, thank you for your advice on labeling chemistry and for always being open to talk about research in general. Marcos, thanks for your help with various things in the lab. Stein, thanks for all the theoretical and non-theoretical discussions during our coffee breaks, which inspired me in many ways. Lastly, I would like to thank my friends, my brother, and my parents for their never ending encouragement since the start of my academic journey.

Contents

Introduction

Disordered and underconstrained networks are well-studied in the field of soft matter physics for their interesting mechanical properties. These networks exhibit floppy modes under low strains, transitioning to geometric rigidity at higher strains. Their disordered structure provides protection against fracture. Additionally, small changes in the network properties and connectivity can significantly alter their mechanical behavior [1, 2] (Figure 1). Remarkably, these networks also occur in nature: biopolymer networks such as collagen, fibrin, and actin at low crosslinker density are a few examples [3, 4, 5]. Compared to simulations of disordered and underconstrained networks, the biological complexity of collagen's hierarchical structure (fiber bundling, monomer slippage, weak crosslinks) introduces additional mechanical behaviors that are not fully understood. The rich mechanics of collagen make it a popular biomaterial choice for tissue engineering and for 3D *in vitro* cell culture scaffolds. Research has shown that changes in the biophysical properties of the collagen matrix can influence cellular behavior, guiding differentiation and promoting directed cell growth [6, 7]. The mechanical behavior of collagen is unique compared to classic engineering materials and could serve as inspiration for the design of metamaterials. Considering the wide range of applications for collagen-based biomaterials, a deeper understanding of its structure and mechanics is essential.

The scope of my thesis is exploratory in nature: to investigate the mesoscale structure and bulk shear mechanics of reconstituted collagen I networks. As previous works have highlighted the importance of collagen network connectivity in the bulk shear mechanics [3, 8, 9, 10], here we develop an image-analysis tool for studying the connectivity of collagen networks from microscopy images. Rheological studies have so far focused on the nonlinear elasticity and fracture behavior of collagen networks [3, 8, 9, 10]. Here, we test their time-dependent mechanical response in the nonlinear elastic regime, an aspect of the collagen bulk shear mechanics that is not previously explored.

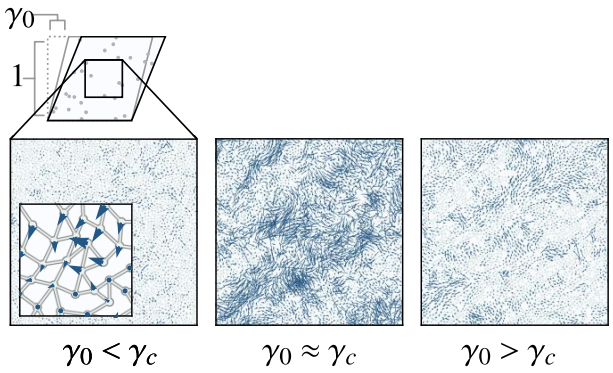

Figure 1: 2D disordered and underconstrained network. The schematic illustrates the local node displacements in a simulated network under the shear strain γ_0. The deviation of local deformations from the macroscale shear deformation reaches a maximum at the critical strain γ_c. Image from Shivers et al.[2]

To summarize, the key research objectives of the thesis are to:

1. Develop an automated image analysis workflow for the accurate 3D reconstruction of the microstructure and connectivity of collagen networks from confocal microscopy images.

2. Investigate the time-dependent mechanics of collagen networks.

The thesis addresses the objectives in two separate chapters. In Chapter 1, we introduce and validate the performance of our image analysis workflow ToFiE (Topologically-aware Fiber Extraction), and use it to quantitatively analyze the 3D architecture of collagen networks from confocal fluorescence microscopy images. This work builds on my previous internship, where I initially developed ToFiE. The chapter is structured in a shorter paper style format.

In Chapter 2, we investigate the time-dependent bulk shear mechanics of the same collagen network microstructures imaged in Chapter 1, using rheology. We find that collagen networks exhibit two transient peaks in dissipation at well-defined stress magnitudes in the high shear strain regime. Our results provide strong evidence that the first dissipative peak corresponds to a second-order mechanical phase transition. We explore potential mechanisms behind the second peak, using insights from our collagen reconstructions in Chapter 1. This chapter is structured in a longer report style format.

1

ToFiE: A Topologically-Aware Fiber Extraction Workflow to Study the Three-dimensional Architecture of Collagen Networks

1.1. Introduction

Biological connective tissues are complex materials with a vast diversity in their mechanical properties. However they share one mutual component, the load-bearing collagen network, that plays a crucial role for their mechanical function. *Ex vivo* studies reveal significant variability in the architecture of these networks across different tissues. In tendons, collagen fibers are organized into aligned, thick bundles whose anisotropic structure gives it high tensile strength along the dominant orientation, while remaining resilient to repetitive, large stresses [11]. In the skin, the network is disordered, providing both elasticity and strength necessary for its function as a protective external barrier [12].

Previous works have highlighted the strong connection between network topology and morphology, and collagen mechanics. Topological parameters, such as connectivity, describe properties of the network that remain unchanged under continuous geometric deformation. In contrast, morphological parameters, such as fiber length and orientation, can change as the network deforms. Lee et al. showed that the circular and spherical variance in fiber orientations from second harmonic generation (SHG) images of the rat cervix correlate with local measurements of the Young's modulus obtained by nanoindentation [13]. Hayn et al. showed that pore size and structural heterogeneity, observed from confocal fluorescence images of collagen matrices, influence local and bulk elasticity measured by atomic force microscopy [14]. It is therefore of great interest to study the collagen network microstructure quantitatively from microscopy images, and eventually correlate it to the mechanical behavior.

Most structural analyses of collagen networks focus on either 2D projections of the imaged microstructure [10, 15, 16, 17], or 3D morphological characteristics [12, 18, 19]. Meanwhile, recent studies combining simulations and rheological measurements of reconstituted collagen I hydrogels show that the average connectivity of collagen networks governs their linear and

nonlinear elastic behavior, as well as their fracture properties [3, 8, 9, 10]. However, determination of the average connectivity is so far model-dependent, and an image-based approach to characterize the topological structure of collagen networks is missing. This can be attributed to the challenge of distinctly resolving collagen fibers in close proximity as they approach the resolution limit of optical microscopes, and to the limitations of current image analysis methods.

Automated methods to study images of fibrous networks can be classified into two main categories; those that use derivative-based filters or transformations (e.g. Fourier transform, wavelet transform) to directly extract structural information such as orientation and anisotropy [20, 21], and those that first trace a skeleton of the filaments before deriving quantities from it [22, 23, 24, 25, 26]. Tracing methods have an advantage over the former, as they can in theory capture the full network description. However, fiber tracing is not a trivial task due to the inherent structural and signal heterogeneity present in experimental images, and few tools such as SOAX, CT-FIRE, Qiber3D, FFA are actually suited to work in three-dimensions [22, 23, 24, 26]. Each of these tools come with their own limitations: SOAX works by stretching open active contours along the fiber signal, but a good reconstruction requires to optimally tune a large number of parameters and good image contrast between the object of interest and the background [22]; CT-FIRE and Qiber3D works by morphological thinning or tracing of the Euclidean distance map after image binarization, making these methods sensitive to the choice of the binary threshold and less suited for dense structures [23, 24]; FFA traces fibers stepwise based on a user-defined intensity threshold and angle, making the method sensitive to noise in the signal and fiber curvature [26]. The main issue with all these approaches is that they identify fragments of fibers, and merge them together based on angle and distance rules, making the individual filaments, and overall network topology ill-defined. In the work of Lindström et al., the authors used the skeletonization function of the Amira software to extract the length, valency, and directional cosine distribution from confocal fluorescence images of collagen networks [27]. However, as the function relies on intensity thresholding, the approach is also unsuitable for denser networks than those investigated (1 mg/mL).

The aim of this chapter is to develop an automated image analysis workflow that can accurately trace and extract individual fibers and the 3D network topology from experimental collagen images. Using the developed workflow, we will investigate how the collagen concentration and the polymerization temperature modulates the collagen network structure. To achieve the aim, ToFiE, a topologically-aware fiber extraction workflow developed during my internship is adapted and optimized here. ToFiE relies on the DisPerSe software to trace a skeleton of the network fibers based on the concepts of Discrete Morse theory (DMT) and persistent homology, overcoming the limitations of previous methods as topology is mathematically defined in DMT [28]. Persistent homology filters out noisy topological features in the skeleton with a measure called persistence, making the approach less sensitive to signal heterogeneity compared to conventional pixel intensity thresholding (e.g Otsu's method). Although DisPerSe was originally developed for extracting the topology of cosmic filaments [28], its translation to biological applications has only been recently demonstrated with DISSECT [29].

In this chapter, we present the ToFiE workflow that integrates image pre-processing, fiber tracing with DisPerSe, skeleton refinement, and graph network construction. We evaluate the

ability of ToFiE to capture network morphology and topology using artificial fluorescence images of synthetic networks. Then, we demonstrate the application of ToFiE to experimental collagen images. Collagen I hydrogels with varied microstructures are prepared *in vitro* by changing the collagen concentration and polymerization temperature, as in prior works [8, 10, 15, 30, 31, 32, 33]. Using confocal fluorescence microscopy, a 3D image library of all the collagen network structures is acquired. Confocal fluorescence microscopy is the most suitable imaging modality for studying the three-dimensional network structure, since label-free techniques are not able to image fibers going out of the imaging plane [34], and scanning electron microscopy images capture only the surface topography of the sample. Lastly, the ToFiE workflow is applied to the images to create 3D collagen network reconstructions, and quantitative measurements of the resulting collagen microstructures for different concentrations and polymerization temperatures are obtained. This chapter complements our exploration of the bulk shear mechanics in Chapter 2, where collagen networks prepared under the same experimental conditions are mechanically tested.

1.2. Methods

1.2.1. NHS-ester labeling of collagen

The methods of Remy et al. [35] and Doyle et al. [36] are adapted and optimized for labeling bovine atelocollagen type I (5133, Biomatrix Fibricol, Advanced BioMatrix) with DyLight™ 550 NHS Ester (ThermoScientific) (see Appendix A.1 for the full protocol). Briefly, bovine atelocollagen type I is neutralized to pH 7.4 in one part 10x phosphate-buffered saline (PBS, pH 7.4, Gibco), 0.1 M NaOH, and MilliQ water, to a final volume of 2 mL and collagen concentration of 5 mg/mL. The solution is polymerized into a gel by incubation in a 37^{o}C water bath for 90 minutes. Following polymerization, the gel is rinsed twice with 1x PBS for ten minutes and then incubated with a buffer consisting of 3 mL of MilliQ and 1 mL of 1 M carbonate buffer (1 M $NaHCO_3$ adjusted to pH 8.3 with 1 M Na_2CO_3) pre-mixed with a two-molar excess of DyLight™ 550 NHS Ester (10 mg/mL in anhydrous DMSO), for one hour at room temperature. The reaction is quenched by replacing the dye buffer solution with 50 mM Tris buffer (pH 7.4) for ten minutes. Unbound dye is removed through six sequential washes with 1x PBS for 30 minutes each. The labeled collagen gel is subsequently dissolved by agitation in 1 mL of 20 mM HCl, and brought down to pH 2 by additional drops of 1 M HCl at 4^{o}C. The obtained solution of DyLight 550-labeled collagen monomers has a final concentration of 3.33 mg/mL.

1.2.2. Collagen hydrogels preparation

Collagen samples are prepared on ice by neutralizing bovine atelocollagen type I solution (5133, Biomatrix Fibricol, Advanced BioMatrix) in one part 10x PBS (pH 7.4, Gibco), 0.1 M NaOH and MilliQ to the target concentration (1.5, 2.5, or 3.5 mg/ml) and to the target pH 7.4. For confocal fluorescence imaging, the samples are prepared with a 1:2 mass fraction of the DyLight 550-labeled collagen monomers (see Appendix A.1 for a representative preparation scheme). The additional salt in the labeled collagen solution is accounted for by reducing the volume of 10x PBS added, as differences in the polymerization times are noticed without salt adjustment. The samples are mixed by pipetting up and down quickly for 30 times, and the pH is double-checked with pH strips at the end of the sample preparation. 80 µL of sample is pipetted into an 18-well glass bottom μ-slide (Ibidi, 81817) for polymerization. The slide is kept in a temperature-controlled environment in a Thermomixer Comfort (Eppendorf) for at least 90 minutes at 37^{o}C, 300 minutes at 30^{o}C or overnight at 26^{o}C to ensure that polymerization is complete. A drop of water is added between the bottom of the slide and the Thermomixer Comfort plate to improve the heat transfer, and surrounding wells are filled with deionized water to ensure humid conditions. The oxygen scavenger mixture consisting of 1 mM Protocatechuic acid and 0.05 µM Protocatechuate-3,4-dioxygenase in 1x PBS is pipetted on top of the polymerized samples before imaging.

1.2.3. Confocal imaging of fluorescent collagen gels

Confocal fluorescence and reflectance images are acquired simultaneously in the Stellaris FALCON 8 confocal microscope (Leica Microsystems), using the 63x glycerol-immersion objective lens (HC PLAN APO CS2, NA: 1.3, Leica Microsystems) and white laser light (80 MHz) controlled by an Acousto-Optical Beam Splitter. For reflectance imaging, the sample is ex-

cited at 488 nm with laser intensity of 3% in reflectance mode and emission light is collected between 478 nm and 498 nm by the HyDS detector at a gain of 10. For fluorescence imaging, the sample is excited at 553 nm with laser intensity of 5% in fluorescence mode and emission light is collected between 561 nm and 740 nm by the HyDX detector at a gain of 20. The top of the coverslip is found by the bright reflection signal, due to the refractive index mismatch between glass and water, and this position was set as 0. Image stacks are acquired starting 20 μm above the coverslip, with an isotropic pixel size of 110 nm, and lateral and axial dimensions of 111.94 μm and 24.64 μm, respectively.

1.2.4. ToFiE workflow

The ToFiE workflow is developed for reconstructing fiber networks from 3D image stacks. Here, we describe the four main steps of the workflow: 1) image pre-processing, 2) skeleton tracing, 3) skeleton refinement, and 4) graph construction.

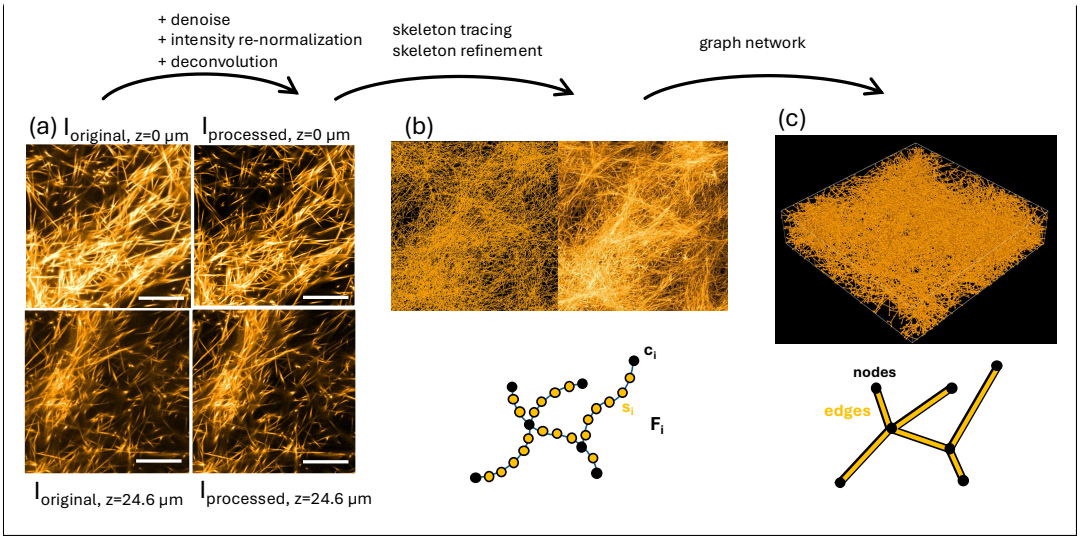

Figure 1.1: An overview of the steps in the network reconstruction workflow. (a) Confocal fluorescence image of a collagen gel. Two XY-slices from the image z-stack are shown. The original image I_{original} is smoothened, re-normalized in intensities, and deconvoluted to obtain the enhanced image $I_{\text{processed}}$. The scale bar represents 15 µm. (b) The 2D projection of the skeleton of the imaged network traced by DisPerSe [28], and further refined through several custom functions is shown (left). The maximum intensity projection of the image is shown for comparison (right).The skeleton consists of filament subunits F_i described by sampling points s_i and endpoints c_i. (c) 3D visualization of the graph network constructed from the skeleton. The dimensions of the sample and reconstruction is 112 x 112 x 24 µm.

1.2.4.1. Image pre-processing

Noise in the raw image is addressed by applying a gaussian filter, followed by a median filter. Both filters are accessible in the scikit-image Python library [37]. The pixel values of the smoothened image, within a specified lower and upper threshold, are re-normalized to the full 8-bit image range (0–255) to ensure uniform contrast and intensity across the z-depth, inspired by the approach of Intensify3D [38]. Pixel values outside the thresholds are clipped to the 8-bit range limits. For the lower limit, a constant threshold value is manually determined for the image stack, or set to zero if the background intensity is minimal. The upper threshold value is determined for each z-slice within the image stack, by taking the nth-percentile pixel intensity

value as a measure of the overall brightness of the slice. The number n is determined manually for the image, such that the nth-percentile intensity value captures the observed intensity attenuation. The nth-percentile intensity value is also smoothened as a function of z-depth by a Gaussian kernel with standard deviation of 8 to ensure continuity between adjacent z-slices. The smoothened and enhanced image stack is deconvoluted with the Gaussian point spread function (PSF) and the Richardson-Lucy deconvolution algorithm with a padding of 10 pixels at the image boundaries using the open source SDeconv python framework [39]. The resolution of the smoothened image, determined with the Fourier Ring Correlation (FRC) function in the open source MIPLIB software [40], is used as the lateral $d_{xy,FRC}$ and axial $d_{z,FRC}$ size of the PSF. Finally, the intensities of the image stack are re-normalized to the full 8-bit image range as previously, to enhance the contrast after deconvolution. An example of an image before and after processing is shown in Figure 1.1a.

1.2.4.2. Skeleton tracing based on discrete Morse theory and persistent homology

Discrete Morse theory (DMT) and persistent homology form the mathematical framework for obtaining a skeleton of the collagen network from the pre-processed image. Briefly, DMT partitions an n-dimensional discrete density field into n-simplices via Delaunay triangulation (Figure 1.2a). Image intensities are assigned to the vertices. Following this, higher order simplices are assigned a value in compliance with discrete Morse conditions. A gradient arrow consists of a simplicial pair of i−simplex and its lower valued cofacet (i+1-simplex), or i−simplex and its higher-valued facet (i−1-simplex) (Figure 1.2b). The sequence of simplicial pairs, where each is a gradient pair, and the simplex in the next pair is a facet of the previous simplex, forms an acyclic gradient path. Simplices that have no gradient pair are considered critical, and can be thought of analogously to the continuous case as points of the density function where the derivative is equal to zero (critical 0-simplex: maximum, critical 1-simplex: saddle-2, critical 2-simplex: saddle-1, critical 3-simplex: minimum) (Figure 1.2c). The gradient vector field linking critical simplices in the density field forms a topological description of the data. By extracting the vector paths between the critical 0- and 1- simplex, 1- and 2- simplex, or 2- and 3- simplex, we can extract the discrete 1-, 2-, or 3- manifold, corresponding to a line, surface, or volume description of the data.

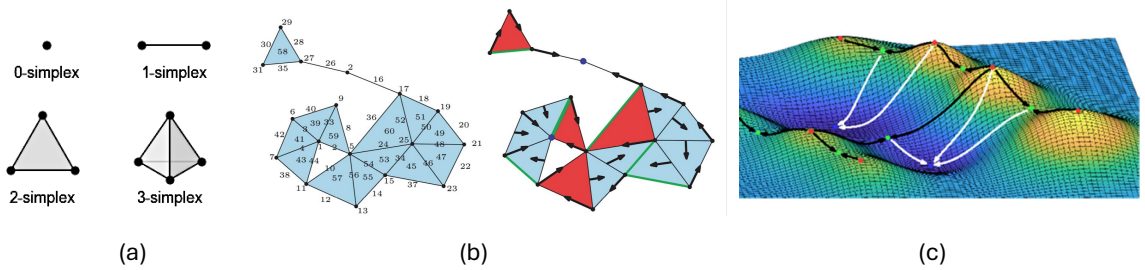

Figure 1.2: Discrete Morse Theory. (a) Simplices of the three-dimensional space. Lower order simplices are faces of the higher order simplex (e.g 3-simplex consist of four 0-faces, six 1-faces, and four 2-faces), or, the higher order simplex is a coface of all lower order simplices. Image from McInnes [41]. (b) A discrete two-dimensional density field. A gradient arrow connects a simplicial pair of simplex i and its only lower valued cofacet (i+1 simplex), or simplex i and its only higher-valued facet (i-1 simplex). Acyclic gradient paths are formed from the sequence of gradient pairs, where the simplex in the next gradient pair is a facet of the previous, and begin and end at a critical simplex (red triangles, green segments and blue points). Image from Sousbie et al. [28]. (c) A continuous two-dimensional density field. Gradient flow lines are curves tangential to the gradient of the density field, which start and end at a critical point (black). Maxima, saddle, and minima points are marked by red, green and blue points. Image from Wang et al. [42].

Persistent homology identifies more robust topological features in the 1-manifold. The persistence of a critical pair is defined as the difference in field intensities of the simplices in the pair, a greater difference indicating greater topological importance. An example is shown in Figure 1.3 to illustrate the concept. A one-dimensional signal and its maximum-minimum critical pairs are portrayed. The noisy pairs that appear as bumps, have a lower persistence and are removed when a certain persistence threshold is set.

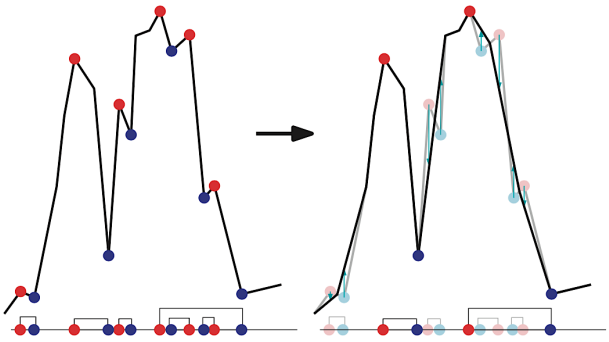

Figure 1.3: Persistent homology. An example of a one-dimensional signal containing noise and its critical pairs of local maxima (red) and minima (blue) (left). Persistence is defined as the difference in field intensities of the simplices in the pair. Low-persistence pairs are removed by setting a persistence threshold, and the remaining pairs are reconnected (right). The resulting signal is smoother and retains its main topological structure. Image from Sousbie et al. [28].

We use the specific implementation of DMT and persistent homology in the DisPerSe software to trace the fiber skeleton through the discrete 1−manifold [28]. DisPerSe is accessed through the Apptainer image glyg/disperse (image ID: f212bff24659) and executed on the DelftBlue supercomputer, supported by the Delft High-Performance Computing Centre [43]. Four parameters (−cut, −smooth, −assemble, −trimBelow) enable processing the 1-manifold

in DisPerSe. The cut parameter sets the persistence threshold and removes less persistent topological features: we determine the optimal threshold with a custom video-tracing visualization (Appendix A.8). Through the video, we qualitatively check whether each fiber in the image is traced out or not. Too high of a cut threshold means dim fibers are not traced, and too low of a threshold results in an overtraced network. The smooth parameter controls the number of sampling points to average over to smoothen a filament. The assemble parameter defines the maximum angle for merging neighboring filaments in the skeleton. The trimBelow parameter removes topological features associated with an intensity lower than a set threshold. Unwanted cross-connections between fibers over dark regions in the image are removed with a high enough threshold. The skeleton S obtained is defined in filament subunits F, where each filament is described by endpoints c and sampling points s (Figure 1.1b).

1.2.4.3. Skeleton refinement

A set of custom functions are developed for further refining the filament subunits within the traced skeleton. Firstly, the original filaments in the skeleton are broken down at the branchpoints or endpoints, such that endpoints cannot be contained within the redefined filament (Figure 1.4a). This establishes a consistent base definition. Filaments shorter than a specific length threshold l_{thr} are merged with their neighboring filament, or removed, depending on the connectivity of the endpoints of the short filament (Figure 1.4b). Neighboring filaments that share a similar orientation within an angle threshold θ_{thr} are merged (Figure 1.4c). To clean up the skeleton further, broken or spurious ends are removed, and to obtain a fully connected network dangling ends can also be removed (Figure 1.4d).

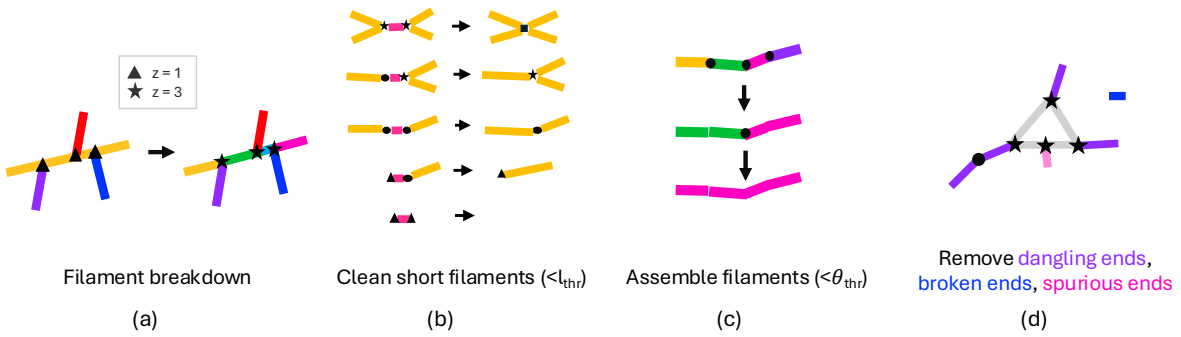

Figure 1.4: Skeleton refinement functions. (a) The original filaments in the skeleton are broken at the junction and new filaments and node valencies are defined. After the redefinition, the filament length represents the fiber inter-crosslink distance. (b) Short filaments smaller than the set length threshold l_{thr} are merged with their neighboring filament, or removed, depending on the connectivity of the endpoints of the short filament, as pictured. (c) Neighboring filaments that share a similar orientation within an angle threshold θ_{thr} are merged. (d) Broken, spurious, or dangling ends can be removed to obtain a cleaner skeleton or a fully-connected skeleton.

1.2.4.4. Constructing the graph network

The processed skeleton is converted into an undirected graph using the NetworkX python library, with nodes and edges representing the endpoints and filaments of the skeleton (Figure 1.1c). Interactive 3D visualizations of the graph networks are made in PyVista.

1.2.5. Simulating confocal fluorescence images of synthetic networks

Synthetic networks consisting of nodes with valencies of 3 or 4, with average connectivity between three and four, are created by Sara Cardona (Appendix A.4). These networks serve as a ground truth for assessing the performance of the reconstruction workflow. First, point cloud descriptions of the simulated networks are made by sampling along their edges at a resolution of 20 points per µm. To replicate the heterogeneity in fiber thickness and signal intensity in biological data, all edges are additionally sampled with a random uniform distribution at a resolution of 10 points per µm, with a 1% uncertainty in its position perpendicular to the edge axis. Using the MicroVIP software [44], 3D image stacks with cubic dimensions of 26 µm and isotropic pixel size of 0.1 µm are simulated from the sampled point clouds. MicroVIP imitates the image acquisition process of a confocal microscope by accounting for various physical factors: we specify the excitation wavelength as 488 nm; the objective magnification as 63x; the numerical aperture as 1.3; the refractive index of the immersion medium as 1.47; and the Gaussian noise standard deviation as 1. For each network, images with varying signal-to-noise ratio are generated by adjusting the photon count parameter across the values of 25, 50, 75, 125, 250, 500, and 10000 (Figure 1.6a). The Gaussian noise standard deviation, the sampling density of the network, and the photon count parameter range together work to visually mimic low to very high noise levels in experimental images.

1.2.6. Sensitivity analysis of the workflow

The performance of the workflow is tested by reconstructing the networks from the simulated images and comparing them with the ground truth (GT) (see Appendix A.2 for the parameter values). For the skeleton refinement step, we determine the parameters l_{thr}= 0.4 µm and $\theta_{\text{thr}} = \frac{\pi}{3}$ to work well for processing the skeleton in the presence of noise and signal heterogeneity (in Appendix A.6 the refinement step with these parameters are shown for an example network). A total of 40 independent networks and 215 reconstructions are explored (Table 1.5). Instead of the photon count parameter, a more tangible measure of the signal-to-noise ratio (SNR) of the images, defined as the average normalized collagen fiber intensity divided by its standard deviation, is calculated with the formula SNR $= \overline{I}_{\text{norm}}/std(I_{\text{norm}})$ based on NoiSee [45]. The normalized fiber intensities I_{norm} are computed as $I_{\text{norm}} = I_{\text{target}} - \overline{I}_{\text{bg}}$. The foreground values I_{target} are obtained by applying a mask, generated from the discretized sampled point cloud, to the simulated image. The background values I_{bg} are obtained by applying the inverse of the dilated mask to the simulated image.

	Samples per photon count parameter						
	25	50	75	125	250	500	10000
<z> = 3.12	10	10	10	10	10	10	10
<z> = 3.20	10	10	10	9	10	10	9
<z> = 3.36	10	10	9	4	2	1	1
<z> = 3.56	10	10	10	3	3	2	2

Table 1.5: Number of samples for each average network connectivity and photon count in the sensitivity analysis.

Two different metrics are leveraged for evaluating the accuracy of the reconstructions as a function of the SNR. The Kullback-Leibler divergence (KLD) quantifies the difference in

information represented by the probability distribution of the reconstruction P_r, and of the GT network P_{GT}. The distributions of two structural parameters are considered: the azimuthal angle θ, defined as the in-plane edge angle measured counter-clockwise from the positive x-axis, and the edge length l. The probability distribution of θ is created as a normalized histogram weighted by the edge length, with eighteen equally spaced bins for $\theta \in [-\frac{\pi}{2}, \frac{\pi}{2}]$. The probability distribution of l is created as a normalized histogram with 40 equally spaced bins for $l \in [0, 20]$. KLD is calculated according to KLD $= \sum_x P_r log\ \frac{P_r}{P_{GT}}$. In the limit of $P_r = P_{GT}$, KLD is equal to 0. Confusion matrix components are computed to locally assess the accuracy of the reconstructed node valencies z. These are defined as follows: true positive (TP) −the reconstruction and GT have overlapping nodes with the same z; false negative (FN) −GT has no overlapping nodes with the reconstruction with the same z; false positive (FP) −reconstruction node has no overlapping nodes with the GT with the same z. Due to the discretization of the networks for confocal image simulation, and propagation of the error, the reconstructed networks are not perfectly aligned with the GT. Therefore, nodes are considered to be overlapping if the distance between their centers $D < 2r$, with $r = 0.3$ µm, and nodes less than 2 µm away from the domain boundaries are excluded due to reconstruction artifacts. The recall score, corresponding to the fraction of correctly reconstructed node valencies, is defined as recall $= \frac{TP}{TP+FN}$.

1.2.7. Analysis of collagen microstructure

3D fluorescence images of the collagen gels are reconstructed using the workflow described in section 1.2.4 (see Appendix A.3 for the parameter values). For the skeleton refinement step, we use the same parameters that are applied for the synthetic networks (Appendix A.6) of l_{thr}= 0.4 µm for dealing with short noisy filaments that are unlikely to be relevant structural features; and $\theta_{\text{thr}} = \frac{\pi}{3}$ to account for slight curvature of the fibers and wobble in the tracing of the fibers. From the reconstruction, various structural parameters are quantified. The histogram of edge lengths with 40 equally spaced bins $\in [0, 20]$ μm is fitted to a log-normal distribution $f_{log-normal}$ with parameters $\bar{l}$ and v as the mean and normalized variance [18].

$$f_{log-normal}(l, \bar{l}, v) = \frac{1}{\bar{l}\sqrt{2\pi\xi^2}} e^{-\frac{(\lambda - \ln l)^2}{2\xi^2}},\ \xi^2 = \ln v + 1,\ \lambda = \ln \bar{l} - \frac{\xi^2}{2} \tag{1.1}$$

Edge density is defined as the sum of edge lengths per unit volume. Local heterogeneity in the microstructure is quantified through subgraphs: the network is divided into $n_{sub}^2 = 1^2, 2^2, 3^2, 4^2, 5^2$ non-overlapping subgraphs to see how the standard deviation in the edge density across subgraphs varies with the subgraph size (Figure 1.11).

1.3. Results

1.3.1. Sensitivity analysis of the ToFiE workflow

We developed the ToFiE workflow for the topological reconstruction of fiber networks from microscopy images (Figure 1.1). Before applying ToFiE to study the microstructure of fluorescent collagen gels, we evaluate its performance using synthetic networks for which the ground truth is known. Artificial confocal fluorescence images of synthetic networks are simulated with different SNR to reflect the range typically observed in experimental images (Figure 1.6a, Methods 1.2.5). In the highest SNR condition, Poisson and Gaussian noise is minimized, but signal heterogeneity across the network is still present. ToFiE is used to reconstruct the networks from these artificial images. In Figure 1.6b a representative reconstruction for the best SNR condition (in magenta) and the corresponding ground-truth GT network (in cyan) is shown. The reconstruction appears to share considerable overlap with the GT network, and captures the junctions. There are some mismatches at the domain boundaries due to boundary artifacts from the simulated image and the reconstruction.

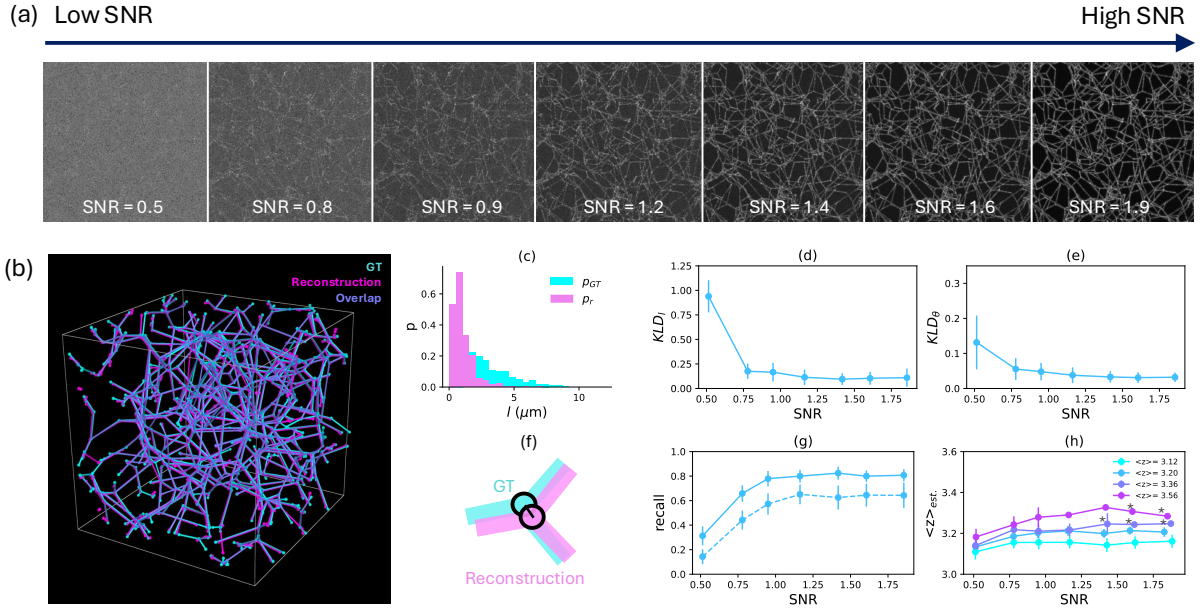

Figure 1.6: Sensitivity analysis of the ToFiE workflow using synthetic networks. (a) Maximum intensity projection of simulated confocal images of a synthetic network with varying signal-to-noise ratios SNR. (b) 3D visualization of the ground truth GT network (cyan) and the reconstruction (magenta) from the confocal image. (c) The probability distributions of the reconstruction p_r (the length distribution here is for SNR = 0.5) and the GT network p_{GT} are compared using the Kullback-Leibler divergence KLD. (d) Average KLD score for edge lengths l and (e) azimuthal angle θ as a function of the SNR. (f) A junction of the groundtruth GT (cyan) and reconstructed network (magenta) are depicted. The recall metric, defined as recall $= \frac{TP}{TP+FN}$, looks at the overlap of nodes with the same valency z between the two networks. A true positive TP instance is defined if there are overlapping nodes with the same valency z between the reconstruction and GT network, within the tolerance, and a false negative FN instance is defined as a GT node having no overlapping node with the same valency. (g) Recall score as a function of the SNR for nodes with valency z=3 (solid line) and z=4 (dashed line). (h) Average connectivity of the reconstructions $\langle z \rangle_{est.}$ as a function of SNR. The star symbol indicates there are less than N=3 samples. Results in (d,e,g,h) are for N=40 independent networks and N=215 reconstructions (Table 1.5). Error bars represent the standard deviation.

For a global comparison of the reconstructions and the GT networks, we quantify the similarity of their edge length and azimuthal angle θ distributions (Figure 1.6c), by computing the Kullback-Leibler divergence KLD score. The KLD score for edge lengths is shown in Figure 1.6d as a function of the signal to noise ratio for N=215 reconstructions. The KLD score remains close to 0.1 for SNR$>$ 0.75, so the edge length is reliably determined for a wide range of image qualities. The reconstruction breaks down at the lowest SNR where mostly fragments are traced out; for SNR$<$0.75 the KLD increases to 0.9. In figure 1.6e the KLD score for the azimuthal angle distributions is plotted as a function of the SNR. Compared to the edge lengths, θ distributions are less sensitive to the SNR, with a small increase in KLD to 0.13 at the lowest SNR. This can be explained by the fact that even if fragments are traced out, the identified orientations of the fragments remain robust.

Importantly, we are interested to see whether the reconstructions are able to reproduce the topology of the networks. To test this, the one-to-one correspondence of the node valencies in the GT network and reconstruction are computed (Figure 1.6f). Since the GT network and reconstruction do not fully align in space, we allow for a small margin of tolerance (nodes are considered overlapping if the distance between their centers $D < 2r$, with $r = 0.3$ µm). We define a true positive TP instance if there are overlapping nodes with the same valency z between the reconstruction and GT network, within the tolerance. A false negative FN instance is defined as a GT node having no overlapping node with the same valency. In Figure 1.6g, the recall score is plotted as a function of the SNR for z=3 nodes (solid line) and z=4 nodes (dashed line). The non-zero recall score confirms that the reconstructions are able to capture the junctions in most cases. The recall score for nodes with valency 3 or 4 is maximized at 0.8 and 0.6, respectively, and starts to decrease from SNR $<$1. These results suggest that the reconstructions are able to capture 3-junctions more frequently compared to 4-junctions. The difference in recall might be explained by the coarse discretization of the network in the simulated images, and abrupt intensity transitions due to uncertainty introduced with the sampling strategy. We therefore sometimes notice 4-junctions being identified as two closely positioned 3-junctions. In Figure 1.6h, we show the average estimated connectivity of the reconstructions $\langle z \rangle_{est.}$ as a function of the SNR, for simulated networks with a true connectivity of $\langle z \rangle$ = 3.12, 3.20, 3.36, 3.56. The lower recall for z=4 nodes means that as the true $\langle z \rangle$ increases (i.e. the network contains more 4-junctions), the systematic underestimation of $\langle z \rangle$ also increases. Nevertheless, within the range of $\langle z \rangle \in [3.12, 3.56]$, a relative difference in $\langle z \rangle$ is still distinguishable. For networks with $\langle z \rangle$ = 3.12, the reconstructions show the lowest $\langle z \rangle_{est}$ across all SNR, and similarly, the reconstructions for the networks with $\langle z \rangle$ = 3.56 show the highest $\langle z \rangle_{est}$ across all SNR.

1.3.2. Confocal fluorescence images of collagen networks

Next, to study the structure of real collagen networks, we prepare collagen gels with varying microstructures by adjusting their concentration (1.5, 2.5, or 3.5 mg/mL) and polymerization temperature (26^{o}C, 30^{o}C, or 37^{o}C). For confocal fluorescence imaging, the gels are polymerized with a mixture of fluorescently labeled- and unlabeled- collagen monomers. We first check that the network structure is not influenced by the labeling, by comparing the confocal reflectance images of unlabeled and labeled gels (Appendix A.1). Qualitatively little difference between the unlabeled and labeled gels is observed, so it is assumed that they resemble each other in terms of structure. The fluorescence signal of the labeled network also colocalizes

with its reflectance signal, confirming that a single network rather than two interpenetrating networks is formed. A library of confocal fluorescence images for all the collagen microstructures is developed and shown in Figure 1.7 (see Appendix A.7 for a second sample for each of the conditions). At 37^{o}C, collagen forms a homogeneous mesh network that becomes denser with increasing concentration. At 30^{o}C, the networks are less homogeneous and the fibers appear slightly longer. Some bundling between fibers is visible in the 1.5 mg/mL network polymerized at 30^{o}C, but bundling becomes more prominent in the 3.5 mg/mL network polymerized at 30^{o}C. The networks polymerized at 26^{o}C are the most heterogeneous, and show significant concentration-dependent bundling behavior: at the concentration of 1.5 mg/mL, the network shows a little bundling but is mostly homogeneous across the field of view; at the concentration of 3.5 mg/mL, the network consists of dense regions of large fiber bundles and sparse regions with few fibers. The bundles are formed from the aggregation of many short fibers. The fibers also appear to be thicker at lower temperatures, translating to a higher fluorescence signal.

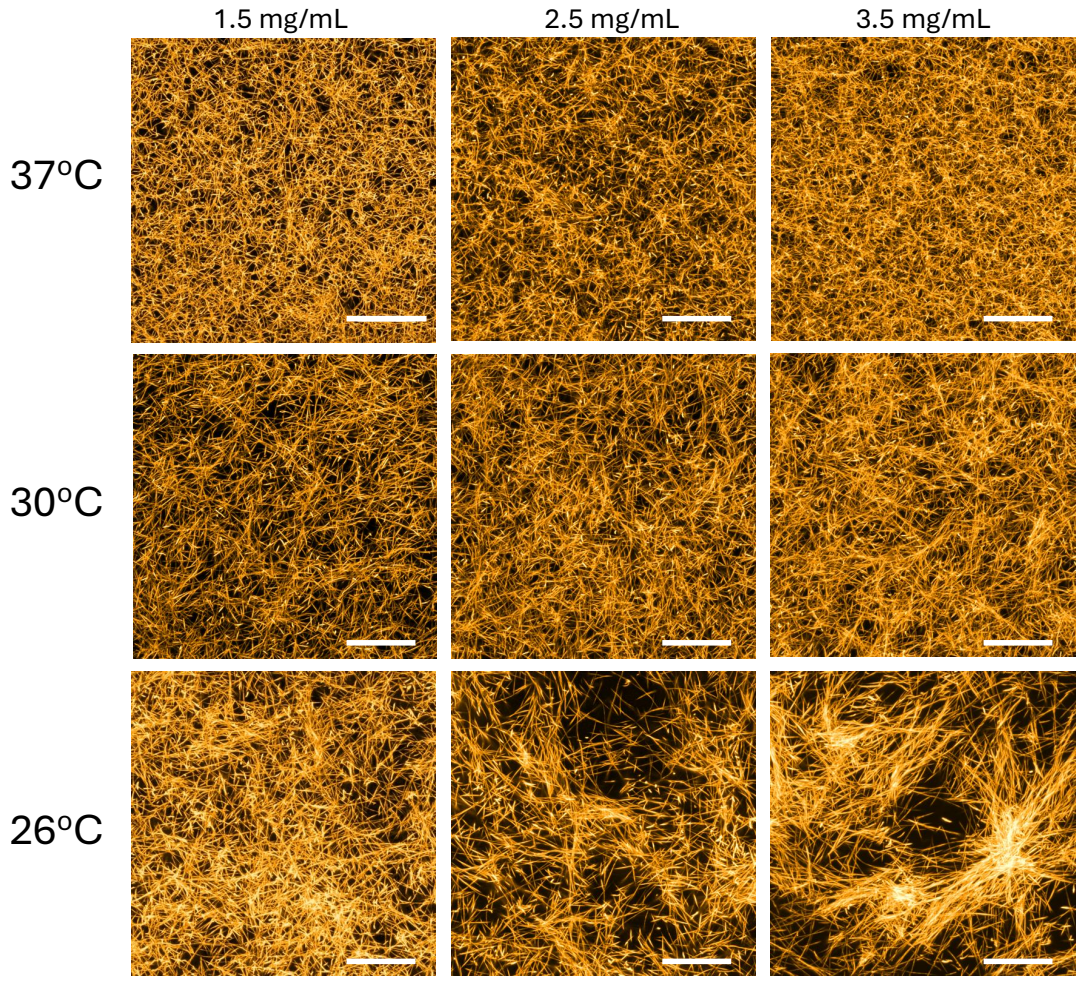

Figure 1.7: 3D image library of collagen microstructures. The maximum intensity projection of processed confocal fluorescence images of the collagen gels (concentration: 1.5, 2.5, 3.5 mg/mL, polymerization temperature: 26^{o}C, 30^{o}C, 37^{o}C) prepared with 1:2 mass fraction of Dylight 550 labeled collagen monomers are shown over a depth of 4.95 µm. Scale bar represents 25 µm, and the image size is 112 µm with an isotropic pixel size of 0.1 µm.

1.3.3. Structural analysis of collagen network reconstructions

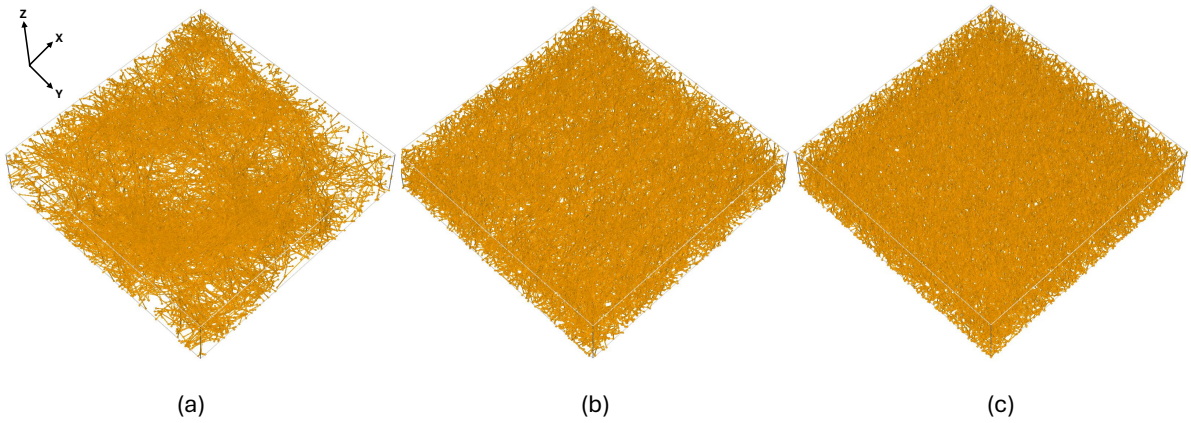

Figure 1.8: 3D visualization of the collagen network reconstructions. A representative sample is shown for the 3.5 mg/mL network at the polymerization temperature of (a) 26^{o}C, (b) 30^{o}C, and (c) 37^{o}C. The sample dimensions are 112 x 112 x 24 µm.

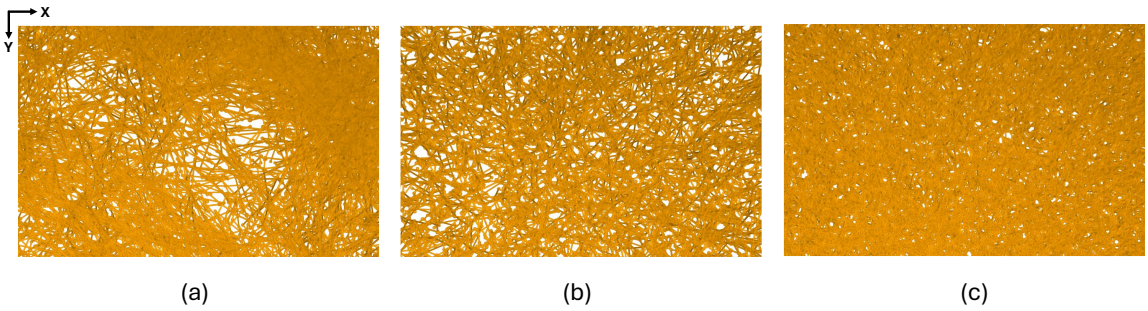

Figure 1.9: Zoomed-in 3D visualization of the collagen network reconstructions. A representative sample is shown for the 3.5 mg/mL network at the polymerization temperature of (a) 26^{o}C, (b) 30^{o}C, and (c) 37^{o}C.

To quantify the collagen network structure and topology in the various polymerization temperatures and concentration conditions, ToFiE is applied to the images to create 3D reconstructions. In Figure 1.8, and Figure 1.9, the reconstructions of the 3.5 mg/mL collagen networks polymerized at 26^{o}C, 30^{o}C and 37^{o}C are shown. In Figure 1.10a, we show the violin plots of the edge lengths of the reconstructions, for N= 1 sample (1.5 mg/mL network polymerized at 30^{o}C and 37^{o}C) or N=2 independent samples (all the other conditions). Additionally, the log-normal distribution (Equation 1.1), parametrized by the mean $\bar{l}$ and normalized variance v of edge lengths, is fitted to the data and shown in Figure 1.10b. Edge length is defined as the inter-crosslink distance of fibers. At 37^{o}C, the mean edge length consistently decreases with increasing concentration, whereas at 30^{o}C and 26^{o}C the trend is nonmonotonic, with a slight increase in the mean edge length for the concentration of 2.5 mg/mL and a decrease for the concentration of 3.5 mg/mL. Surprisingly, the edge length distribution of the 1.5 mg/mL and 3.5 mg/mL network polymerized at 26^{o}C are not significantly different ($p>0.05$), despite the structural differences we observe in the images. However, the edge length distribution for different

polymerization temperatures within the same concentration are significantly different. For the concentration of 1.5 mg/mL, the mean edge length is smallest at the temperature of 26^{o}C ($\bar{l}$ = 1.96 µm) and largest at 30^{o}C ($\bar{l}$ = 2.26 µm). For the concentration of 3.5 mg/mL, the mean edge length is smallest at the temperature of 37^{o}C ($\bar{l}$ = 1.8 µm) and largest at 30^{o}C ($\bar{l}$ = 2.21 µm). The networks polymerized at 30^{o}C have the largest mean edge length across all concentrations.

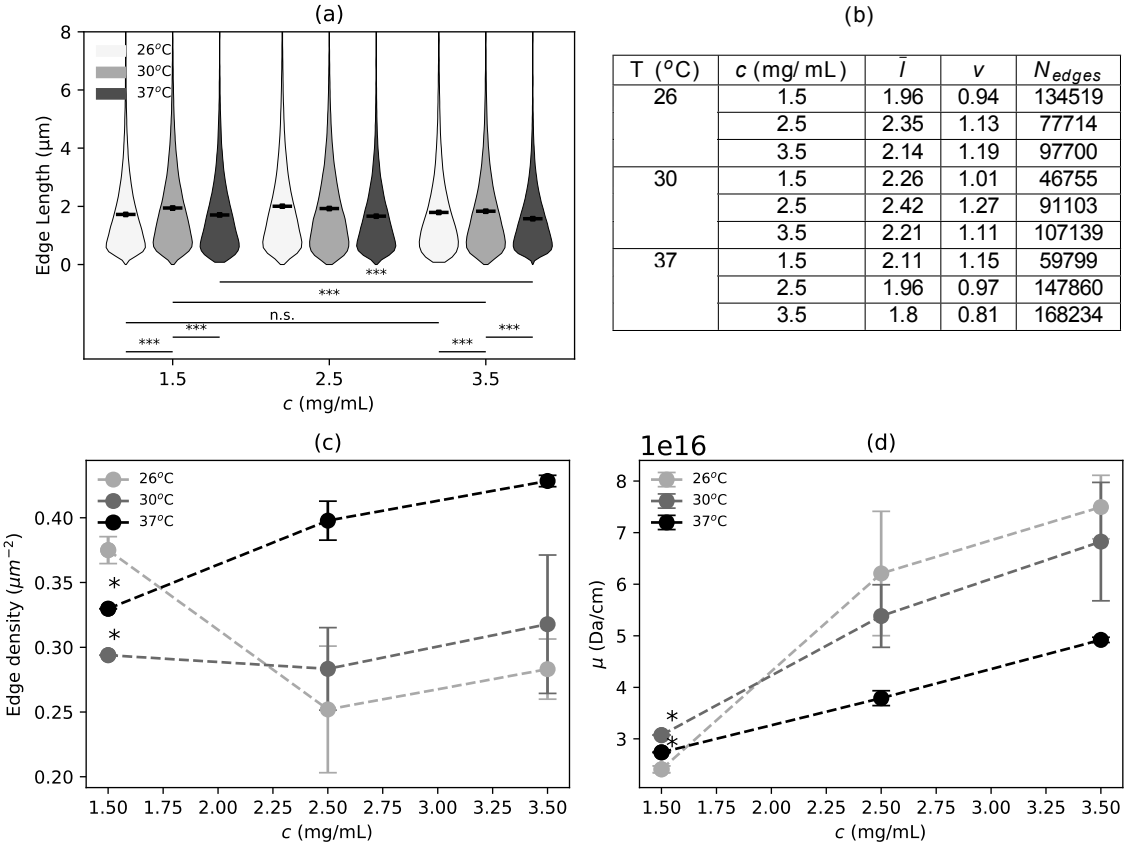

T (°C)	c (mg/ mL)	$\bar{l}$	v	N_{edges}
26	1.5	1.96	0.94	134519
	2.5	2.35	1.13	77714
	3.5	2.14	1.19	97700
30	1.5	2.26	1.01	46755
	2.5	2.42	1.27	91103
	3.5	2.21	1.11	107139
37	1.5	2.11	1.15	59799
	2.5	1.96	0.97	147860
	3.5	1.8	0.81	168234

Figure 1.10: Edge lengths and densities as a function of the polymerization temperature and collagen concentration. (a) Violin plots of the edge lengths pooled from N=2 samples, except for the 1.5 mg/mL network polymerized at 30^{o}C and 37^{o}C, which has N=1 sample. The mean is marked by the black square. Significant differences in the distributions are tested with the Mann-Whitney U-test. *** indicates a p-value $\leq$0.0005 and n.s stands for not significant. (b) Table of values of the edge lengths fitted with a log-normal distribution, where the fit parameters $\bar{l}$ and v represent the mean and normalized variance at different temperatures and concentrations. N_{edges} shows the total number of edges considered. (c) The average edge density, defined as the total length of edges per unit volume, shown for the different conditions. The points marked with * show the results of N=1 sample, otherwise N=2 samples. Error bars represent the standard deviation between samples. (d) The average mass to length ratio μ shown for the different conditions. The points marked with * show the results of N=1 sample, otherwise N=2 samples. Error bars represent the standard deviation between samples.

In Figure 1.10c the edge density, defined as the sum of edge lengths per unit volume, is plotted as a function of the concentration. The edge density measurements support our earlier observations of bundling: at 37^{o}C the density increases with concentration (0.33 µm^{-2} and 0.43 µm^{-2} at 1.5 and 3.5 mg/mL respectively); at 30^{o}C the density stays relatively constant across concentrations (0.29 µm^{-2} and 0.33 µm^{-2} at 1.5 and 3.5 mg/mL respectively); and at 26^{o}C the average edge density appears to slightly decrease (0.38 µm^{-2} and 0.28 µm^{-2} at 1.5 and 3.5 mg/mL respectively). Surprisingly, the edge density of the 1.5 mg/mL network poly-

merized at 37^{o}C is slightly lower than that of the 1.5 mg/mL network polymerized at 26^{o}C, which may be due to having only one sample for the former. In the work of Jansen et. al. the edge density is derived using the relation $\rho_l = \frac{c}{\mu}$, where c is the collagen concentration, ρ_l is the edge density, and the mass-length ratio μ is obtained from turbidimetry experiments [10]. Here, μ is inversely determined as an estimate of the average fiber diameter using the edge density and concentration, and is shown in Figure 1.10d. For all temperatures, μ increases with the concentration. The increase in μ is smallest at 37^{o}C ($\Delta\mu = 2 \cdot 10^{16}$ Da/cm) and largest at 26^{o}C ($\Delta\mu = 5 \cdot 10^{16}$ Da/cm).

From the images, we observe that the network becomes more heterogeneous at lower temperatures and higher concentrations (Figure 1.7). We quantify the heterogeneity in the edge density within a sample by subdividing our collagen network reconstructions in the xy plane into non-overlapping subgraphs (Figure 1.11a). In Figure 1.11b, the average and standard deviation in the edge density across subgraphs is shown as a function of the subgraph size. The focus here is on the magnitude of the standard deviation between subgraphs, which can be used as a measure of the heterogeneity. The networks polymerized at 37^{o}C are considerably homogeneous for the length scales considered here, with a small standard deviation for all subgraph sizes, the smallest subgraph being one fifth of the original network size ($\frac{1}{5}\times$ 112.64 µm = 22.53 µm). The networks polymerized at 30^{o}C and 26^{o}C show an increasing standard deviation from a subgraph size of 0.5 (or $\frac{1}{2}\times$ 112.64 µm = 56.32 µm). Notably, the standard deviation is much larger for the 3.5 mg/mL network polymerized at 26^{o}C compared to the other networks, nearly reaching 0.2 µm^{-2}.

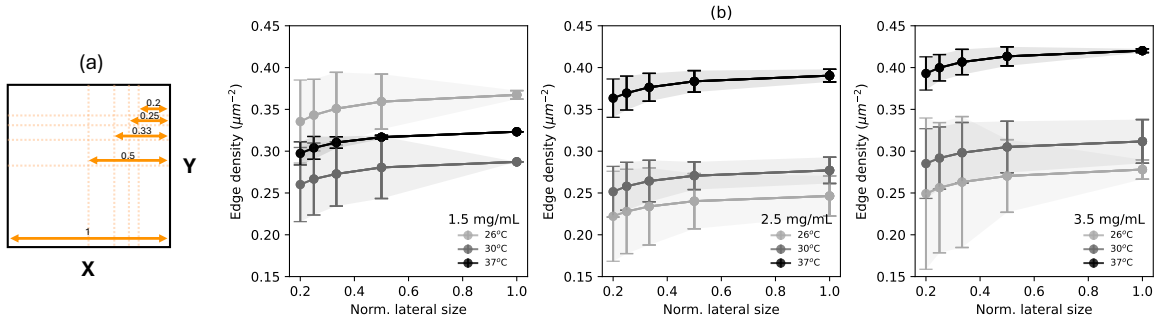

Figure 1.11: Subgraphs reveal the heterogeneity length scale of the networks. (a) The network is subdivided across x- and y- into 1^2, 2^2, 3^2, 4^2, or 5^2 non-overlapping subgraphs. The numbers on the orange arrows indicate the different normalized lateral dimensions of the subgraphs. (b) The average edge density across subgraphs, averaged over N=2 samples, except for the 1.5 mg/mL network polymerized at 30^{o}C and 37^{o}C, which has N=1 sample. The error bar represents the standard deviation between subgraphs, averaged over the samples.

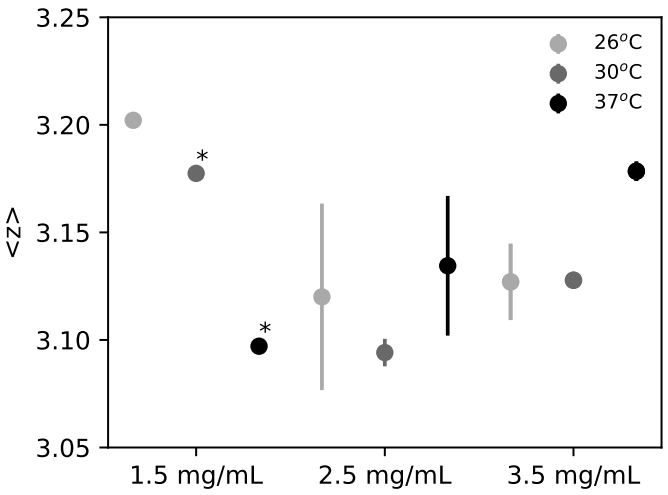

Figure 1.12: Average connectivity <z> of collagen networks. The error bar represents the standard deviation between N=2 samples. Points marked with * show the results of N=1 sample.

Lastly, we look at the average connectivity of the networks, and plot this in Figure 1.12 for N=2 samples (or N=1 sample if marked by a star). At the lowest concentration of 1.5 mg/mL, <z> increases with decreasing polymerization temperature (26 ^{o}C: <z> = 3.20, 30^{o}C: <z> = 3.17, 37^{o}C: <z> = 3.09). However, for the collagen concentrations of 2.5 mg/mL and 3.5 mg/mL, a temperature dependence of <z> cannot be concluded considering the small sample size and the large standard deviations. At these concentrations, the networks are also interspersed with bundles which may complicate the <z> estimation.

1.4. Discussion

The four-step ToFiE workflow enables the three-dimensional reconstruction of fiber networks from high resolution microscopy images. Compared to existing tools for fiber tracing, ToFiE demonstrates the ability to preserve both the morphology and topology of the original network. The first step of the workflow addresses noise, intensity attenuation with depth, and optical distortions in the raw confocal fluorescence images. By enhancing the image signal in this step, we improve the performance of DisPerSe, used in the next step for tracing the fiber skeleton. DisPerSe utilizes discrete Morse theory and persistent homology to compute the 1-manifold skeleton of the image data. The topology of the 1-manifold is defined mathematically, and is accurate to the underlying structure given an optimal image. A similar topological-awareness in tracing is missing in conventional approaches which rely on image binarization and thinning, or pixel-by-pixel tracing. DisPerSe has been used by Merle et al. for segmenting apical cell surfaces and their cytoskeleton [29]. In this study, we identify image processing (Figure 1.1a), the breakdown of filaments at junctions, and the redefinition of individual filaments (Figure 1.4) as crucial steps for accurately retrieving the topology of biological networks, and integrate it into the ToFiE workflow.

In this chapter, we evaluate the performance of ToFiE by applying it to reconstruct artificial confocal images of synthetic networks. To assess the sensitivity of the workflow, we simulate images with varying signal-to-noise ratios (SNR) and signal heterogeneity across the network (sampling using a uniform distribution with positional uncertainty), mimicking complex experimental data. The results demonstrate that the network morphology, including edge lengths and azimuthal angles, is accurately captured over a wide range of SNR (Figure 1.6). Topology is also preserved in the reconstructions, as demonstrated with the non-zero recall score. The recall scores of 0.8 for degree 3 nodes, and 0.6 for degree 4 nodes is reasonably high, but it may be insufficient to distinguish networks with similar <z>, particularly as <z> approaches 4. In these cases, the systematic underestimation of <z> may be greater than the standard deviation between samples. The recall score can be improved with further calibration of the workflow: by optimizing the image pre-processing step; by adjusting the skeleton refinement parameters, in particular increasing l_{thr} can improve the recall of degree 4 nodes, through merging of degree 3 nodes close to each other over a slightly larger distance. Several limitations of the test are noted: the small dimensions of each simulated network amplifies the influence of boundary artifacts. Furthermore, the simulated confocal images show more abrupt intensity changes from pixel to pixel compared to experimental images. This can contribute to a lower recall score than expected if the ToFiE workflow is applied to real images.

ToFiE is successfully applied to confocal fluorescence images of collagen networks (Figure 1.8). To obtain the most accurate three-dimensional reconstruction, the collagen gels are imaged with an isotropic pixel size of 0.11 μm. The computationally intensive step of the workflow is the tracing step carried out by DisPerSe. The computation time depends on how dense the network is, but takes approximately 1-3 hours for the image size of 1024 x 1024 x 224 pixels (112 x 112 x 24.64 μm), using six 2.1 GHz CPUs (16 GB memory per CPU) on the compute node of DelftBlue. With the reconstructions, we find the microstructural parameters to show a non-monotonic relation with the collagen concentration and polymerization temperature. At the highest temperature of 37^{o}C, there is a consistent decrease in the edge length, and

increase in the edge density with increasing concentration (Figure 1.10a,c). At 30^{o}C and 26^{o}C, the edge length shows no clear trend with concentration, and the edge density remains constant or decreases with concentration, respectively, which may be attributed to the increased fiber bundling. In support of this, we provide evidence that fibers grow thicker at lower temperatures and higher collagen concentrations: the average mass-to-length ratio of fibers is larger, and also increases the most with concentration at the temperature of 26^{o}C (Figure 1.10d).

These findings align with the work of Jansen et. al., where an increase in fiber diameter with lower polymerization temperatures was also found through SEM images of the collagen networks, and with turbidimetry measurements [10]. However, the mass-length ratio determined with turbidimetry by Jansen et al. decreases slightly with increasing concentration and is approximately two orders of magnitude smaller, contrasting our findings [10]. The difference in the magnitudes may be due to the difference in collagen type (bovine vs. rat tail), and the measurement method. On the one hand, with the reconstruction some fibers can be left untraced. On the other hand, turbidimetry assumes monodisperse fibers, and its sensitivity can be affected by dense and heterogeneous network structures. The trend in the mass-length ratio with concentration may be more accurately determined with the reconstructions since ToFiE is expected to not be influenced by the heterogeneity of the microstructure. From previous literature, concentration and temperature are both expected to increase the nucleation rate and growth rate of fibers [46, 47, 48]. At higher concentrations, the collagen monomers are in closer vicinity to another, and with higher polymerization temperatures, the molecules have increased diffusive motion and stronger hydrophobic interactions. Both aspects likely contribute to the homogeneous and branched network structure observed at 37^{o}C (Figure 1.7). At lower temperatures, limited diffusion combined with a lower frequency of nucleation events promotes larger bundle growth over branching, resulting in the heterogeneous network structure observed at 26^{o}C.

Lastly, we find that the collagen networks have an average connectivity in the range of <z> = 3.05 - 3.20 (Figure 1.12). These numbers should not be taken as absolute values, given the tendency of the ToFiE workflow to underestimate <z>. At 1.5 mg/mL, the <z> decreases with increasing temperature. But at 2.5 mg/mL and 3.5 mg/mL, no clear relation between <z> and temperature can be observed. The average connectivity of collagen networks has not been determined before using an automated image analysis approach. However, Jansen et al. have tried to determine the average connectivity of their networks by fitting the experimentally measured stiffening strain to the mechanics of simulated 2D disordered networks [10]. With this approach, they found that <z> increases with decreasing temperatures for rat-tail collagen (26^{o}C 4 mg/mL: <z> = 3.55, 37^{o}C 4 mg/mL: <z> = 3.1), with a weak concentration-dependence. However, they also tried to quantify <z> manually by checking the valency of 100 random junctions in SEM images, and could not find a dependence of <z> on the polymerization temperature. ToFiE shows the potential to determine <z> from confocal fluorescence images, but the sample size should be extended to draw conclusions on the temperature or concentration dependence.

For future work, it would be interesting to explore network heterogeneity in more details. Simulations frequently study the behavior of 2D or 3D lattice-based networks with varying <z> that are entirely homogeneous. Little is known about how heterogeneity in disordered networks in-

fluence their mechanical behavior. The experimentally-derived reconstructions can serve as a basis for simulations to more closely recapitulate the topology of real collagen networks. From visual inspection, heterogeneity introduces additional length scales to the network, within the bundles and between bundles (Figure 1.7), which are not captured by the edge length measurements (Figure 1.10a). Local differences in the connectivity, and length scales associated with bundling can be further studied with our reconstructions using concepts from graph theory (centrality measures, shortest paths), and may provide insights in how networks differentially respond to micro- and macro- loads.

To conclude, ToFiE is not limited to tracing collagen networks, nor is it limited to working with confocal fluorescence images. Many other biopolymers in nature form similar disordered fiber network structures with mechanically important roles: fibrin networks are the load-bearing and stabilizing components of blood clots; actin, intermediate filaments and microtubules form a composite cytoskeletal network and jointly regulate cellular shape and mechanics. This workflow can be used to reconstruct any biological structure given a high-resolution 2D or 3D image. If topology (i.e. connectivity) is not essential to quantify, the ToFiE workflow can also be applied to label-free imaging modalities such as confocal reflectance and second harmonic generation images, to extract morphological parameters (in-plane angles, edge lengths and density) with high accuracy.

1.5. Conclusion

We present ToFiE, a topologically-aware fiber extraction workflow for studying the microstructure of biopolymer networks in microscopy images. We demonstrate the ability of the ToFiE reconstructions to capture both the morphology (in-plane angles, edge length and edge density) and topology (connectivity) of synthetic networks. The workflow is successfully applied to confocal fluorescence microscopy images of bovine atelocollagen I hydrogels, to investigate the influence of concentration and temperature on their microstructure. Our 3D collagen network reconstructions show that fiber bundling, structural heterogeneity and fiber thickness exhibit a nonlinear increase with higher collagen concentration and lower polymerization temperatures. Furthermore, we find that the edge length and network connectivity shows a non-monotonic relationship with concentration and temperature. Altogether, our findings indicate that multiple microstructural features besides network connectivity are significantly changing in the collagen networks, which may be crucial to consider for their mechanics.

2

Strain- and Time- dependent Bulk Shear Mechanics of Collagen Networks: Elasticity, Viscoelasticity and Critical Phase Transition

2.1. Introduction

2.1.1. The complex mechanics of collagen networks supports a wide variety of biological processes

Collagen type I is the most abundant protein found in biological tissues, and is a key component of the extracellular matrix as a biophysical scaffold for cells. The basic building block of collagen is a triple helix consisting of three peptide chains bound together by hydrogen bonds (Figure 2.1) [46]. Lateral and axial polymerization of the monomers into fibrils is self-driven by hydrophobic and electrostatic interactions in physiological conditions [48]. Fibrils further assemble into fibers, which branch out and crosslink to form a percolating network structure. As the networks are formed from branches and junctions, they have an average connectivity between three and four [3, 10]. Based on Maxwell's definition of isostaticity stating that the number of constraints for a node is equal to the degrees of freedom it has, collagen networks are sub-isostatic.

Sub-isostatic networks exhibit complex material behavior. Collagenous tissues are soft for small deformations and stiff for large deformations. They behave both viscoelastically and plastically allowing for time-dependent responses and structural remodeling. These special properties enable collagen networks to support the wide range of tissue requirements: to function as the main load bearing component, to provide mechanical and physical cues to embedded cells, regulating biological processes such as differentiation and migration, and to maintain tissue integrity under large or sudden deformations. The origins of the complex mechanics of collagen likely stem from its hierarchical structure spanning multiple length scales [9, 49, 50]. The combined findings from experimental investigations on reconstituted collagen I gels and numerical simulations of disordered networks paint an extensive but incomplete picture [2, 3, 10, 30, 32, 51, 52, 53].

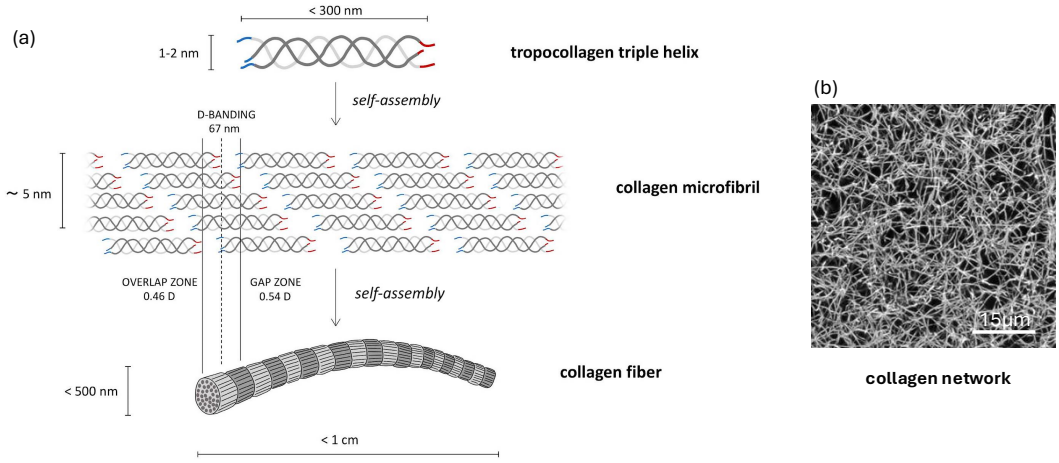

Figure 2.1: The hierarchical structure of collagen fibers. (a) Three peptide chains form a triple helix, which aggregate laterally and axially in a staggered fashion to form microfibrils. Microfibrils bundle together to form fibers that branch out and crosslink to make a network. Adapted from Salvatore et. al. [54]. (b) Confocal fluorescence image of a 1.5 mg/mL bovine atelocollagen type I network formed at 37^{o}C maximum intensity projected over a depth of 4.95 µm.

2.1.2. Linear elasticity is controlled by bending rigidity

Collagen filaments can be considered as stiff athermal filaments in comparison to more flexible biopolymers such as intermediate filaments and elastin. The stiff filaments contribute to the mechanical stability of the network with their finite bending, compressive and stretching stiffness. For small strains, the networks behave linearly elastically (Figure 2.2a). The linear shear modulus $G_0 \propto \tilde{\kappa}$ is proportional to the dimensionless bending rigidity $\tilde{\kappa} = \frac{\kappa}{\mu_s l_c^2}$, where κ is the bending rigidity, μ_s is the stretching modulus and l_c is the lattice spacing in disordered lattice network simulations [8, 10]. κ is controlled by the mass-length ratio, the degree of fibril bundling, and intra-fibrillar crosslinking, which are dependent on the polymerization conditions of collagen, the addition of crosslinking agents, and the source of the collagen [10, 31, 32].

2.1.3. Nonlinear elasticity involves a transition from bending- to stretching-dominated rigidity

Beyond a certain strain, collagen networks stiffen dramatically (Figure 2.2a). The stiffening was thought to arise from the bending-to-stretching transition of network fibers [55]. However, findings demonstrate that onset of stiffening precedes the transition [8, 10]. Initial stiffening corresponds with the build up of negative normal stress in the network under shear, which arises due to the asymmetry of forces exerted by the fibers: stretched fibers exert greater forces than the fibers that are compressed, generating net negative tension perpendicular to the shear plane [10, 56, 57, 58]. Therefore, the nonlinear regime may be distinguished into two parts, where the first part is bending-dominated, and the second part is stretching-dominated (Figure 2.2a) [8, 10, 15]. Loading beyond the linear regime is also accompanied by geometric rearrangements of the network, with a subset of load-bearing fibrils aligning in the principal direction of the load forming so called force chains through which stress is transmitted [59] (Figure 2.2b), and a subset buckling or bending [15, 30, 32, 58, 60]. The change from bending to stretching

dominated rigidity has been described by simulations to be a second-order phase transition, with strain as the control parameter and the differential modulus as the order parameter [9] (Figure 2.2c). Approaching the critical strain, simulated networks show a divergence in non-affine strain fluctuations, in the zero-shear viscosity and in the slowest relaxation time that can be described by critical exponents [2, 9, 53, 61]. So far no experimental evidence exists to support these findings.

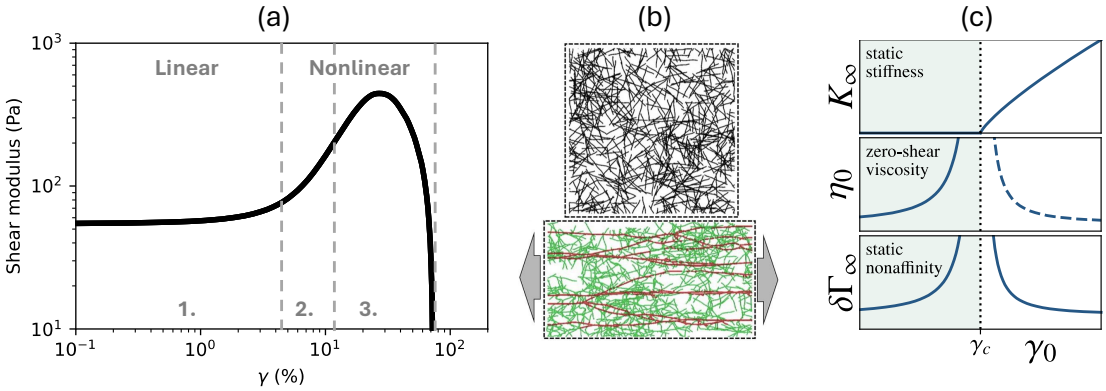

Figure 2.2: Nonlinear elasticity of collagen networks. (a) The differential shear modulus $d\sigma/d\gamma$ shows the strain-stiffening behavior of a 3.5 mg/mL bovine atelocollagen type 1 network polymerized at 37^{o}C as a function of shear strain γ. Three different regimes can be identified: 1. linear elastic regime, 2. nonlinear elastic bending-dominated regime, 3. nonlinear elastic stretching-dominated regime. (b) Example of a simulated network at rest (top) and under tension (bottom). When strained above the critical strain, a load-bearing subnetwork develops, forming highly aligned tracts called force chains (shown in red). Figure from Ban et. al. [59]. (c) The second order mechanical phase transition at the onset of rigidity predicted by simulations, is accompanied by a divergence in various quantities like the zero-shear viscosity and nonaffine fluctuations. Figure from Shivers et. al. [2].

2.1.4. Network microstructure determines the emergent bulk shear mechanics

Previous studies have highlighted the importance of network structure in their mechanics. The efficiency of stress transmission is linked to the microstructure: when a local deformation is applied, the morphology of the force chains that develop depends on the mechanical properties of individual fibers and the local connectivity within the network [51]. The average network connectivity, <z>, was found to control both the linear and nonlinear elasticity [10, 18]. The connectivity is either determined from manual inspection of microscope images (Figure 2.3a), or indirectly derived by fitting rheological data to a model [3, 10]. The average connectivity is proportional to the linear shear modulus [18]. Experiments and simulations show the threshold strain for nonlinearity and critical strain monotonically decreases with increasing <z> (Figure 2.3b,c) [3, 8, 10, 61]. The degree of network stiffening in the first non-linear part is related to <z>; a more connected network stiffens less, while in the stretching-dominated nonlinear regime, the stiffening becomes independent of <z> or fibril density [8]. Fracture behavior is also influenced by <z>, where a less connected network fractures at higher strains in a more ductile manner (Figure 2.3d) [3]. Surprisingly, elasticity was found to be largely insensitive to other features besides connectivity. However, simulations of Mikado, Voronoi, and packing-derived networks with the same <z> showed quantitative differences in their mechan-

ical behavior [61], which suggests that additional structural parameters must be influencing the mechanics of these networks.

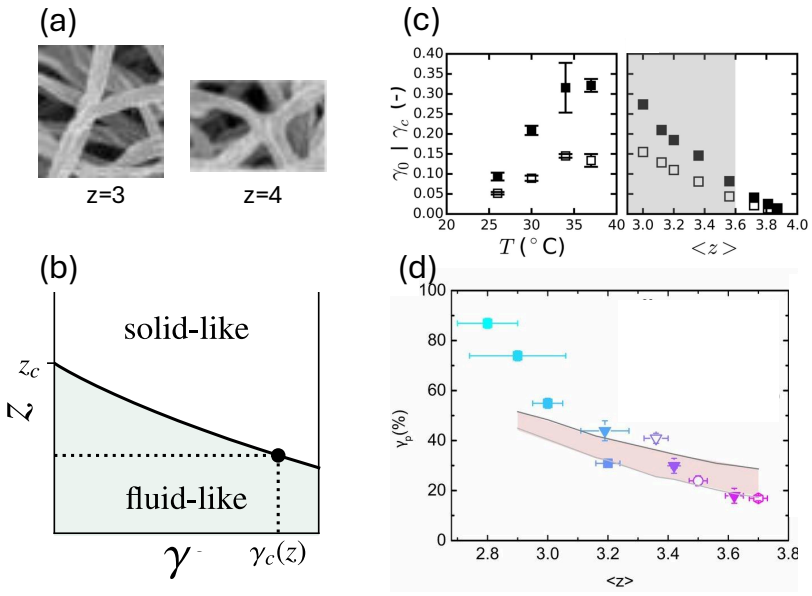

Figure 2.3: The average network connectivity <z> plays an important role in the elasticity and fracture of collagen. (a) Scanning electron microscope images of fiber junctions in collagen. Figure from Jansen et. al. [10]. Networks consist of a mixture of branches with a valency z=3, and junctions with z=4. (b) Sub-isostatic networks with connectivity $z < z_c$, the critical isostatic connectivity, develop rigidity once strained past a z-dependent critical strain value $\gamma_c(z)$. Adapted from Shivers et. al. [2]. (c) Experimental findings (left) show the onset strain γ_o and critical strain γ_c increases with polymerization temperature, and simulations (right) show the onset and critical strain monotonically decreases with increasing <z>. Figure from Jansen et. al. [10]. (d) The rupture strain γ_p decreases with increasing <z> in experiments (markers) and in simulations (lines). Adapted from Burla et. al. [3].

2.1.5. Stress relaxation mechanisms are important in weakly-crosslinked collagen networks

A complementary perspective to stress transmission is stress relaxation. The hierarchical and sub-isostatic network allows various ways for it to relax to an applied load over time. In collagen networks, these key mechanisms were found to play a significant role: fiber viscoelasticity, nonaffine network deformation, fibril lengthening, and transient crosslinking [30, 52, 59, 62]. Collagen networks deform non-affinely meaning that local deformations can differ from the applied macroscopic deformation (Figure 2.4a). Through nonaffine deformations, the strained network can minimize the energy of its configuration. Spatially heterogeneous stress distributions arising as a consequence of nonaffine rearrangements were imaged in collagen by boundary stress microscopy [30], digital volume correlation [32], and in fibrin networks using nonlinear Raman scattering [63]. The microstructure can influence the nonaffinity: simulations suggest that preferentially oriented network fibers can enhance the magnitude of nonaffine fluctuations compared to a randomly oriented network [64]. Monomers making up the fibrils can slip under strain (Figure 2.4b). In nature, this enables the mechanical adaptation of tissues to external loads at the macroscale. Significant fibril plasticity was demonstrated with uncrosslinked collagen under large-strain cyclic loading, where a shift in the stress-strain

curve was observed in subsequent cycles due to persistent fibril lengthening (Figure 2.4c) [52]. Finally, in the context of extracellular matrix remodeling, the densification of fibers around cells, persisting after the removal of cellular traction forces, is attributed to the formation of weak crosslinks between adjacent fibers under strain (Figure 2.4d) [65]. The degree of residual deformation increases with the duration of strain and concentration of collagen [59].

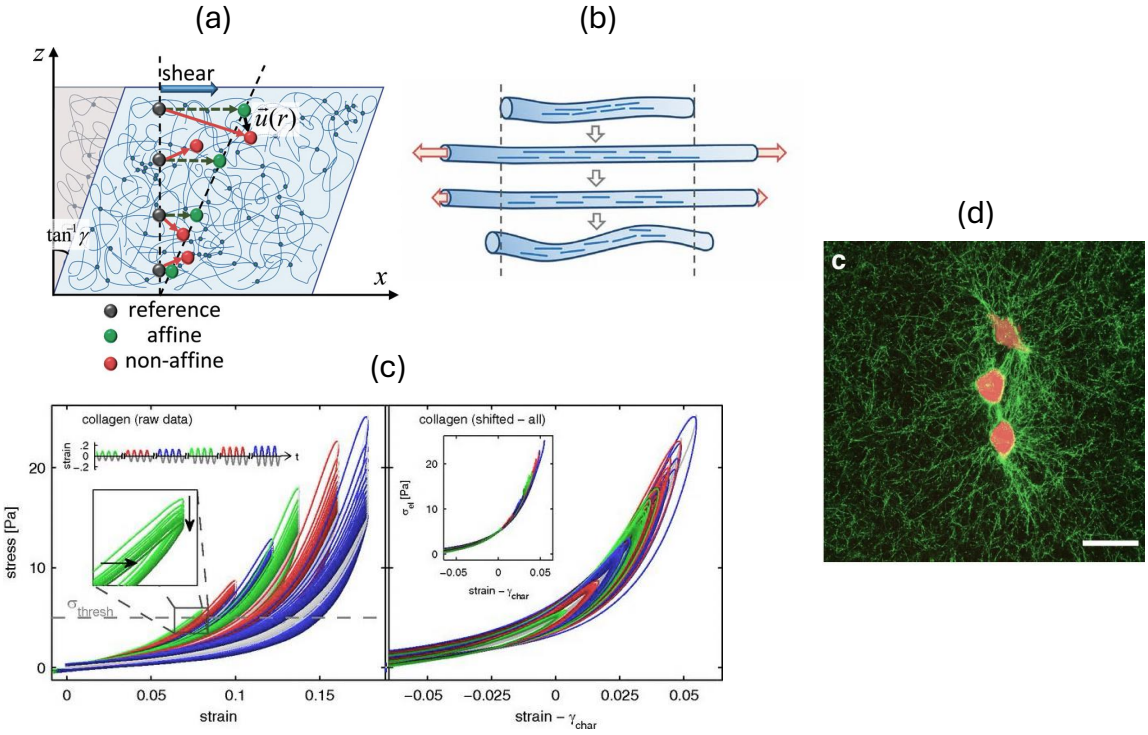

Figure 2.4: Stress relaxation mechanisms in collagen networks. (a) Schematic of a biopolymer gel under shear. The difference in the displacement of embedded tracer beads from the macroscopic shear deformation is quantified as the non-affine deviation $\vec{u}(r)$. Figure from Wen et. al. [66]. (b) Schematic of an uncrosslinked fiber under tension. The blue lines represent protofibrils. Plastic lengthening from the slippage of protofibrils under tension causes the rest length of the fiber to increase. Figure from Münster et. al. [52]. (c) Uncrosslinked collagen networks subject to large oscillatory strains with increasing amplitude, show a shift in their stress-strain response. The response can be collapsed onto a master curve by simple subtraction of a characteristic strain γ_{char}, defined as the strain at which the elastic midline of each loading-unloading curve reaches a specific threshold stress $\sigma_{el}(\gamma_{char}) = \sigma_{threshold}$. Figure from Münster et. al. [52]. (d) Confocal image of human breast cancer cells (MDA-MB-231) actively remodeling the surrounding collagen matrix forming dense fiber tracts. Red: Labeled MDA-MB-231 cells. Green: Reflectance signal of collagen. The scale bar represents 20 µm. Image from Kim et. al. [65].

2.1.6. Probing the time-dependent mechanics of collagen in the nonlinear regime

The relationship between microstructure and mechanics has mainly been explored in the context of elasticity for collagen networks. However, the large body of evidence suggests that viscoelasticity, inelasticity, and plasticity of collagen is equally important to consider, highlighting a gap in our understanding of the interplay between these time-dependent mechanisms and bulk shear mechanics. We hypothesize that collagen networks display time-dependent me-

chanical behavior, with microstructural differences potentially influencing the dynamics under load. Simulations also hint towards this: Burla et. al. show fibril- and network- level plasticity can fine-tune the rupture strain [3], and Ban et. al. highlight that fibril lengthening in the network increases the energy dissipated for the same magnitude of deformation [59].

To bridge the gap, in this chapter we explore the time-dependent bulk shear response of atelocollagen type I networks across the linear and nonlinear regime with a stress-controlled rheometer. Atelocollagen is a truncated form of the native telocollagen, where the terminal telopeptides are removed [67]. Since telopeptides are involved in forming strong covalent intra- and interfibrillar bonds, atelocollagen networks are weaker and more plastic, making them suitable for investigating the interplay of time-dependent mechanisms with the bulk shear mechanics. One of the challenges with collagen is that it varies structurally and mechanically depending on the animal species and body part that it was extracted from. Therefore, we first aim to characterize the mechanics of our collagen samples, prepared with different collagen concentrations and polymerization temperatures to vary the microstructure as in the first chapter, with measurements of their linear viscoelasticity and nonlinear elasticity. We investigate the time-dependent bulk shear response of collagen in the nonlinear regime using stress-controlled experiments. Finally, to capture the critical diverging signatures of simulated collagen networks predicted in literature, the experiments suggested by Shivers et al. are also tested [2].

2.2. Methods

2.2.1. Stress-controlled rotational rheometer

Shear tests are performed using the stress-controlled rheometer (Physica MCR 501, Anton Paar) and a stainless-steel cone-plate geometry with an angle of 1^o and diameter of 20 mm (part no. 3274, serial no. 16798, and 9034). A schematic of the test setup is shown in Figure 2.5. The rheometer controls the torque T applied through rotating the cone-plate head, and the associated shear stress σ at the sample-cone interface can be calculated based on the cone-plate geometry (Eq. 2.1). The shear strain γ is converted from the measured deflection angle θ of the head. As the cone angle α is small, we can approximate a linear increase in cone radius r with the gap height h, so the strain at the interface is constant and independent of h and r (Eq. 2.2, 2.3).

$$\sigma = \frac{3T}{2\pi R^3} \tag{2.1}$$

$$\gamma = \frac{r\theta}{h}, \quad tan(\alpha) = \frac{h}{r} \tag{2.2}$$

$$\gamma = \frac{\theta}{tan(\alpha)} \approxeq \frac{\theta}{\alpha} \tag{2.3}$$

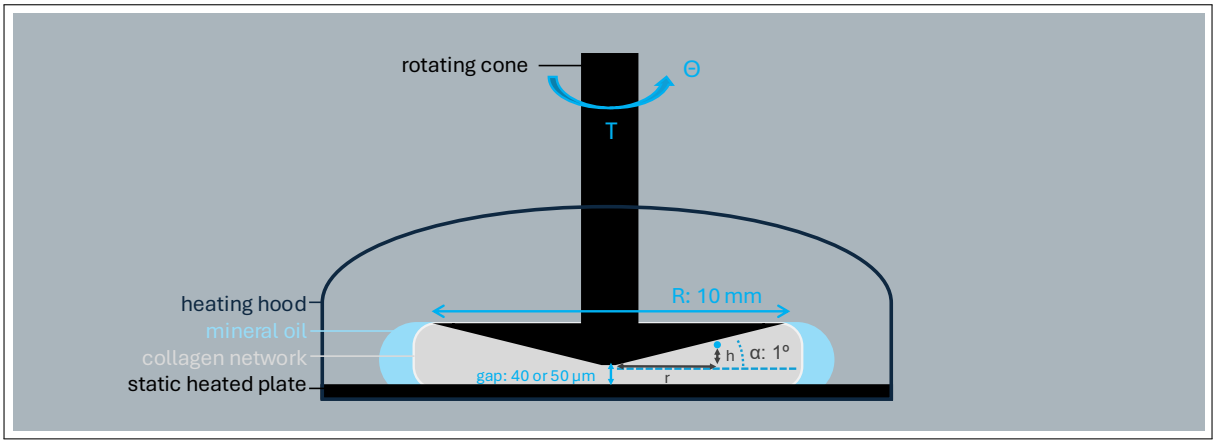

Figure 2.5: Schematic of the stress-controlled rheometer setup with a cone-plate geometry (cone angle $\alpha = 1^o$, diameter $d = 2R$). The collagen network polymerizes *in situ* between the heated cone-plate head and the bottom plate. The rheometer directly applies a torque T to the sample through rotation of the cone, and the resulting deflection angle θ is measured.

2.2.2. Rheology to probe the bulk shear mechanics of collagen networks

2.2.2.1. Collagen hydrogel preparation

First, collagen samples are prepared on ice by neutralizing bovine atelocollagen type I solution (catalog no. 5133, Biomatrix Fibricol, Advanced BioMatrix) in one part 10x PBS (pH 7.4, Gibco), 0.1M NaOH and MilliQ to the target collagen concentration (1.5, 2.5, 3.5 mg/ml) and to the target pH 7.4. The samples are mixed by pipetting up and down quickly for 30 times,

and the pH is double-checked with pH strips at the end of the sample preparation. The heating hood and bottom plate of the rheometer is set to the desired temperature for polymerization (26^{o}C, 30^{o}C, 37^{o}C). Then, 40 µL of sample is pipetted onto the pre-heated bottom plate and the cone is immediately lowered to the gap size of 40 or 50 µm corresponding to the specific head (Part no. 3274). Either 250 µL of mineral oil or 500 µL of 1x PBS is pipetted around the head to prevent sample dehydration. After the hood is lowered, polymerization of the network is monitored through the application of small shear strain sinusoidal oscillations $\gamma(t)$ with amplitude $d\gamma = 1\%$ around zero strain at the frequency of 1 Hz. The resulting oscillatory stress response $\sigma(t)$ is decomposed into the elastic in-phase and viscous out-of-phase component with δ as the phase lag from $\gamma(t)$, to obtain the shear storage G' and loss modulus G" (Eq. 2.4).

$$\begin{aligned} \gamma(t) &= d\gamma sin(wt) \\ \sigma(t) &= d\sigma sin(wt+\delta) = d\sigma(sin(wt)cos(\delta) + cos(wt)sin(\delta)) \\ \sigma(t) &= d\gamma(G'sin(wt) + G''cos(wt)) \\ G' &= \frac{d\sigma}{d\gamma}cos(\delta), \quad G'' = \frac{d\sigma}{d\gamma}sin(\delta) \end{aligned} \tag{2.4}$$

The polymerization duration is set to 90 minutes, 210 minutes, and 466 minutes for the temperature of 37^{o}C, 30^{o}C, and 26^{o}C, respectively, to ensure complete polymerization. During this period, G' and G" reach their plateau values (Appendix A.9). More noise is observed in the measured G' during polymerization when using the mineral oil compared to PBS.

2.2.2.2. Viscoelasticity in the low-strain regime and elasticity in the nonlinear regime

The viscoelastic response of the network in the linear elastic regime is probed through small oscillatory strains $d\gamma = 1\%$ applied around zero strain across the frequency range of ω = 0.01-10 rad/s, sampling two frequencies per decade (Figure 2.6a). The storage modulus G' and loss modulus G'' are measured as a function of frequency. To characterize the nonlinear elastic response of the network, a linearly increasing strain γ from 0-200% is applied at the shear strain rate of $\dot{\gamma}$ =0.1%/s, and the stress σ is measured with a sampling time of 1s/pt (Figure 2.6b). As demonstrated by Burla et al. [3], the ramp rate should not influence the elasticity measurements. The differential shear modulus $K = \frac{d\sigma}{d\gamma}$ is calculated from the slope of the stress-strain curve. The frequency sweep and strain-controlled ramp tests are performed consecutively on the same sample, with a ten-minute rest period in between during which the sample is held at 0% strain. The results of at least N=2 independent samples (and N=4 dependent samples) are shown for each test and collagen condition, unless stated otherwise.

2.2.2.3. Time-dependent nonlinear mechanics and second-order phase transition

The time-dependent deformation response is tested through a stress-controlled ramp, where networks are subjected to linearly increasing stress σ at the shear stress rate of $\dot{\sigma} = 0.1$, 1, or 10 Pa/s until failure, with the terminating condition of $\dot{\gamma}$ >100%/s (Figure 2.6c). Measurements of γ and $\dot{\gamma}$ are sampled every 0.25s. Yielding is defined at the point when the apparent viscosity $\eta(\sigma) = \frac{\sigma}{\dot{\gamma}}$ reaches its final maximum (excluding transient peaks at lower stresses). We repeatedly notice two sharp peaks in $\eta(\sigma)$ during the stress ramp tests. To investigate the robustness of these peaks, a cyclic loading experiment with 6 cycles of loading-unloading without intervening waiting time, at the loading rate of $\dot{\sigma} = 1$ Pa/s, with an increasing final stress

magnitude (20, 30, 50, 70, 90, 110 Pa) is carried out (Figure 2.6d).

To capture the second order mechanical phase transition and its critical signatures, we test the pre-strain frequency sweep tests and pre-strain stress relaxation tests proposed by Shivers et al. [2] (Figure 2.6e, Appendix A.25). For the pre-strain frequency sweep test, frequency sweeps are performed at stepwise increasing pre-strains ($\gamma_0 = 0\%$, 5-20% in 1% steps, 25%) encompassing the expected critical strain at around 16% based on strain ramp data. The strain ramp at the rate of $\dot{\gamma} = 0.1\%/s$ is used to go from the previous to the next pre-strain value, followed by a $500s$ hold at the new pre-strain to equilibrate the system, and then an oscillatory strain of amplitude $d\gamma = 0.5\%$ is superimposed on γ_0 for the frequency range of $\omega = 0.01 - 10$ rad/s sampling two frequencies per decade (Figure 2.6e). Zero-shear viscosity $\eta_0^{''}(\gamma_0)$ is determined as the limit of dynamic viscosity $\eta^{''}(\omega, \gamma_0) = \frac{G^{''}(\omega,\gamma_0)}{\omega}$ as ω approaches zero as defined in Shivers et al. (Eq. 2.5) [2].

$$\eta_0^{''}(\gamma_0) = \lim_{\omega \to 0} \eta^{''}(\gamma_0, \omega) \approxeq \eta^{''}(\gamma_0, \omega = 0.01) \tag{2.5}$$

Since crosslinking dynamics are not considered in the simulated networks of Shivers et. al., we experimentally test both uncrosslinked and glutaradehyde (GA)-crosslinked collagen networks [2]. For crosslinking, the network polymerizes for 45 minutes with 1x PBS. Then, the hood is lifted and a solution of GA in 1x PBS is added around the head before lowering the hood again. Polymerization in the presence of 0.001% (w/v) GA is monitored for the next three hours during which G' and G'' reach new plateau values (Appendix A.22. The pre-strain frequency sweep is then carried out following the same protocol.

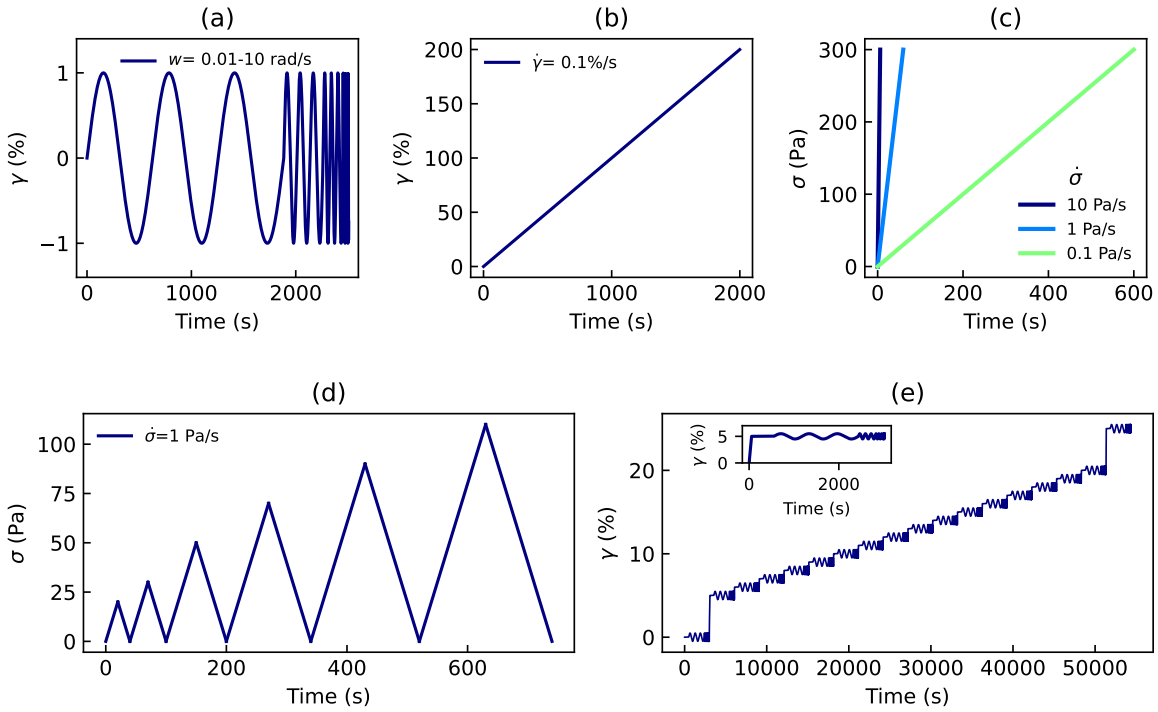

Figure 2.6: Overview of the rheology protocols used in the study. (a) Frequency sweep test. (b) Strain-controlled linear ramp test. (c) Stress-controlled linear ramp test. (d) Cyclic stress ramp test. (e) Pre-strain frequency sweep, proposed by Shivers et al. [2],. A linear ramp at the shear strain rate of $\dot{\gamma} = 0.1\%/\text{s}$ brings the sample to the new pre-strain value γ_0. The sample is equilibrated with a 500s hold at γ_0. Then an oscillatory strain of amplitude $d\gamma = 0.5\%$ is superimposed on γ_0 for the frequency range of $\omega = 0.01 - 10$ rad/s sampling two frequencies per decade. Inset: closer view of the frequency sweep carried out at $\gamma_0 = 5\%$.

2.2.3. Data analysis

Through the strain ramp test, unique stress-strain curves are obtained for different collagen microstructures. Their nonlinear elastic properties are quantified by extracting three characteristic strains: the onset strain γ_o marking the start of nonlinearity; the critical strain γ_c where a transition from bending to stretching-dominated rigidity is expected; and the rupture strain γ_r when fibers begin to break. γ_o is determined as the inflection point in $\frac{dK}{d\gamma}$, corresponding to the strain where the second derivative $\frac{d^2K}{d\gamma^2}$ has a maximum (Figure 2.7). The derivative is computed with the numpy gradient function in Python. γ_c is defined as the inflection point of $K(\gamma)$ corresponding to the strain where the first derivative $\frac{dK}{d\gamma}$ has a maximum. This is taking a similar definition as Jansen et. al. [10], but without the logarithm as it is found to be numerically unstable with the strain ramp data. $\gamma_r = \max_\gamma \sigma(\gamma)$ is defined as the strain where the stress σ reaches a maximum. All the data and subsequent derivatives are smoothened using a Gaussian kernel function before deriving the quantities.

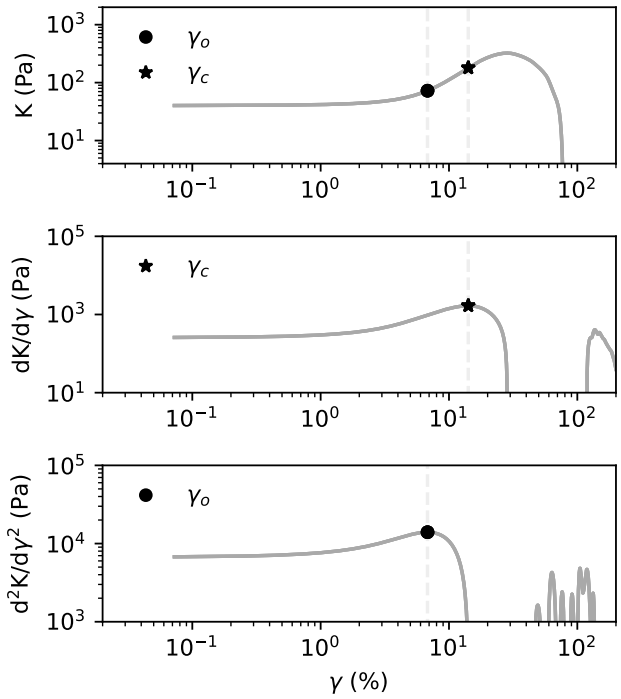

Figure 2.7: Determination of the onset and critical strain from the strain ramp data. A representative sample of the 3.5 mg/mL atelocollagen networks polymerized at 37^{o}C is shown. The differential modulus K is defined as $\mathrm{K} = \frac{d\sigma}{d\gamma}$. The onset strain γ_o (circle symbol) is determined as the inflection point in $\frac{dK}{d\gamma}$, corresponding to the strain where the second derivative $\frac{d^2K}{d\gamma^2}$ has a maximum. The critical strain γ_c (star symbol) is determined as the inflection point of $K(\gamma)$, corresponding to the strain where the first derivative $\frac{dK}{d\gamma}$ has a maximum.

The yield stress σ_y in the stress ramp test is defined as the stress where $\eta(\sigma)$ has the final maximum value. For the loading rate of $\dot{\sigma} = 10$ or 1 Pa/s, the yield point is extracted by computing the numerical derivative of $\eta(\sigma)$ and finding the final datapoint where $\frac{d\eta(\sigma)}{d\sigma} < 10^{-3}$s. For the loading rate of $\dot{\sigma} = 0.1$ Pa/s, the noise in the data affects the stability of the numerical derivative. Instead, a polynomial curve of degree 2 is fitted to the datapoints using the numpy polyfit function, and the maximum in the fitted curve is taken as the yield point. We define the peak strain $\gamma_p = \max_\gamma K(\gamma)$ as the strain where $K(\gamma)$ has a maximum.

2.3. Results

2.3.1. Viscoelasticity in the low strain linear regime

We sought to characterize the viscoelasticity of different collagen microstructures in the low-strain regime by subjecting them to a frequency sweep, consisting of small strain oscillations dγ=1% over the range of ω = 0.01-10 rad/s. Collagen gels are prepared the same way as in the first chapter of the thesis (Figure 1.7), by adjusting the collagen concentration (1.5, 3.5 mg/mL) and the polymerization temperature (26^{o}C, 30^{o}C, 37^{o}C) to create different network microstructures.

The measured G' and G'' of the networks are presented in Figure 2.8a,b. An increase of slightly less than half a decade is observed for G' and G'' across the frequency range. G' is consistently an order of magnitude larger than G'', demonstrating the networks are dominantly elastic in the low strain regime. G' is larger for the networks polymerized at the temperature of 26^{o}C and 30^{o}C (3.5 mg/mL: G'(ω =0.01) = 53 Pa, 42 Pa, respectively) compared to at 37^{o}C (3.5 mg/mL: G'(ω=0.01)= 28 Pa), which tells us that the networks polymerized at lower temperatures are more stiff.

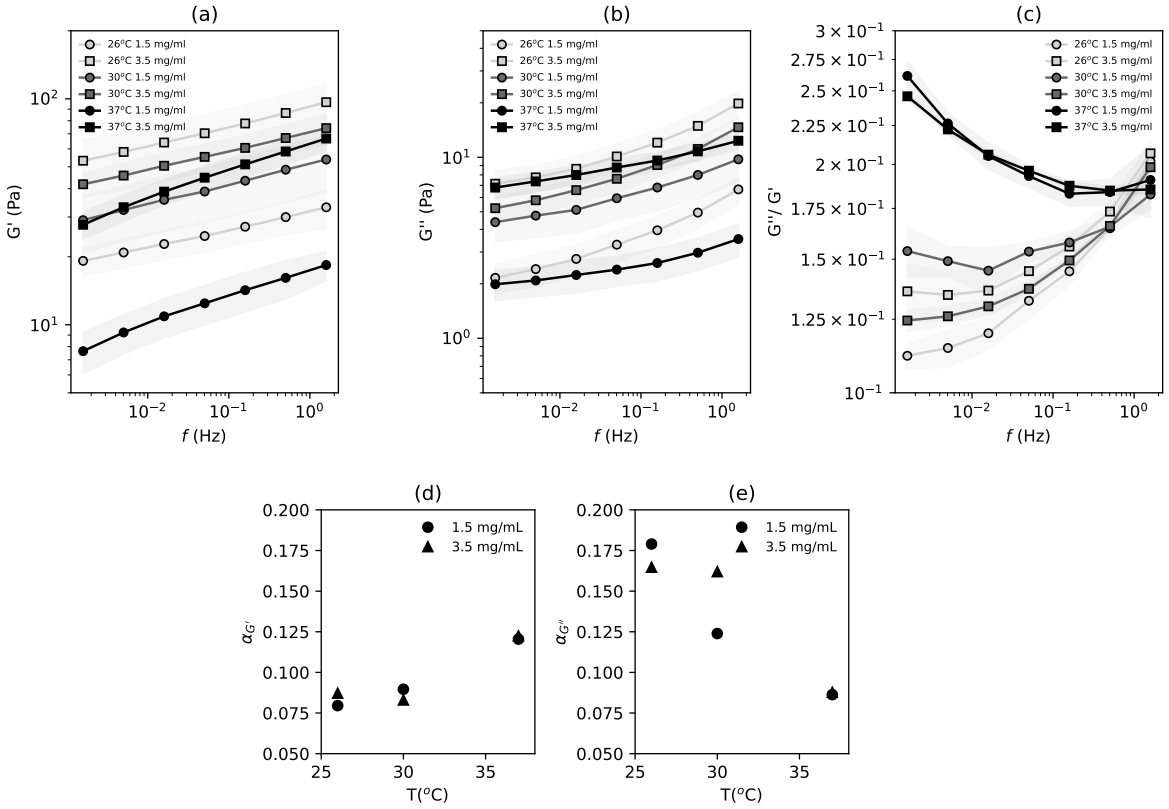

Figure 2.8: Frequency sweep to probe the frequency dependence of G' and G" in the linear regime. (a) The average storage modulus G', (b) loss modulus G'', and (c) loss tangent G''/G' plotted as a function of f. The error bars represent the standard deviation for N=4 (1.5 mg/mL polymerized at 26, 30, 37^{o}C; 3.5 mg/mL polymerized at 26^{o}C), N=3 (3.5 mg/mL polymerized at 30^{o}C), and N=2 samples (3.5 mg/mL polymerized at 37^{o}C). (d-e) The fitted power law exponent α to the curves in (a-b).

Notably, from the slope we see that the frequency dependence of G' and G" appears qualitatively different for the networks polymerized at 37^{o}C compared to the networks polymerized at 26^{o}C and 30^{o}C. To investigate this trend, the loss tangent G"/G', defined as the ratio of the viscous and elastic component, is plotted in Figure 2.8c. For both 26^{o}C and 30^{o}C networks, the loss tangent is initially smaller, suggesting that these networks are more elastic. G"'/G' displays a marked increase with higher strain rates, which is expected due to dissipation by the fluid phase. The network at 37^{o}C shows the opposite trend and is initially more viscous, and becomes more elastic at higher frequencies. We quantified this observation by fitting a power law with exponent α to describe the slope of G' and G" with f on the log-log plot (Figure 2.8 d,e). We find that at 26^{o}C and 30^{o}C, $\alpha_{G'}$ is smaller than $\alpha_{G''}$, and at 37^{o}C $\alpha_{G''} < \alpha_{G'}$. These results highlight the strong viscoelastic behavior of the networks polymerized at 37^{o}C, where it displays a softer, more viscous response at lower frequencies and stiffer elastic response at higher frequencies. It is important to mention that we noticed retrospectively that the strain of 1% lies in the linear elastic regime for the networks polymerized at 37^{o}C, but for the networks polymerized at 26^{o}C and 30^{o}C, 1% lies closer to the nonlinear elastic regime (3.5 mg/mL: onset strain γ_o =0.7% and 1.0%, respectively, Figure 2.10).

2.3.2. Elasticity in the linear and nonlinear regime

We characterize the linear and nonlinear elasticity of the collagen samples by carrying out a strain-controlled ramp at the strain rate of $\dot{\gamma} = 0.1\%/s$ for γ =0-200%. In Figure 2.9a, an overview of the stress-strain response of all the samples is shown. The stress is initially low at small strains, and grows quickly as the network stiffens at intermediate strains. The stress reaches a peak at high strain, beyond which the stress rapidly drops indicating network fracture. The peak location is clearly distinct between the temperature conditions. Within a temperature condition, the different collagen concentrations result in differences in the peak height. To quantitatively describe the elasticity of the different collagen microstructures, the differential modulus $K = d\sigma/d\gamma$ is computed. We show K as a function of strain in Figure 2.9b for the networks polymerized at 37^{o}C. The curve $K(\gamma)$ can be split into different elastic regimes, defined by three characteristic strains. At low strains, the stress increases linearly with strain, so the differential modulus remains constant (Figure 2.9b). Beyond the onset strain γ_o (triangle marker), which is defined as the inflection point in $dK/d\gamma$, the network strain-stiffens as indicated by the upturn in the curve. The nonlinear regime can be distinguished into two parts, the bend-dominated and stretch-dominated regime as the region before and after the critical strain γ_c (circle marker), defined as the inflection point of $K(\gamma)$, respectively. Finally, the rupture strain γ_r is defined as the strain where the stress reaches its maximum value.

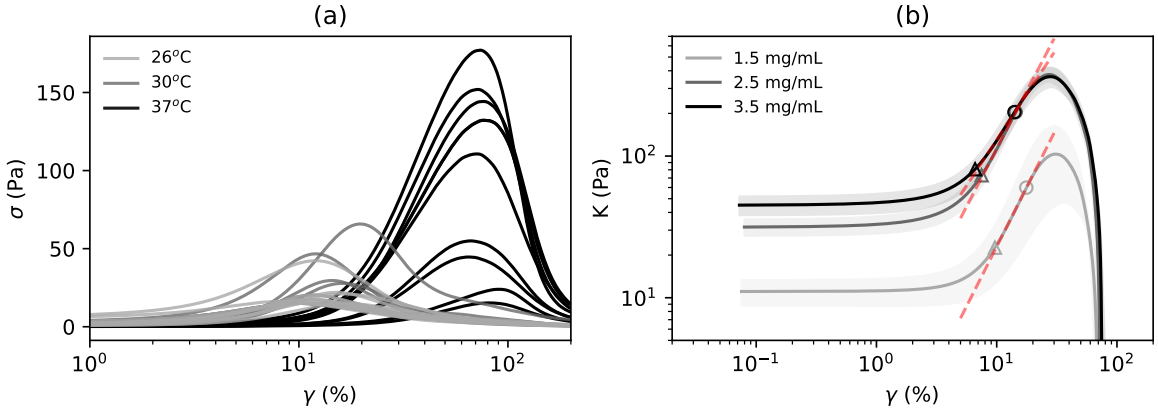

Figure 2.9: Strain ramp to characterize the nonlinear elasticity of collagen. (a) The stress as a function of strain of collagen networks during the strain ramp at $\dot{\gamma} = 0.1\%/s$. Each curve corresponds to a single sample, and for each polymerization temperature, samples of different collagen concentrations (1.5, 2.5, and 3.5 mg/mL) are plotted. (b) The average differential modulus K plotted as a function of γ for networks polymerized at 37^{o}C with different collagen concentrations (N = 2, 3, 4 samples for 1.5, 2.5, and 3.5 mg/mL, respectively). The onset of stiffening γ_o is marked with a triangle and the critical strain γ_c is marked by a circle. The shaded area represents the standard deviation between samples. The degree of stiffening in the first part of the nonlinear regime, between γ_o and γ_c, is quantified by fitting a power law with exponent β to the curve as shown by the red dashed line.

The average γ_o, γ_c, and γ_r values for different collagen concentrations and polymerization temperatures are summarized in Figure 2.10a,b,c. We find that the characteristic strains are strongly correlated with the temperature, with a weak concentration-dependence. The networks polymerized at 37^{o}C stiffen and rupture at the largest strains (3.5 mg/mL: γ_o : $6.6 \pm 0.2\%$, γ_c : $14.0 \pm 0.1\%$, $\gamma_r = 77.9 \pm 3.4\%$). In contrast, the difference between networks polymerized at 26^{o}C and 30^{o}C is small, and the networks stiffen and rupture at much lower strains (3.5 mg/mL polymerized at 26^{o}C: γ_o : $0.7 \pm 0.4\%$, γ_c : $1.4 \pm 0.8\%$, $\gamma_r = 10.4 \pm 1.8\%$; 3.5 mg/mL polymerized at 30^{o}C: γ_o : $1.0 \pm 0.4\%$, γ_c : $2.1 \pm 0.7\%$, $\gamma_r = 10.1 \pm 0.8\%$). The stiffening degree in the bending-dominated nonlinear elastic regime is quantified by fitting a power law with exponent β to $K(\gamma)$ between γ_o and γ_c, as demonstrated in Figure 2.9b with the dashed red line. The average stiffening exponent β for each polymerization temperature and collagen concentration is shown in Figure 2.10d. β shows a small temperature- and concentration- dependence: β decreases with increasing collagen concentration, and decreases with lower polymerization temperatures.

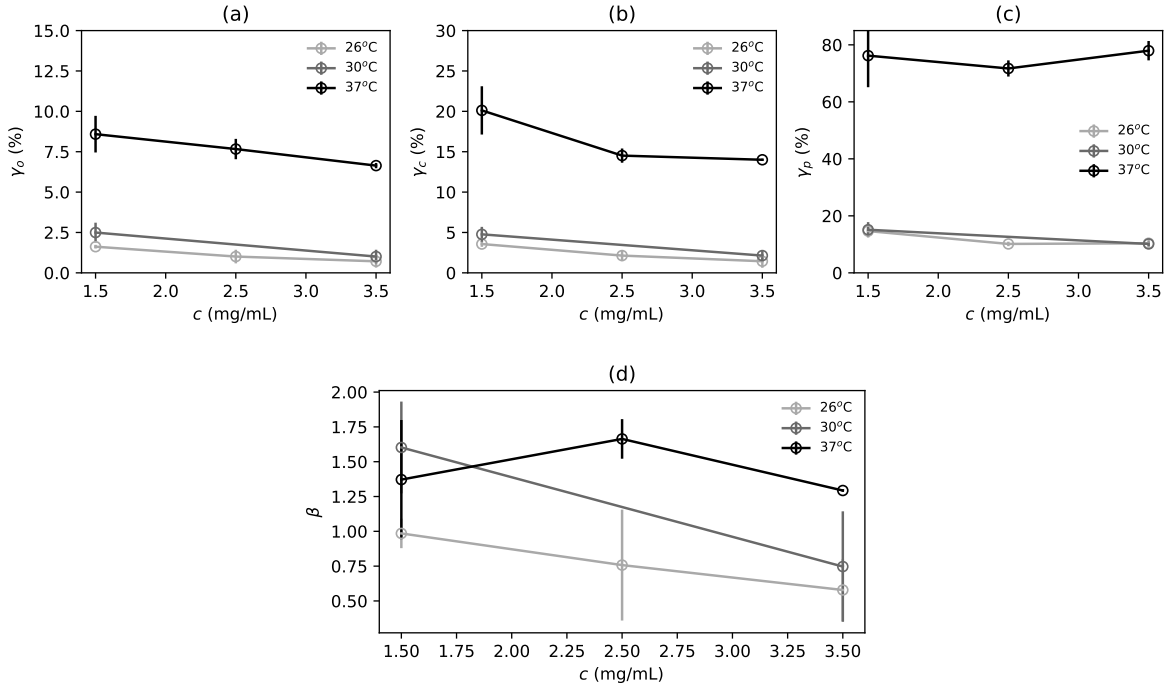

Figure 2.10: Characteristic strains strongly depend on polymerization temperature and weakly depend on concentration, while the stiffening exponent weakly depends on both polymerization temperature and concentration. (a-c) The onset strain γ_o, critical strain γ_c and rupture strain γ_r as a function of the collagen concentration. The averages are shown over N=3 samples for 2.5 mg/mL polymerized at 26^{o}C or 37^{o}C, and 3.5 mg/mL polymerized at 30^{o}C or N=2 samples for 3.5 mg/mL polymerized at 37^{o}C, and the rest for N=4 samples. The error bars represent the standard deviation between samples. (d) The average stiffening exponent β determined by fitting the $K(\gamma)$ curve between γ_o and γ_c for each sample is plotted here as a function of the collagen concentration. The error bars represent the standard deviation.

2.3.3. Time-dependent nonlinear mechanics and second-order phase transition

In the previous sections, we focused on characterizing the viscoelasticity in the low strain linear regime, and the nonlinear elasticity of the collagen networks. However, a notion of their stress- and time- dependent response to loading is missing from these experiments. To investigate this further, we subject the networks to a linear stress ramp: here the strain rate is not controlled, which enables us to observe the dynamics of the network deformation. In Figure 2.11 (left panel), we show the deformation rate $\dot{\gamma}$ as a function of time for the ramp at the loading rate of $\dot{\sigma} = 1$ Pa/s, for a representative sample of the four different microstructures. The curves show that $\dot{\gamma}$ is non-monotonic during the test: $\dot{\gamma}$ is larger at the start when the collagen network elastically responds to low stresses. Then $\dot{\gamma}$ shows a sudden drop and recovery, after which it further decreases as the network stiffens. The test ends with a sudden spike up in $\dot{\gamma}$ indicating complete network failure.

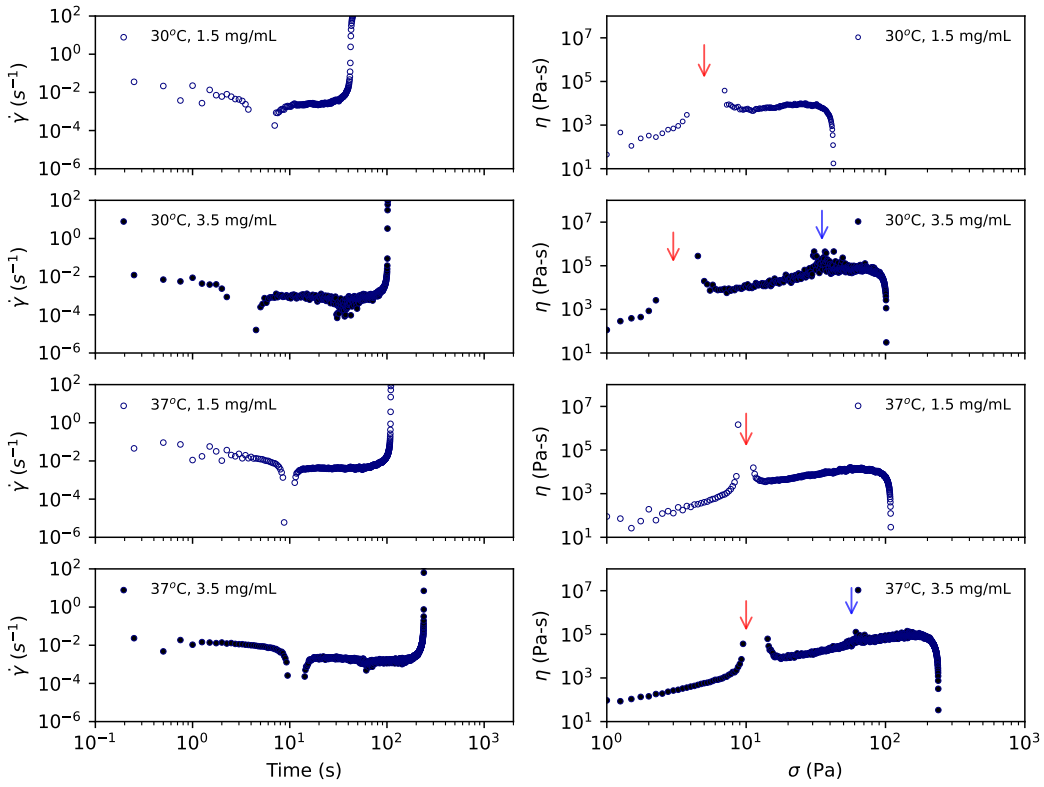

Figure 2.11: Non-monotonic strain rate during the stress ramp with two peaks in dissipation. The strain rate $\dot{\gamma}$ as function of time (left panel), and the apparent viscosity η as a function of stress σ (right panel) during the ramp at $\dot{\sigma} = 1$ Pa/s is shown here for a single representative sample for each collagen microstructure. The red and the blue arrow point at the first and the second identified peak in dissipation, respectively.

We show the apparent viscosity, defined as $\eta(\sigma) = \frac{\sigma}{\dot{\gamma}}$, as a complementary representation of the network response (right panel, Figure 2.11). η increases with σ, indicating that the gel shear-thickens. Yielding of the network is defined as the point where η rapidly decreases. The distinct drop we saw in $\dot{\gamma}$ manifests as a peak in η (see red arrows), which occurs consistently at a similar stress magnitude corresponding to a given microstructure. This peak shares a strikingly similar shape to the critical signature found in the simulations of Shivers et. al. [2]. For

the high concentration conditions, we also notice a second peak in η at a higher stress magnitude (see blue arrows), most prominently at 30^{o}C. The second peak also occurs consistently at a similar stress magnitude for a given condition.

The reproducibility of the two peaks in dissipation across samples within one condition suggests that these peaks represent well-defined mechanical states of the network. To investigate the nature of both peaks, we check where they lie within the elastic regimes described earlier. We plot $\eta(\gamma)$ and $K(\gamma)$ for all loading rates, for the 3.5 mg/mL networks polymerized at 30^{o}C in Figure 2.12a, and at 37^{o}C in Figure 2.12b. Each curve represents a separate sample, and the critical strain γ_c and peak strain γ_p in K are marked by a star and a square, respectively. Although γ_c is ill-defined for some samples, especially at the loading rate of $\dot{\sigma} = 10$ Pa/s, we find that the first peak coincides well with the critical strain (Figure 2.12), suggesting that this peak represents the second-order phase transition that has been observed in the simulations of Shivers et. al. [2]. The second peak coincides with the peak in the differential modulus.

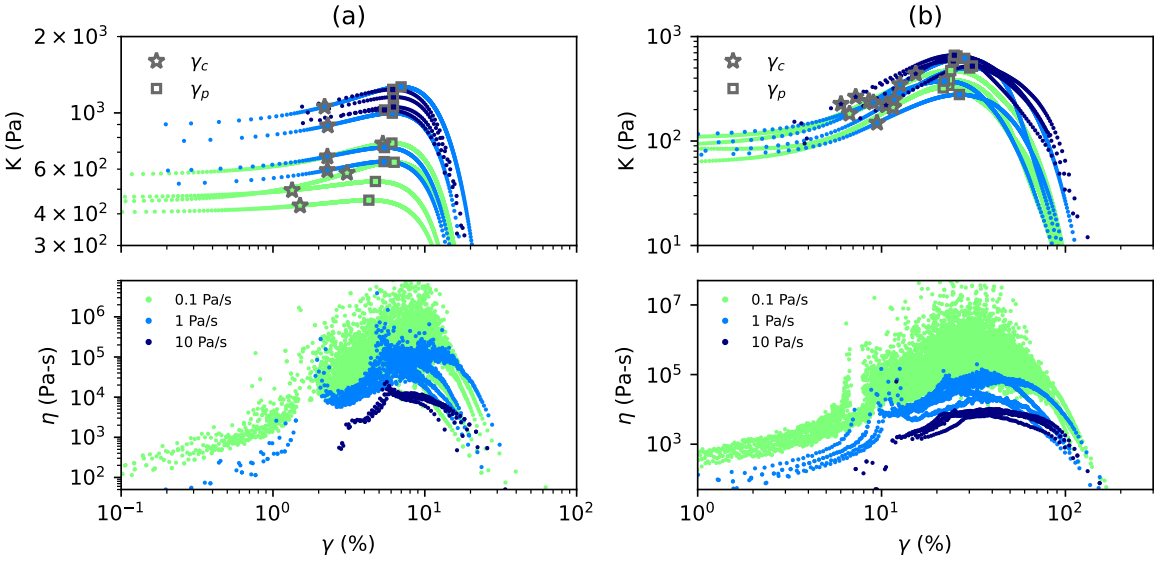

Figure 2.12: The first peak and second peak in dissipation occur, respectively, at the inflection point and peak of the differential modulus. The differential modulus K and the apparent viscosity η plotted as a function of γ for the stress ramps at the loading rate of $\dot{\sigma} = 10$, 1, and 0.1 Pa/s. (a) for the 3.5 mg/mL networks polymerized at 30^{o}C, (b) for the 3.5 mg/mL networks polymerized at 37^{o}C. The critical strain γ_c (star symbol) is defined as the strain at the inflection point in K(γ), or maximum in $\frac{dK(\gamma)}{d\gamma}$, and the peak strain γ_p (square symbol) is the strain where K is maximal. Each curve represents a single sample. N=4 samples are shown for each loading rate.

To characterize the peak in η at criticality for comparison to simulation findings, we manually determine the two nearest datapoints flanking the divergence. All the strain values in between the two datapoints are possible values of the divergence strain γ_d. We plot η for the points $\gamma < \gamma_d$ of a representative sample for all possible γ_d, with the ramp loading rate of $\dot{\sigma} = 0.1$ Pa/s in Figure 2.13a, and $\dot{\sigma} = 1$ Pa/s in Figure 2.13b. Simulations from Shivers et. al. describe the critical power law scaling relation as $\eta_0 - \eta_f \propto |\gamma - \gamma_c|^{-\lambda}$, where η_0 is the zero-shear viscosity, η_f is the fluid viscosity, γ_c is the strain at onset of rigidity, with the exponent $\lambda = 1.5$ [2]. For our data, we fit λ to the points close to γ_d (highlighted in color), which is $|\gamma - \gamma_d| \leq 2\%$ or $|\gamma - \gamma_d| \leq 2.5\%$ in Figure 2.13a,b, respectively, according to the experimental scaling relation $\eta \propto |\gamma - \gamma_d|^{-\lambda}$. As shown in the plots (Figure 2.13a,b), the shape of the curve is sensitive to the choice of γ_d, and different possible γ_d results in different values of the fitted λ. We define the best fit λ as the λ which minimizes the weighted mean square error WMSE in the fitting close to the divergence, and maximizes the WMSE in the fitting including datapoints outside the divergence. The approach is described in more detail in Appendix A.15. In Figure 2.13c, we summarize the best fit λ for the 3.5 mg/mL networks polymerized at 37^{o}C. λ is more robustly determined at the loading rate of $\dot{\sigma} = 1$ Pa/s with a small standard deviation ($\lambda = 1.5 \pm 0.1$), and shows good agreement with theory. For the 1.5 mg/mL networks polymerized at 37^{o}C, and the networks polymerized at 30^{o}C, there are too few data points at the divergence to determine λ using the same approach.

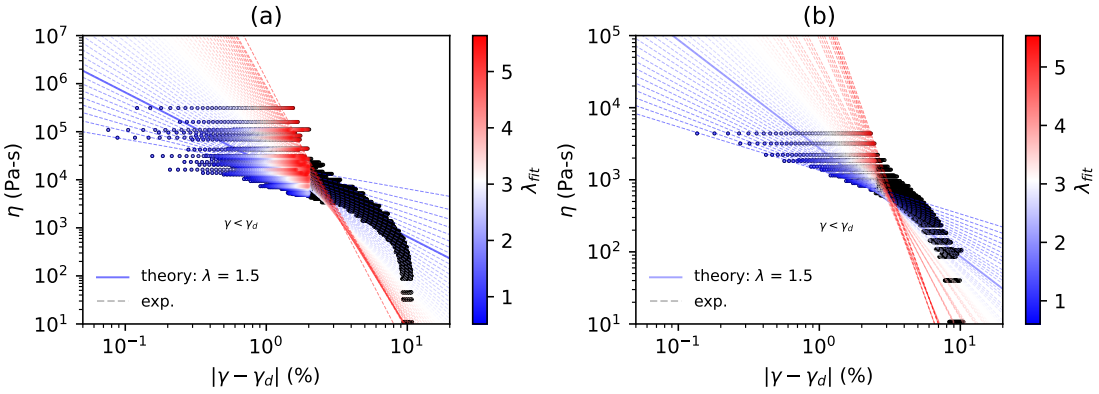

(c)

$\dot{\sigma}$ (Pas^{-1})	**Fit** λ
1	1.5 ± 0.1 (N=4)
0.1	1.1 ± 0.3 (N=4)

Figure 2.13: Experimental fit of the divergence in apparent viscosity at criticality. (a-b) The apparent viscosity η of a 3.5 mg/mL atelocollagen network polymerized at 37^{o}C subject to the stress ramp at $\dot{\sigma} = 0.1$ Pa/s (a) and $\dot{\sigma} = 1$ Pa/s (b). The black markers represent the datapoints where $\gamma < \gamma_d$, shown for all possible values of the divergence strain γ_d between the manually determined nearest two datapoints flanking the divergence in viscosity. The datapoints $|\gamma - \gamma_d| \leq 2\%$ are fitted in (a), and the datapoints $|\gamma - \gamma_d| \leq 2\%$ are fitted in (b),to determine the critical exponent λ defined as $\eta \propto |\gamma - \gamma_d|^{-\lambda}$. A different λ_{fit} is obtained for each value of γ_d, shown with the dashed line. The theoretical fit from the simulations of Shivers et. al. with $\lambda = 1.5$ is plotted as the solid line [2]. (c) The best fit λ for the 3.5 mg/mL networks polymerized at 37^{o}C is determined as the λ which minimizes the weighted mean square error WMSE in the divergence region, and maximizes the WMSE beyond the divergence (see Appendix A.15 for details).

Assuming that the first peak represents a second order mechanical phase transition, the first peak in viscosity should be fully reversible. The second peak takes place before softening or yielding of the network, suggesting that the peak can occur repeatedly. To assess the both peak reproducibility, a cyclic loading experiment is carried out on 3.5 mg/mL networks polymerized at 37^{o}C. Here we apply 6 cycles of the stress ramp at $\dot{\sigma} = 1$ Pa/s, with each loading cycle reaching an increasing final stress of 20, 30, 50, 70, 90, and 110 Pa (Figure 2.14). These magnitudes are chosen to just capture the first peak with $\sigma > 10$ Pa and eventually reach the second peak with $\sigma > 70$ Pa. $K(\gamma)$ and $\eta(\gamma)$ during the loading part of each cycle are plotted in Figure 2.15a,b, respectively, for a single representative sample. The test confirms the reproducible presence of the first and second peak: the first peak is observed in all 6 cycles, while the second peak appears in the last three cycles when the final stress magnitude reaches higher than 70 Pa. The second peak appears to grow more prominent between cycles 4, 5, and 6. The maximum in K evolves with each loading cycle (370 Pa to 1600 Pa).

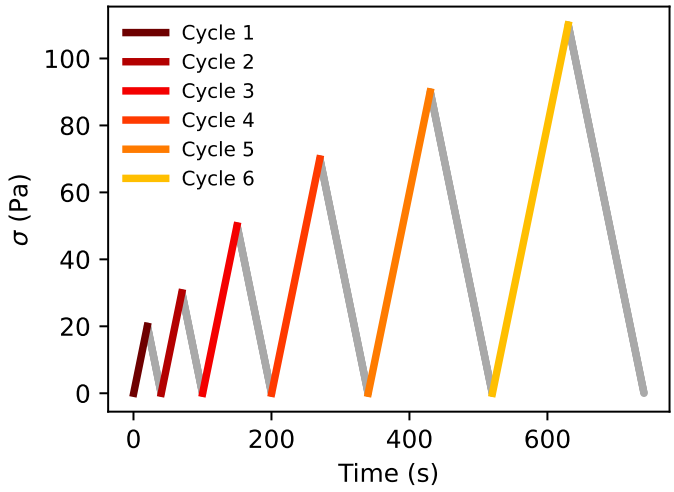

Figure 2.14: The cyclic loading protocol where 6 cycles of the stress-controlled ramp at $\dot{\sigma} = 1$ Pa/s with increasing final stress magnitude in each cycle (20, 30, 50, 70, 90, 110 Pa) are imposed on the sample.

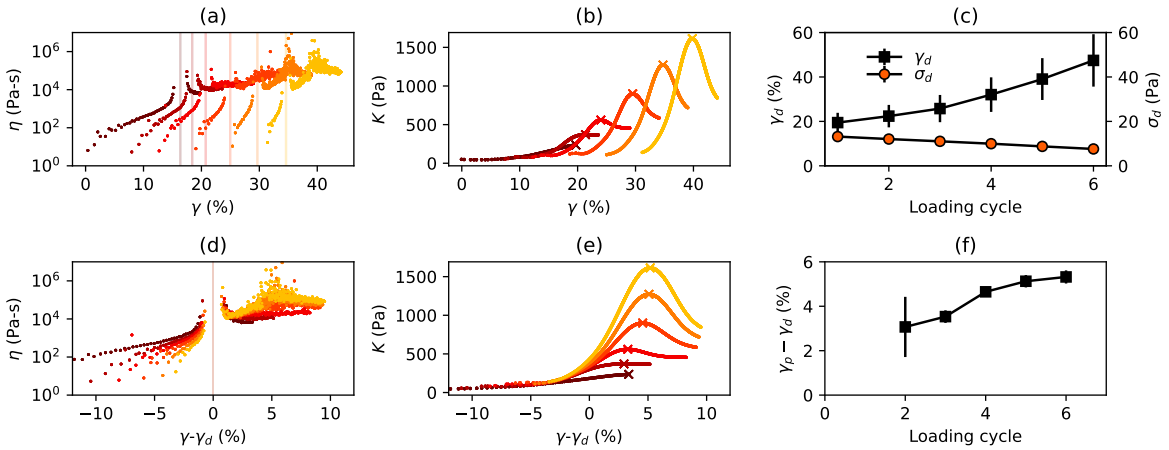

Figure 2.15: First and second peak in dissipation occur robustly under cyclic loading. Figure 2.14 shows the cyclic loading protocol used. The results of a single representative sample for 3.5 mg/mL atelocollagen networks polymerized at 37^{o}C is shown in (a,b,d,e), for the loading part of each cycle (marker color follows from Figure 2.14 and represents the cycle number). (a) η is plotted as a function of γ. The divergence strain γ_d where the first peak in dissipation occurs (shown as a solid line) is manually determined by selecting the nearest two points flanking the divergence and taking the mean. (b) The differential modulus K is plotted as a function of γ, and the peak in K is marked by a cross. (c) The average γ_d and the corresponding $\sigma_d = \sigma(\gamma_d)$ in each loading cycle (N=5 samples). (d) Subtraction of γ_d from the curve $\eta(\gamma)$ leads to a collapse of the first peak in dissipation for all cycles. (e) Subtraction of γ_d from $K(\gamma)$ shifts the curves without collapse. (f) The distance between γ_d and the peak strain γ_p in each loading cycle (N=5 samples). The error bar in (c,f) represents the standard deviation.

At the end of each cycle, the network is brought back to $\sigma = 0$ Pa. However, there is a large shift in the starting strain for each subsequent cycle (from 0% to 31%). This is accompanied by a shift in the divergence strain γ_d where the first peak in η occurs. γ_d is estimated here by taking the mean strain of the two closest datapoints flanking the divergence. In Figure 2.15c, we show the average γ_d and the associated $\sigma_d = \sigma(\gamma_d)$ for each loading cycle over N=5 samples. γ_d shows large variability between samples and increases by 28% from the first ($19 \pm 4\%$) and last cycle ($47 \pm 12\%$). On the other hand, σ_d decreases slightly from the first (13.2 ± 1.1 Pa) to the last cycle (7.59 ± 0.67 Pa) with little variability between samples. In Figure 2.15d,e, we shift the $\eta(\gamma)$ curves by subtracting γ_d, leading to a collapse of the first peak in viscosity for all cycles. The shifted $K(\gamma)$ curves do not entirely collapse as function of γ (Figure 2.15e), suggesting that the mechanical trajectory in each cycle is qualitatively different. In Figure 2.15f, we plot the distance between the divergence strain γ_d and peak strain γ_p, which slightly increases with each loading cycle.

While the first peak likely captures the critical slowing down of the network, the second peak at the maximum of the differential modulus K has not been described in previous works. We speculated on the origins of the second peak, which manifests at the end of the stretching-dominated nonlinear regime. Prior works have shown that collagen networks develop a load-bearing subnetwork past the critical strain [60]. Considering that the second peak in dissipation occurs when the sub-network is maximally stretched and stiffened, we hypothesize that plastic fibril lengthening may provide the network with an additional degree of freedom to redistribute stress.

To explore this possibility, we carry out the linear stress ramp until failure, and the cyclic loading experiment on 3.5 mg/mL telocollagen networks polymerized at 37^{o}C (Figure 2.16). Telocollagen monomers contain the terminal telopeptide which is able to create much stronger covalent intra-fibrillar crosslinks compared to atelocollagen, and thus is expected to show reduced fibril-level plasticity [3]. Telocollagen networks show no visible second peak in dissipation during the linear stress ramp at the loading rate of $\dot{\sigma}$= 1 Pa/s (Figure 2.16a). In the cyclic loading protocol, the first peak in dissipation is similarly reproduced in every cycle, whereas the second peak does not appear prominently in any cycle (Figure 2.16b, Appendix A.17). However, there is again substantial residual strain after unloading, reaching 39% in the last cycle. The plot of $K(\gamma)$ shows a similar increasing maximum stiffness reached in each cycle as observed for atelocollagen networks. The increase in K (180 Pa to 770 Pa) is less than observed for atelocollagen.

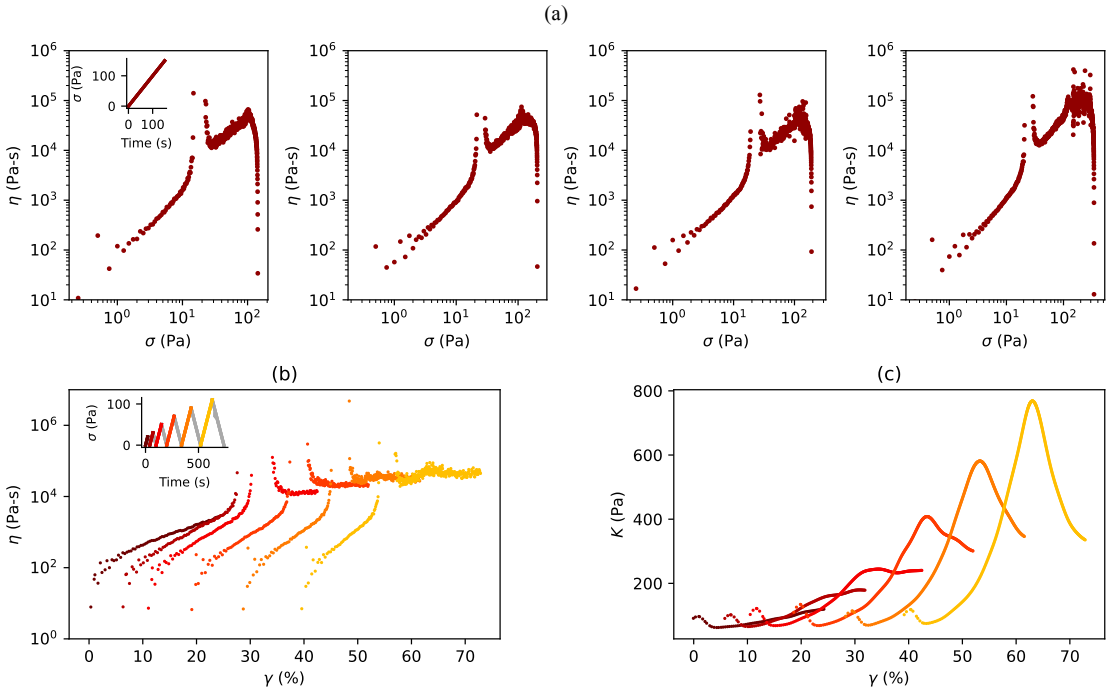

Figure 2.16: The second peak in dissipation is suppressed in telocollagen networks. (a) η as a function of σ during the stress ramp with loading rate of 1 Pa/s for 3.5 mg/mL telocollagen networks polymerized at 37^{o}C (N=4). Inset shows the loading protocol. (b-c) The results of the cyclic stress ramp experiment for a single representative sample for 3.5 mg/mL telocollagen networks polymerized at 37^{o}C. (b) η as a function of γ is plotted for the loading part of each cycle. The inset shows the loading protocol, where we impose 6 cycles of a linear stress ramp at 1 Pa/s with increasing final stress magnitude (20, 30, 50, 70, 90, 110 Pa) on the sample. (c) The differential modulus K is plotted as a function of the strain γ for the loading part of each cycle.

Lastly, we want to see whether the atelocollagen network's dynamic response to stress varies with the experiment timescale, so the stress ramp is conducted at three different loading rates ($\dot{\sigma}$ = 0.1, 1, 10 Pa/s). In Figure 2.17a, $\eta(\sigma)$ is plotted for 1.5 mg/mL atelocollagen networks polymerized at 37^{o}C. We observe a decrease in the yield viscosity η_y, defined as the maximum viscosity reached in the curves (excluding transient peaks), and increase in the yield stress $\sigma_y = \sigma(\eta_y)$ with higher loading rates. Normalizing η with η_y and σ by σ_y results in a collapse onto a master curve, suggesting that η_y and σ_y fully capture the differences between loading rates (Figure 2.17b). The factor increase in η_y with respect to the fastest loading rate is plotted in Figure 2.17c. At 37^{o}C the increase in η_y is almost directly proportional to the decrease in $\dot{\sigma}$, while at 30^{o}C the increase in η_y is smaller with decreasing $\dot{\sigma}$.

We also observe a slight shift of the curves towards higher stresses with higher loading rates. However, the yield stress σ_y we quantify could represent both yielding or delamination from the plates. As an alternative approach, we check if the strain γ_d and stress σ_d at the first divergence also shifts with the loading rate. Since the divergence occurs at much lower strains, we can presume that delamination has not occurred. γ_d and σ_d is manually determined for each curve and is plotted in Figure 2.17d and e. We find that both γ_d and σ_d show a weak loading-rate dependence.

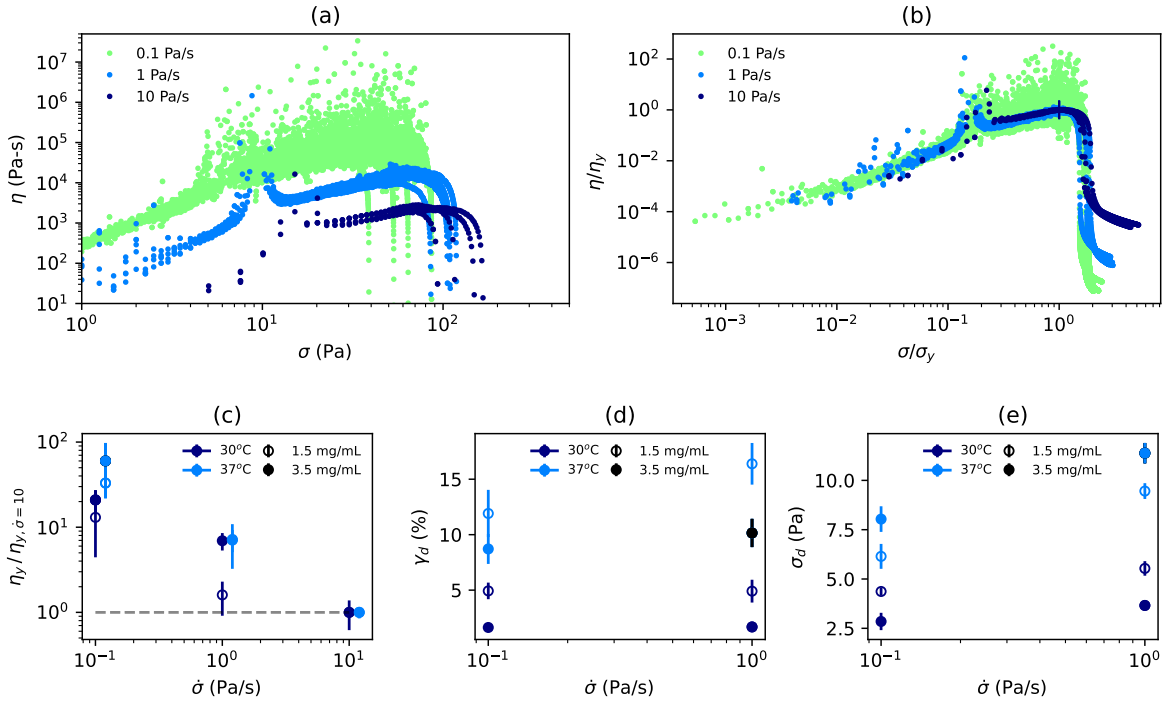

Figure 2.17: Loading-rate dependence of the apparent viscosity, and stress and strain at divergence. Stress ramps are performed at different loading rates $\dot{\sigma}$ = 0.1, 1, 10 Pa/s. (a) η as a function of σ plotted for 1.5 mg/mL atelocollagen networks polymerized at 37^{o}C. Each curve represents a separate sample. (b) Normalization of the curve with the yield viscosity η_y and the yield stress σ_y leads to a collapse onto a master curve. (c) The average factor change in η_y compared to η_y for the 10 Pa/s loading rate, as a function of $\dot{\sigma}$. The critical divergence strain γ_d is determined manually by selecting the nearest two points flanking the first divergence in viscosity and taking the mean of the strains. (d) γ_d and associated (e) $\sigma_d = \sigma(\gamma_d)$ is plotted as a function of $\dot{\sigma}$. The hollow and solid markers represent the 1.5 mg/mL and 3.5 mg/mL networks, respectively. The average is taken over N= 4 or 5 samples for each condition, and error bars represent the standard deviation.

2.4. Discussion

Prior studies have emphasized the network connectivity to govern the elastic and fracture response of collagen. However, numerous works also provide evidence of the viscoelastic, inelastic, and plastic behavior of collagen, highlighting timescale as a crucial but under explored point in the structure-mechanics relation. In this study, we characterize the bulk mechanics of collagen networks using the well-established strain ramp and frequency sweep tests. To examine their dynamic response to loading we conduct stress-controlled ramp experiments. The key findings are discussed and interpreted in the following sections.

2.4.1. Linear viscoelasticity and nonlinear elasticity

The networks polymerized at 37^{o}C are the softest and display strong viscoelastic behavior: they are the most viscous at low frequencies and become more elastic at higher frequencies (Figure 2.8a,c). The networks polymerized at 26^{o}C and 30^{o}C are stiffer and in general more elastic: they show a weaker frequency dependence of G' for the range we tested (Figure 2.8d). The viscoelastic behavior we find differs from the results of Jansen et al. [10]. There, they conducted a frequency sweep test by applying oscillatory shear with amplitude $d\gamma = 0.5\%$ over a similar frequency range of 0.05-10 Hz. They found little temperature dependence of the loss tangent G"/G' at the frequency of 0.5 Hz, and the networks polymerized at 26^{o}C, 30^{o}C, and 37^{o}C were similarly elastic with G"/G' $\approx$ 0.13. The differences are most likely due to the collagen type, as they used rat-tail collagen with intact telopeptides, which enable stronger covalent fibril-fibril interactions.

We found that the polymerization temperature dominantly controls the characteristic strains in the strain ramp test. The collagen networks polymerized at 37^{o}C show the largest onset, critical and rupture strain, and stiffening exponent β, while the networks polymerized at 26^{o}C and 30^{o}C show similar, and much lower, onset, critical and rupture strain (Figure 2.10a,b,c,d). The results from the strain ramp are in agreement with previous works. A similar temperature-dependence of the onset and critical strain was found with rat-tail collagen in the work of Jansen et al. [10], and the temperature-dependence of the rupture strain was found with collagen from different sources (rat-tail, bovine, human) in the work of Burla et al. [3]. The strong correlation between polymerization temperature and the characteristic strains of the network is attributed to changes in the average network connectivity <z>; where higher polymerization temperatures lead to networks with lower <z>, based on the fitting of the onset strain measurements to 2D simulations of disordered networks with varying <z> [3, 10]. The onset strains we found can also be fitted to the simulations of Jansen et al. [10]. Our model-estimated <z> (Figure 2.18) ranges from <z>= 3.2-3.4 for networks polymerized at 37^{o}C, <z>= 3.6-3.9 for networks polymerized at 30^{o}C and <z>= 3.7-4.0 for networks polymerized at 26^{o}C, which are all larger than the image-estimated <z> in Chapter 1 (Figure 1.12). To confirm either findings, the average connectivity should be manually checked using the 3D confocal fluorescence images of the collagen networks (Figure 1.7).

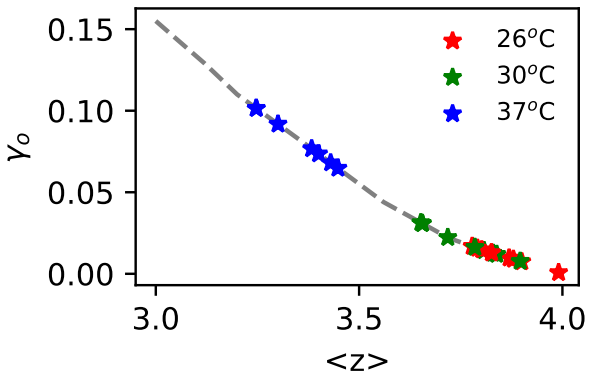

Figure 2.18: Average network connectivity <z> determined by comparing rheological measurements of the onset strain γ_o to the 2D simulations of disordered networks by Jansen et al. [10]. The dashed line represents the relation between γ_o and <z> found with simulations [10]. The markers represent the fitting of the experimentally determined γ_o from the strain ramp tests with bovine atelocollagen I networks (1.5, 2.5, and 3.5 mg/mL) polymerized at 26^{o}C, 30^{o}C, or 37^{o}C.

2.4.2. Collagen networks exhibit a transient peak in dissipation at the critical strain

The simulations by Shivers et al. have shown that subisostatic disordered networks exhibit nonaffine fluctuations under shear, which grow with a power law scaling with the distance from the critical strain. [2]. At the critical strain, the networks undergo a second order phase transition from bending to stretching dominated rigidity. By the principle of energy conservation, the divergence in nonaffine fluctuations corresponds with a divergence in the zero-shear viscosity, and the slowest relaxation time of the network [2]. Experiments have captured the continuous change of the order parameter, the differential modulus K, as a function of the strain in collagen networks [8, 9], however, measurement of diverging critical signatures have evaded prior rheological studies. We present here the first experimental observation of a divergence in apparent viscosity η at the critical strain in collagen networks. The presence of the critical divergence of η is confirmed in all atelocollagen network microstructures (1.5 and 3.5 mg/mL networks polymerized at 30^{o}C and 37^{o}C), as well as in telocollagen networks (3.5 mg/mL polymerized at 37^{o}C) (Figure 2.11, 2.16). Unlike the permanently crosslinked networks simulated by Shivers et. al. [2], we thus show that the transiently crosslinked atelocollagen networks can also display the critical signature. The critical exponent λ, which describes the power law scaling of η close to the critical strain, is determined from the stress-ramp data using a weighted mean square error approach (Appendix A.15), and the value we find ($\lambda = 1.5 \pm 0.1$) for 3.5 mg/mL atelocollagen networks for the loading rate of $\dot{\sigma} = 1$ Pa/s, shows good agreement with the theoretical value $\lambda = 1.5$ [2]. For lower collagen concentrations and polymerization temperatures, the best fit λ is difficult to reliably determine due to noise and the sparsity of data points. The reversibility of the critical divergence in η is demonstrated in the cyclic loading experiments with atelo- and telocollagen networks, where the characteristic peak consistently reappears in all loading cycles (Figure 2.15, 2.16). Telocollagen networks exhibit less plasticity compared to atelocollagen networks as seen in the overlap of the divergence in the first two loading cycles, but both networks show significant residual strain when stressed further beyond criticality in the subsequent loading cycles. The elastic nature of the phase transition

can therefore be more effectively assessed by cyclic loading of the networks to a constant, low stress magnitude of 15–20 Pa, remaining as close to the critical strain as possible.

2.4.3. Collagen networks exhibit a second transient peak in dissipation at peak stiffness

We present new evidence that collagen networks exhibit another peak in dissipation past the critical strain, coinciding with the peak in the differential modulus. To the best of our knowledge, no experiments or simulations have described the presence of a second dissipative peak in the nonlinear regime. The magnitude of the second peak varies between microstructures (Figure 2.11), suggesting it is sensitive to microscopic features of the network: the second peak is most visible in the 3.5 mg/mL atelocollagen networks, and the peak magnitude is larger in the networks polymerized at 30^{o}C compared to 37^{o}C. The second peak is suppressed in the stress ramp and cyclic loading experiments with telocollagen networks (Figure 2.16). Which prompts the question, what is the origin of the second peak?

For this high stress magnitude, we imagine that the underlying load-bearing subnetwork is maximally stretched. The stress distribution across this subnetwork can be highly heterogeneous, as evidenced in both experiments and simulations [3, 30, 68]. We hypothesize that the second peak in dissipation corresponds to a structural transition of the network for supporting a more homogeneous stress distribution. This transition is driven by nonaffine network rearrangements, facilitated by fiber rupture or plastic fiber lengthening (Figure 2.19). In the cyclic loading experiment with 3.5 mg/mL atelocollagen networks polymerized at 37^{o}C, the second peak grows between cycles 4, 5, and 6 (Figure 2.15, Appendix A.16), supporting the idea of inelastic or plastic changes in the network influencing the second peak magnitude.

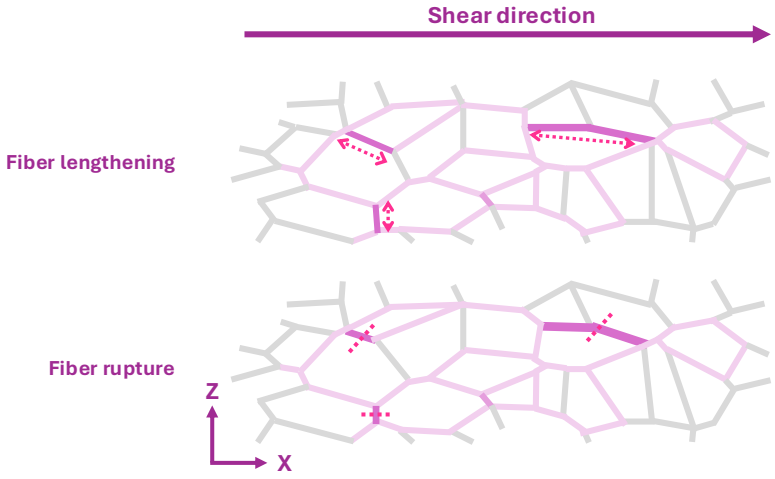

Figure 2.19: Schematic of hypothesized inelastic and plastic mechanisms affecting the load-bearing subnetwork at the second peak in dissipation. The collagen network, sheared along the positive X direction, develops a load-bearing subnetwork past the critical strain (depicted in pink). Nonaffine fluctuations places a few fibers (dark pink) under greater strain than other fibers. They can lengthen or rupture to alleviate their stress, giving rise to additional nonaffine network rearrangements at the end of the stretching-dominated nonlinear elastic regime.

The microstructural dependence of the second peak magnitude may be explained by differ-

ences in the fiber plasticity or fiber bending rigidity of the networks. Plastic fiber lengthening could provide the networks with an extra degree of freedom for stress relaxation, after they are maximally stretched. Burla et al. demonstrated that bovine atelocollagen networks exhibit significant plastic fiber lengthening, while bovine telocollagen networks show minimal plastic lengthening [3]. Plastic fiber lengthening is also identified as a mechanism by which the rupture of collagen networks can be modulated to occur at lower or higher strain. In the first chapter, we found that collagen networks formed at lower temperatures and higher concentrations have the highest degree of bundling (Chapter 1, Figure 1.7). Combining this observation with the stress ramp data suggests that weak fibril-fibril interactions within bundles may influence the peak magnitude. Our stress ramp results with 3.5 mg/mL telocollagen networks polymerized at 37^{o}C also align with the idea: the stronger fibril-fibril interactions suppresses the second peak (Figure 2.16, Appendix A.17). This is assuming that telocollagen networks are structurally similar to atelocollagen networks with the same concentration and polymerization temperature, which can be confirmed by 3D fluorescence imaging as performed in the first chapter.

Additionally, it seems possible that the magnitude of nonaffine fluctuations arising from local fiber rupture, could be influenced by the fiber bending rigidity κ. Bending rigidity is shown to control the magnitude of the zero-shear viscosity η_0 at criticality in the simulated networks of Shivers et al., according to $\eta_0(\gamma_c) - \eta_f \propto \tilde{\kappa}^{-\frac{\lambda}{\phi}}$, where $\tilde{\kappa}$ is the dimensionless bending rigidity, η_f is the fluid viscosity, λ and ϕ are critical exponents [2]. The different collagen network microstructures explored in this thesis are expected to have different $\tilde{\kappa}$. The collagen concentration c is correlated with $\tilde{\kappa}$ following the relation $\tilde{\kappa} \propto c$ derived by Sharma et al. [9]. The polymerization temperature influences the fiber thickness (Chapter 1, Figure 1.10) [10], with thicker fibers expected to have a higher κ, which leads to a higher $\tilde{\kappa}$ of the network. Telocollagen forms stiff fibers because of covalent fibril-fibril interactions. Based on this, the networks can be qualitatively ranked from lowest to highest dimensionless bending rigidity: 1.5 mg/mL 37^{o}C, 1.5 mg/mL 30^{o}C, 3.5 mg/ml 37^{o}C, 3.5 mg/ml 30^{o}C, 3.5 mg/ml 37^{o}C telocollagen. The second peak is therefore maximized at an intermediate $\tilde{\kappa}$, with a reduction in the second peak magnitude with increasing $\tilde{\kappa}$ with telocollagen, or with decreasing $\tilde{\kappa}$ with the 1.5 mg/ml concentration condition. Figure 2.19 summarizes the hypothesized origins of the second dissipative peak where fiber lengthening, or fiber rupture within the load-bearing subnetwork, or a combination of both could give rise to dissipative nonaffine fluctuations in the high-strain regime.

2.4.4. Study limitations

For most experimental conditions, data are collected from N=4 samples across two independent batches. However, for a few conditions, only N=3 or N=2 samples are collected. Given the large sample-to-sample variation of the gels, increasing the number of independent samples would improve the robustness of the data. Nevertheless, the main conclusions from the findings remain the same.

Atelo- and telocollagen networks both display a significant increase in the residual strain, and in the maximum stiffness reached during the cyclic loading experiment (Figure 2.15, 2.16). Overlooking the shift in the strain, the mechanical response of the network is not drastically

different, so the shift is most likely an artifact of the test on top of small plastic changes in the network. The apparent increase in the stiffness suggests there is inadequate resting time between cycles for the viscoelastic collagen networks. After reaching the zero-stress state, additional time should be implemented for the network to also reach zero-strain at the end of each cycle [69]. Then a collapse of $K(\gamma)$ and $\eta(\gamma)$ is expected with subsequent cycles. To rule out the possibility of transient crosslinking influencing the response, bi-directional cyclic loading tests, where the network is sheared in both positive and negative shear directions, should be performed instead of uni-directional loading tests.

Finally, the pre-strain frequency sweep and pre-strain stress relaxation experiments proposed by Shivers et al. [2] are also tested (Figure 2.6e, Appendix A.25); however, critical signatures are not observed in either test. To encompass the critical strain, pre-strain steps of 1% are taken, however it is possible that the critical signatures are missed with these step sizes. Determination of the slowest relaxation time from the pre-strain relaxation test is hindered by noise as it approaches the sensitivity limit of the rheometer for small torques (Appendix A.26,A.27). The pre-strain frequency sweep test data is less noisy, but we could not see a divergence in $\eta_0^{''}$ (Appendix A.21,A.23,A.24). However, both tests are strain-controlled, and rapid, transient spikes in stress may be hidden due to the indirect feedback loop between the applied torque and the measured deflection angle used to control strain on a stress-controlled rheometer. Similarly, no divergence in η is observed during the strain-controlled ramp (Appendix A.10). To confirm whether the critical signatures are missed due to strain-controlled experiments being performed on a stress-controlled rheometer, a strain-controlled ramp should be performed on a true strain-controlled rheometer.

2.4.5. Outlook

Future research is needed to understand the origins and role of the observed second peak in dissipation. The absence of a second peak in dissipation for the 1.5 mg/mL networks may be because the collagen response is too weak to be detected with the 20 mm diameter cone-plate head geometries, and should be tested with larger diameters. Preliminary tests with the 30 mm and 40 mm cone-plate diameters show that the measured responses are less noisy (Appendix A.20), and results hint at a small second peak bump for the 1.5 mg/mL atelocollagen networks polymerized at 37^{o}C. The influence of the microstructure on the second peak magnitude could also be further investigated with a larger range of collagen networks, prepared at lower polymerization temperatures or higher collagen concentrations (i.e. 26^{o}C, and 5.5 mg/mL). In the cyclic loading experiments with atelocollagen networks we found that the second peak in dissipation becomes more prominent in the final three cycles (Figure 2.15, Appendix A.16). The observed change in the second peak magnitude could be further investigated by performing a bi-directional cyclic loading experiment at a constant high stress magnitude of 90 Pa, for an increased number of cycles. It would be interesting to see whether collagen networks weaken with repeated high-stress loading, and if this change could be correlated with an evolution of the second peak.

Fiber elongation and fiber crosslinking are thought to occur over minutes to several hours according to the literature [59]. The preliminary pre-strain stress relaxation test suggests that the network relaxation time is at least $>$1000s (Appendix A.26, A.27). However, with the stress-controlled ramp at the slowest loading rate the maximum test duration is limited to 1500s or

shorter before the sample ruptures. To further investigate the time-dependent mechanical behavior of collagen, creep tests can be conducted at very low stress magnitudes (10–20 Pa), giving access to an extended range of experimental timescales from hours to days.

Lastly, this chapter focuses on exploring the mechanics of isotropic networks. However, in many tissues the collagen network is globally or locally anisotropic, so it is relevant to characterize their mechanics. Dedroog et al. describe a method to create anisotropic gels by applying shear stress during polymerization [70]. The method could be used to systematically generate microstructures with varying degrees of alignment.

2.5. Conclusion

The results of this chapter provide new insights into the deformation dynamics of collagen networks in the high shear strain regime, an aspect of their mechanics that has received limited attention. We present the first experimental observation of the second order critical phase transition in collagen networks by capturing their diverging viscosity at criticality, and find evidence of another peak in dissipation at the end of the nonlinear elastic regime. While further work is needed to establish the origins of the second dissipative peak, the microstructural-dependence of the peak magnitude supports the idea that other structural parameters besides <z> likely control the mechanical behavior. The findings contribute to our fundamental understanding of collagen network mechanics, provide insights into how cells may interact with their microenvironment, and, from a materials perspective, inspire new approaches for tissue engineering that leverage the strain-dependent mechanics of hierarchical, subisostatic network structures.

Conclusion

Collagen networks are fundamental structural components of the extracellular matrix and are increasingly being recognized for their role as biocompatible cellular scaffolds in *in vitro* studies, and as biomaterials for tissue engineering applications. Recent research is also looking into composite biopolymer networks for their synergistic mechanical properties. Despite the growing complexity of systems that use collagen networks, the fundamental connection between their structure and mechanics is still not fully understood. In this thesis, we focused on studying the structure and mechanical properties in the simplest model system of acellular reconstituted collagen I gels.

In the first chapter, we explored the 3D microstructure of collagen I gels combining confocal fluorescence microscopy and image analysis. By exploiting the known sensitivity of the collagen self-assembly process to the concentration and the polymerization temperature, a range of different collagen network structures were prepared and imaged. We introduced and utilized the ToFiE workflow as an automated image analysis tool to study the 3D network morphology and topology, marking the first efforts to experimentally extract the connectivity of collagen networks from images, and provided insights into the morphological changes in the network structure (edge lengths, fiber thickness, heterogeneity length scale).

In the second chapter, we used rheology to investigate a new aspect of collagen mechanics, the deformation dynamics in the nonlinear regime. We showed that collagen networks exhibit two transient peaks in viscosity under shear stress. The observed critical divergence in viscosity is the first experimental evidence for the second-order mechanical phase transition in collagen networks, as predicted by simulations. The second peak in viscosity occurs at peak stiffness, with a microstructural-dependence of the peak magnitude. We provided several hypotheses for the origins of the second dissipative peak. Our findings suggest that, in addition to the described relationship with nonlinear elasticity and fracture, the microstructure can also influence other aspects of collagen mechanics, such as their strain-dependent relaxation dynamics. The approach presented here can be more generally extended to provide insights into the dynamic mechanical behavior of other biopolymer networks.

In this thesis, the structure and mechanics of collagen networks were investigated separately. Future work can look into experiments with the in-house rheo-confocal setup, which allows imaging the networks during shear. The rheoconfocal setup consists of a rheometer head mounted on top of an inverted confocal microscope (Figure A.28). Preliminary trials have been carried out, where fluorescently labeled collagen networks were imaged during the stress-controlled ramp at the loading rate of 0.1 Pa/s (Appendix A.9.2). The temporal and spatial resolution of the timelapse images require optimization, however, improving these aspects would enable tracking nonaffine fluctuations, and provide direct visualization of the structural changes occurring within the network at the second peak in dissipation.

Bibliography

[1] Chase P. Broedersz, Xiaoming Mao, Tom C. Lubensky, and Frederick C. MacKintosh. Criticality and isostaticity in fibre networks. *Nature Physics*, 7(12):983–988, 12 2011. ISSN 1745-2473. doi: 10.1038/nphys2127.

[2] Jordan L. Shivers, Abhinav Sharma, and Fred C. MacKintosh. Strain-Controlled Critical Slowing Down in the Rheology of Disordered Networks. *Physical Review Letters*, 131 (17):178201, 10 2023. ISSN 0031-9007. doi: 10.1103/PhysRevLett.131.178201.

[3] Federica Burla, Simone Dussi, Cristina Martinez-Torres, Justin Tauber, Jasper van der Gucht, and Gijsje H. Koenderink. Connectivity and plasticity determine collagen network fracture. *Proceedings of the National Academy of Sciences*, 117(15):8326–8334, 4 2020. ISSN 0027-8424. doi: 10.1073/pnas.1920062117.

[4] Hajer Ennomani, Gaëlle Letort, Christophe Guérin, Jean-Louis Martiel, Wenxiang Cao, François Nédélec, Enrique M De La Cruz, Manuel Théry, and Laurent Blanchoin. Architecture and Connectivity Govern Actin Network Contractility. *Current biology : CB*, 26 (5):616–26, 3 2016. ISSN 1879-0445. doi: 10.1016/j.cub.2015.12.069.

[5] Jing Xia, Li-Heng Cai, Huayin Wu, Frederick C. MacKintosh, and David A. Weitz. Anomalous mechanics of Zn^{2}□-modified fibrin networks. *Proceedings of the National Academy of Sciences*, 118(10), 3 2021. ISSN 0027-8424. doi: 10.1073/pnas.2020541118.

[6] Yong How Tan, Krista M. Habing, Jessica L. Riesterer, Erin S. Stempinski, Steven H. Lewis, Carmem S. Pfeifer, Sanjay V. Malhotra, and Karina H. Nakayama. Engineered nanofibrillar collagen with tunable biophysical properties for myogenic, endothelial, and osteogenic cell guidance. *Acta Biomaterialia*, 186:95–107, 9 2024. ISSN 17427061. doi: 10.1016/j.actbio.2024.08.002.

[7] G. Y. Liu, R. Agarwal, K. R Ko, M. Ruthven, H. T. Sarhan, and J. P. Frampton. Templated Assembly of Collagen Fibers Directs Cell Growth in 2D and 3D. *Scientific Reports*, 7 (1):9628, 8 2017. ISSN 2045-2322. doi: 10.1038/s41598-017-10182-8.

[8] Albert James Licup, Stefan Münster, Abhinav Sharma, Michael Sheinman, Louise M. Jawerth, Ben Fabry, David A. Weitz, and Fred C. MacKintosh. Stress controls the mechanics of collagen networks. *Proceedings of the National Academy of Sciences*, 112 (31):9573–9578, 8 2015. ISSN 0027-8424. doi: 10.1073/pnas.1504258112.

[9] A. Sharma, A. J. Licup, K. A. Jansen, R. Rens, M. Sheinman, G. H. Koenderink, and F. C. MacKintosh. Strain-controlled criticality governs the nonlinear mechanics of fibre networks. *Nature Physics*, 12(6):584–587, 6 2016. ISSN 1745-2473. doi: 10.1038/nphys3628.

[10] Karin A. Jansen, Albert J. Licup, Abhinav Sharma, Robbie Rens, Fred C. MacKintosh, and Gijsje H. Koenderink. The Role of Network Architecture in Collagen Mechanics. *Biophysical Journal*, 114(11):2665–2678, 6 2018. ISSN 00063495. doi: 10.1016/j.bpj.2018.04.043.

[11] Spencer P. Lake, Jess G. Snedeker, Vincent M. Wang, Hani Awad, Hazel R. C. Screen, and Stavros Thomopoulos. Guidelines for ex vivo mechanical testing of tendon. *Journal of Orthopaedic Research*, 41(10):2105–2113, 10 2023. ISSN 0736-0266. doi: 10.1002/jor.25647.

[12] Alan E. Woessner, Jake D. Jones, Nathan J. Witt, Edward A. Sander, and Kyle P. Quinn. Three-Dimensional Quantification of Collagen Microstructure During Tensile Mechanical Loading of Skin. *Frontiers in Bioengineering and Biotechnology*, 9, 3 2021. ISSN 2296-4185. doi: 10.3389/fbioe.2021.642866.

[13] W. Lee, A. Ostadi Moghaddam, S. Shen, H. Phillips, B. L. McFarlin, A. J. Wagoner Johnson, and K. C. Toussaint. An optomechanogram for assessment of the structural and mechanical properties of tissues. *Scientific Reports*, 11(1):324, 1 2021. ISSN 2045-2322. doi: 10.1038/s41598-020-79602-6.

[14] Alexander Hayn, Tony Fischer, and Claudia Tanja Mierke. Inhomogeneities in 3D Collagen Matrices Impact Matrix Mechanics and Cancer Cell Migration. *Frontiers in Cell and Developmental Biology*, 8, 11 2020. ISSN 2296-634X. doi: 10.3389/fcell.2020.593879.

[15] JiEung Kim, Sangmin Lee, Chang-Yeon Gu, Taek-Soo Kim, Hyunjoon Kong, and Dongchan Jang. Mechanical Characterization of Collagen Hydrogels by Quasistatic Uniaxial Tensile Experiments. *Advanced Engineering Materials*, 25(21), 11 2023. ISSN 1438-1656. doi: 10.1002/adem.202301136.

[16] Shaunak Kanade, Milie Desai, Neel Bhatavadekar, and Nagaraj Balasubramanian. Quantitative analysis of fibrillar collagen organization in the immediate proximity of embedded fibroblasts in 3D collagen hydrogels. *Journal of Biosciences*, 49(3):65, 6 2024. ISSN 0973-7138. doi: 10.1007/s12038-024-00449-4.

[17] Maximilian Witte, Michael Rübhausen, Sören Jaspers, Horst Wenck, and Frank Fischer. A method to analyze the influence of mechanical strain on dermal collagen morphologies. *Scientific Reports*, 11(1):7565, 4 2021. ISSN 2045-2322. doi: 10.1038/s41598-021-86907-7.

[18] Stefan B. Lindström, David A. Vader, Artem Kulachenko, and David A. Weitz. Biopolymer network geometries: Characterization, regeneration, and elastic properties. *Physical Review E*, 82(5):051905, 11 2010. ISSN 1539-3755. doi: 10.1103/PhysRevE.82.051905.

[19] Vanesa Olivares, Mar Cóndor, Cristina Del Amo, Jesús Asín, Carlos Borau, and José Manuel García-Aznar. Image-based Characterization of 3D Collagen Networks and the Effect of Embedded Cells. *Microscopy and Microanalysis*, 25(4):971–981, 8 2019. ISSN 1431-9276. doi: 10.1017/S1431927619014570.

[20] Riccardo Alberini, Andrea Spagnoli, Mohammad Javad Sadeghinia, Bjørn Skallerud, Michele Terzano, and Gerhard A. Holzapfel. Fourier transform-based method for quantifying the three-dimensional orientation distribution of fibrous units. *Scientific Reports*, 14(1):1999, 1 2024. ISSN 2045-2322. doi: 10.1038/s41598-024-51550-5.

[21] Eline E. van Haaften, Tamar B. Wissing, Marcel C.M. Rutten, Jurgen A. Bulsink, Kujtim Gashi, Mathieu A.J. van Kelle, Anthal I.P.M. Smits, Carlijn V.C. Bouten, and Nicholas A. Kurniawan. Decoupling the Effect of Shear Stress and Stretch on Tissue Growth and Remodeling in a Vascular Graft. *Tissue Engineering Part C: Methods*, 24(7):418–429, 7 2018. ISSN 1937-3384. doi: 10.1089/ten.tec.2018.0104.

[22] Ting Xu, Dimitrios Vavylonis, Feng-Ching Tsai, Gijsje H. Koenderink, Wei Nie, Eddy Yusuf, I-Ju Lee, Jian-Qiu Wu, and Xiaolei Huang. SOAX: A software for quantification of 3D biopolymer networks. *Scientific Reports*, 5(1):9081, 3 2015. ISSN 2045-2322. doi: 10.1038/srep09081.

[23] Anna Jaeschke, Hagen Eckert, and Laura J Bray. Qiber3D—an open-source software package for the quantitative analysis of networks from 3D image stacks. *GigaScience*, 11, 2 2022. ISSN 2047-217X. doi: 10.1093/gigascience/giab091.

[24] Jeremy S. Bredfeldt, Yuming Liu, Carolyn A. Pehlke, Matthew W. Conklin, Joseph M. Szulczewski, David R. Inman, Patricia J. Keely, Robert D. Nowak, Thomas R. Mackie, and Kevin W. Eliceiri. Computational segmentation of collagen fibers from second-harmonic generation images of breast cancer. *Journal of Biomedical Optics*, 19(1): 016007, 1 2014. ISSN 1083-3668. doi: 10.1117/1.JBO.19.1.016007.

[25] ANDREW M. STEIN, DAVID A. VADER, LOUISE M. JAWERTH, DAVID A. WEITZ, and LEONARD M. SANDER. An algorithm for extracting the network geometry of three-dimensional collagen gels. *Journal of Microscopy*, 232(3):463–475, 12 2008. ISSN 0022-2720. doi: 10.1111/j.1365-2818.2008.02141.x.

[26] Ninna Struck Rossen, Anders Kyrsting, Amato J. Giaccia, Janine Terra Erler, and Lene Broeng Oddershede. Fiber finding algorithm using stepwise tracing to identify biopolymer fibers in noisy 3D images. *Biophysical Journal*, 120(18):3860–3868, 9 2021. ISSN 00063495. doi: 10.1016/j.bpj.2021.08.017.

[27] Stefan B. Lindström, Artem Kulachenko, Louise M. Jawerth, and David A. Vader. Finite-strain, finite-size mechanics of rigidly cross-linked biopolymer networks. *Soft Matter*, 9 (30):7302, 2013. ISSN 1744-683X. doi: 10.1039/c3sm50451d.

[28] T. Sousbie. The persistent cosmic web and its filamentary structure - I. Theory and implementation. *Monthly Notices of the Royal Astronomical Society*, 414(1):350–383, 6 2011. ISSN 00358711. doi: 10.1111/j.1365-2966.2011.18394.x.

[29] Tatiana Merle, Sophie Theis, Alain Kamgoué, Emmanuel Martin, Florian Sarron, Guillaume Gay, Emmanuel Farge, and Magali Suzanne. DISSECT is a tool to segment and explore cell and tissue mechanics in highly deformed 3D epithelia. *Developmental Cell*, 58(20):2181–2193, 10 2023. ISSN 15345807. doi: 10.1016/j.devcel.2023.07.017.

[30] Richard C. Arevalo, Pramukta Kumar, Jeffrey S. Urbach, and Daniel L. Blair. Stress Heterogeneities in Sheared Type-I Collagen Networks Revealed by Boundary Stress Microscopy. *PLOS ONE*, 10(3):e0118021, 3 2015. ISSN 1932-6203. doi: 10.1371/journal.pone.0118021.

[31] Stéphanie Motte and Laura J. Kaufman. Strain stiffening in collagen I networks. *Biopolymers*, 99(1):35–46, 1 2013. ISSN 0006-3525. doi: 10.1002/bip.22133.

[32] Blayne A. Roeder, Klod Kokini, and Sherry L. Voytik-Harbin. Fibril Microstructure Affects Strain Transmission Within Collagen Extracellular Matrices. *Journal of Biomechanical Engineering*, 131(3), 3 2009. ISSN 0148-0731. doi: 10.1115/1.3005331.

[33] Blayne A. Roeder, Klod Kokini, Jennifer E. Sturgis, J. Paul Robinson, and Sherry L. Voytik-Harbin. Tensile Mechanical Properties of Three-Dimensional Type I Collagen Extracellular Matrices With Varied Microstructure. *Journal of Biomechanical Engineering*, 124(2):214–222, 4 2002. ISSN 0148-0731. doi: 10.1115/1.1449904.

[34] Louise M Jawerth, Stefan Münster, David A Vader, Ben Fabry, and David A Weitz. A blind spot in confocal reflection microscopy: the dependence of fiber brightness on fiber orientation in imaging biopolymer networks. *Biophysical journal*, 98(3):1–3, 2 2010. ISSN 1542-0086. doi: 10.1016/j.bpj.2009.09.065.

[35] David Remy, Anne-Sophie Macé, Philippe Chavrier, and Pedro Monteiro. Invadopodia Methods: Detection of Invadopodia Formation and Activity in Cancer Cells Using Reconstituted 2D and 3D Collagen-Based Matrices. pages 225–246. 2023. doi: 10.1007/978-1-0716-2887-4{_}14.

[36] Andrew D. Doyle. Fluorescent Labeling of Rat-tail Collagen for 3D Fluorescence Imaging. *BIO-PROTOCOL*, 8(13), 2018. ISSN 2331-8325. doi: 10.21769/BioProtoc.2919.

[37] Stéfan van der Walt, Johannes L. Schönberger, Juan Nunez-Iglesias, François Boulogne, Joshua D. Warner, Neil Yager, Emmanuelle Gouillart, and Tony Yu. scikit-image: image processing in Python. *PeerJ*, 2:e453, 6 2014. ISSN 2167-8359. doi: 10.7717/peerj.453.

[38] Nadav Yayon, Amir Dudai, Nora Vrieler, Oren Amsalem, Michael London, and Hermona Soreq. Intensify3D: Normalizing signal intensity in large heterogenic image stacks. *Scientific Reports*, 8(1):4311, 3 2018. ISSN 2045-2322. doi: 10.1038/s41598-018-22489-1.

[39] Sylvain Prigent. SDeconv Python Framework.

[40] Sami Koho. MIPLIB: Microscope image processing library. 2020.

[41] Leland McInnes. How UMAP Works, 2018.

[42] Dingkang Wang, Lucas Magee, Bing-Xing Huo, Samik Banerjee, Xu Li, Jaikishan Jayakumar, Meng Kuan Lin, Keerthi Ram, Suyi Wang, Yusu Wang, and Partha P. Mitra. Detection and skeletonization of single neurons and tracer injections using topological methods, 3 2020.

[43] Delft High Performance Computing Centre (DHPC). DelftBlue Supercomputer (Phase 2). https://www.tudelft.nl/dhpc/ark:/44463/DelftBluePhase2, 2024.

[44] Ali Ahmad, Guillaume Vanel, Sorina Camarasu-Pop, Axel Bonnet, Carole Frindel, and David Rousseau. MicroVIP: Microscopy image simulation on the Virtual Imaging Platform. *SoftwareX*, 16:100854, 12 2021. ISSN 23527110. doi: 10.1016/j.softx.2021.100854.

[45] Alexia Ferrand, Kai D. Schleicher, Nikolaus Ehrenfeuchter, Wolf Heusermann, and Oliver Biehlmaier. Using the NoiSee workflow to measure signal-to-noise ratios of confocal microscopes. *Scientific Reports*, 9(1):1165, 2 2019. ISSN 2045-2322. doi: 10.1038/s41598-018-37781-3.

[46] Alan Cooper. Thermodynamic studies of the assembly in vitro of native collagen fibrils. *Biochemical Journal*, 118(3):355–365, 7 1970. ISSN 0306-3283. doi: 10.1042/bj1180355.

[47] Christopher Allen Rucksack Jones, Long Liang, Daniel Lin, Yang Jiao, and Bo Sun. The spatial-temporal characteristics of type I collagen-based extracellular matrix. *Soft Matter*, 10(44):8855–8863, 2014. ISSN 1744-683X. doi: 10.1039/C4SM01772B.

[48] Svetlana Morozova and Murugappan Muthukumar. Electrostatic effects in collagen fibril formation. *The Journal of Chemical Physics*, 149(16), 10 2018. ISSN 0021-9606. doi: 10.1063/1.5036526.

[49] Christopher A. R. Jones, Matthew Cibula, Jingchen Feng, Emma A. Krnacik, David H. McIntyre, Herbert Levine, and Bo Sun. Micromechanics of cellularized biopolymer networks. *Proceedings of the National Academy of Sciences*, 112(37), 9 2015. ISSN 0027-8424. doi: 10.1073/pnas.1509663112.

[50] Fan Yang, Debashish Das, Kathiresan Karunakaran, Guy M. Genin, Stavros Thomopoulos, and Ioannis Chasiotis. Nonlinear time-dependent mechanical behavior of mammalian collagen fibrils. *Acta Biomaterialia*, 163:63–77, 6 2023. ISSN 17427061. doi: 10.1016/j.actbio.2022.03.005.

[51] José Ruiz-Franco and Jasper van Der Gucht. Force Transmission in Disordered Fibre Networks. *Frontiers in Cell and Developmental Biology*, 10, 6 2022. ISSN 2296-634X. doi: 10.3389/fcell.2022.931776.

[52] Stefan Münster, Louise M. Jawerth, Beverly A. Leslie, Jeffrey I. Weitz, Ben Fabry, and David A. Weitz. Strain history dependence of the nonlinear stress response of fibrin and collagen networks. *Proceedings of the National Academy of Sciences*, 110(30):12197–12202, 7 2013. ISSN 0027-8424. doi: 10.1073/pnas.1222787110.

[53] Jordan L. Shivers, Sadjad Arzash, Abhinav Sharma, and Fred C. MacKintosh. Scaling Theory for Mechanical Critical Behavior in Fiber Networks. *Physical Review Letters*, 122(18):188003, 5 2019. ISSN 0031-9007. doi: 10.1103/PhysRevLett.122.188003.

[54] Luca Salvatore, Nunzia Gallo, Maria Lucia Natali, Alberta Terzi, Alessandro Sannino, and Marta Madaghiele. Mimicking the Hierarchical Organization of Natural Collagen: Toward the Development of Ideal Scaffolding Material for Tissue Regeneration. *Frontiers in Bioengineering and Biotechnology*, 9, 4 2021. ISSN 2296-4185. doi: 10.3389/fbioe.2021.644595.

[55] Cornelis Storm, Jennifer J. Pastore, F. C. MacKintosh, T. C. Lubensky, and Paul A. Janmey. Nonlinear elasticity in biological gels. *Nature*, 435(7039):191–194, 5 2005. ISSN 0028-0836. doi: 10.1038/nature03521.

[56] Paul A. Janmey, Margaret E. McCormick, Sebastian Rammensee, Jennifer L. Leight, Penelope C. Georges, and Fred C. MacKintosh. Negative normal stress in semiflexible biopolymer gels. *Nature Materials*, 6(1):48–51, 1 2007. ISSN 1476-1122. doi: 10.1038/nmat1810.

[57] Qi Wen, Anindita Basu, Jessamine P Winer, Arjun Yodh, and Paul A Janmey. Local and global deformations in a strain-stiffening fibrin gel. *New Journal of Physics*, 9(11): 428–428, 11 2007. ISSN 1367-2630. doi: 10.1088/1367-2630/9/11/428.

[58] Andrew M. Stein, David A. Vader, David A. Weitz, and Leonard M. Sander. The micromechanics of three-dimensional collagen-I gels. *Complexity*, 16(4):22–28, 3 2011. ISSN 1076-2787. doi: 10.1002/cplx.20332.

[59] Ehsan Ban, J. Matthew Franklin, Sungmin Nam, Lucas R. Smith, Hailong Wang, Rebecca G. Wells, Ovijit Chaudhuri, Jan T. Liphardt, and Vivek B. Shenoy. Mechanisms of Plastic Deformation in Collagen Networks Induced by Cellular Forces. *Biophysical Journal*, 114(2):450–461, 1 2018. ISSN 00063495. doi: 10.1016/j.bpj.2017.11.3739.

[60] David Vader, Alexandre Kabla, David Weitz, and Lakshminarayana Mahadevan. Strain-Induced Alignment in Collagen Gels. *PLoS ONE*, 4(6):e5902, 6 2009. ISSN 1932-6203. doi: 10.1371/journal.pone.0005902.

[61] Jordan L. Shivers, Sadjad Arzash, and F. C. MacKintosh. Nonlinear Poisson Effect Governed by a Mechanical Critical Transition. *Physical Review Letters*, 124(3):038002, 1 2020. ISSN 0031-9007. doi: 10.1103/PhysRevLett.124.038002.

[62] René B. Svensson, Tue Hassenkam, Philip Hansen, and S. Peter Magnusson. Viscoelastic behavior of discrete human collagen fibrils. *Journal of the Mechanical Behavior of Biomedical Materials*, 3(1):112–115, 1 2010. ISSN 17516161. doi: 10.1016/j.jmbbm.2009.01.005.

[63] Frederik Fleissner, Mischa Bonn, and Sapun H. Parekh. Microscale spatial heterogeneity of protein structural transitions in fibrin matrices. *Science Advances*, 2(7), 7 2016. ISSN 2375-2548. doi: 10.1126/sciadv.1501778.

[64] H. Hatami-Marbini and R. C. Picu. Effect of fiber orientation on the non-affine deformation of random fiber networks. *Acta Mechanica*, 205(1-4):77–84, 6 2009. ISSN 0001-5970. doi: 10.1007/s00707-009-0170-7.

[65] Jihan Kim, Jingchen Feng, Christopher A. R. Jones, Xiaoming Mao, Leonard M. Sander, Herbert Levine, and Bo Sun. Stress-induced plasticity of dynamic collagen networks. *Nature Communications*, 8(1):842, 10 2017. ISSN 2041-1723. doi: 10.1038/s41467-017-01011-7.

[66] Qi Wen, Anindita Basu, Paul A. Janmey, and Arjun G. Yodh. Non-affine deformations in polymer hydrogels. *Soft Matter*, 8(31):8039, 2012. ISSN 1744-683X. doi: 10.1039/c2sm25364j.

[67] Advanced BioMatrix - Collagen. URL https://advancedbiomatrix.com/collagen/.

[68] Estelle Berthier, Haiqian Yang, Ming Guo, Pierre Ronceray, and Chase P. Broedersz. Nonlinear mechanosensation in fiber networks. *Physical Review Research*, 6(1):013327, 3 2024. ISSN 2643-1564. doi: 10.1103/PhysRevResearch.6.013327.

[69] Monica E. Susilo, Jeffrey A. Paten, Edward A. Sander, Thao D. Nguyen, and Jeffrey W. Ruberti. Collagen network strengthening following cyclic tensile loading. *Interface Focus*, 6(1):20150088, 2 2016. ISSN 2042-8898. doi: 10.1098/rsfs.2015.0088.

[70] Lens M. Dedroog, Olivier Deschaume, Christian J. Garcia Abrego, Erin Koos, Yovan de Coene, Anja Vananroye, Wim Thielemans, Carmen Bartic, and Minne P. Lettinga. Stress-controlled shear flow alignment of collagen type I hydrogel systems. *Acta Biomaterialia*, 150:128–137, 9 2022. ISSN 17427061. doi: 10.1016/j.actbio.2022.07.008.

A

Appendix

A.1. Protocol: NHS ester labeling for fluorescent collagen

Risa Togo and Irène Nagle

The methods of Remy et al. and Doyle et al. are adapted and optimized in this protocol for labeling bovine atelocollagen type I with DyLight™ 550 NHS Ester [35, 36].

Graphical Abstract

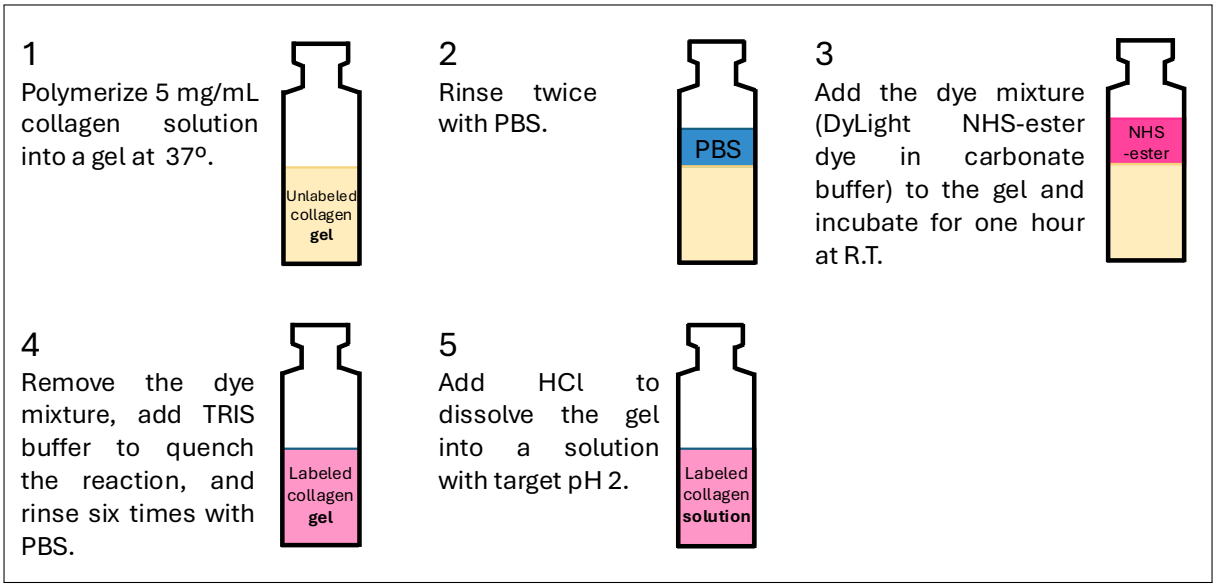

	Stock conc.	Final conc.	Volume
Bovine atelocollagen I	9.99 mg/mL	5 mg/mL	1010 µL
PBS	10x	1x	200 µL
MilliQ			690 µL
NaOH	0.1M	5%	100 µL
			Total: 2000 µL

Table A.1: Scheme for the preparation of 2 mL of 5 mg/mL bovine atelocollagen solution.

Method

Bovine atelocollagen type I (Biomatrix Fibricol, Advanced BioMatrix) is neutralized to pH 7.4 in one part 10x phosphate-buffered saline (PBS, pH 7.4, Gibco), 0.1M NaOH, and MilliQ water, to a final volume of 2 mL and a collagen concentration of 5 mg/mL. A representative scheme is shown in table A.1. The solution is mixed in a centrifuge tube on ice by pipetting up and down without introducing bubbles, and then transferred to a glass vial. The pH is checked to be close to 7.4 using pH strips. The solution is incubated in a water bath at 37^oC for 90 minutes or until gelation is complete and a smooth opaque gel had formed in the vial. Then the gel is rinsed twice with 5 mL of 1x PBS for ten minutes each. A two-molar excess of DyLight 550 NHS ester dye solution (ThermoScientific™, 10 mg/mL in anhydrous DMSO) is pre-mixed in a buffer consisting of 3 mL of MilliQ and 1 mL of 1M carbonate buffer (1M $NaHCO_3$ adjusted to pH 8.3 with 1M Na_2CO_3) and added to the gel at room temperature. The volume of dye solution (16 µL) is calculated based on the mass of collagen in the gel, molecular weight of the dye, 2-molar excess of dye and the concentration of the dye stock solution (Doyle et. al. 2018). The MW of DyLight™ 550 NHS Ester is 1040 g/mol, and the MW of collagen I is theoretically in the range of 130-140 kDa, but variations may exist due to biological reasons such as species, post translational modifications, and experimental factors.

$$\frac{\text{Collagen in mg}}{\text{Collagen MW}} \times (\text{Dye molar excess}) \times (\text{Dye MW}) \times (\text{Dye conc. } (\mu\text{L/mg})) = \text{Dye volume in } \mu\text{L} \tag{A.1}$$

$$\frac{10 \text{ mg}}{130000 \text{ MW}} \times 2 \times 1040 \times 100 = 16 \ \mu\text{L} \tag{A.2}$$

The dye solution is removed from the gel after one hour and replaced with 10 mL of 50 mM Tris buffer (pH 7.5) to quench the dye reaction for ten minutes. Unbound dye molecules are removed through six sequential washing steps with 5 mL of 1x PBS at room temperature, each time for 30 minutes. In the last wash, all the PBS is discarded. Then 1 mL of cold 20 mM HCl and additional drops of 1M HCl in increments of 10 µL is added to bring the pH down to 2 and dissolve the gel. To help the dissolution, the gel is gently agitated for 1-2 hours at 4°C. The final labeled collagen solution is stored at 4°C in the dark.

Additional notes and troubleshooting

The size of the glass vial to hold the gel should not be too large such that a thin and weak gel is formed, or too small, as the limited surface area will hinder the diffusion of the dye. The p1000 pipette is used to slowly add and aspirate solutions during rinsing and incubating steps to disturb the gel as little as possible. The carbonate buffer is made on the day of carrying out the protocol. To obtain a higher concentration of labeled collagen solution, the concentration of the initial gel can be increased or a smaller volume of HCl can be used at the end for dissolution. The labeled solution should look homogeneous, transparent, and brightly coloured. Depending on the age of the NHS ester dye, the labeling reaction can be less efficient. We determine that a two-molar excess works well for labeling with DyLight™ 550 NHS Ester or DyLight™ 633 NHS Ester. However, we found that DyLight™ 633 photobleaches easily and therefore is not suitable for acquiring z-stacks. The two-molar excess is too high for DyLight™ 488 NHS Ester and Alexa Fluor™ 488 NHS Ester dyes, producing overlabeled collagen that form aggregates and curly fibers. For DyLight™ 488 and Alexa Fluor™ 488, a one-molar excess or lower is found to be optimal although the result does not give a very bright fluorescence signal.

The labeled gels are prepared with a 1:2 mass fraction of labeled collagen monomers to obtain a good signal-to-noise ratio in images with negligible influence on the resulting structure and mechanics. A 1:1 mass fraction gives brighter fluorescence signal but seems to influence the structure under specific conditions from our qualitative observations. The salt present in the labeled collagen solution is accounted for by reducing the PBS added such that the resultant gel still consists of one part 10x PBS. As too high of a salt concentration can interfere with the kinetics of self-assembly, when we did not make these salt adjustments, network polymerization is largely inhibited at lower temperatures and higher collagen concentrations.

Schemes for making labelled collagen gels

1.5 mg/mL collagen, pH 7.4, (1:2 mass fraction of labeled to unlabeled)

	Stock conc.	**Final conc.**	**Volume**
Unlabelled collagen	9.9 mg/mL	1 mg/mL	10.10 µL
Labelled collagen	3.33 mg/mL	0.5 mg/mL	15.02 µL
PBS	10x		$\left(\frac{S_{\text{adj}}}{10}\right) \times (V_{\text{total}} - V_{\text{labeled}})$ 9.0 µL
MQ (milliQ water)			63.88 µL
NaOH	0.1 M	2%	2 µL
			Total: 100 µL

Salt adjustment

$(\frac{2}{30} \times 0.1502) + (\frac{S_{\text{adj}}}{10} \times 0.8498) = \frac{1}{10}$ (10x PBS)

$S_{\text{adj}} = 1.059$

2.5 mg/mL collagen, pH 7.4, (1:2 mass fraction of labeled to unlabeled)

	Stock conc.	**Final conc.**	**Volume**
Unlabelled collagen	9.9 mg/mL	1.67 mg/mL	16.87 µL
Labelled collagen	3.33 mg/mL	0.833 mg/mL	25.02 µL
PBS	10x		$\left(\frac{S_{\text{adj}}}{10}\right) \times (V_{\text{total}} - V_{\text{labeled}})$ 8.32 µL
MQ (milliQ water)			45.79 µL
NaOH	0.1 M	4%	4 µL
			Total: 100 µL

Salt adjustment
$\frac{2}{30} \times 0.2502 + \frac{S_{\text{adj}}}{10} \times 0.7498 = \frac{1}{10}$ (10x PBS)
$S_{\text{adj}} = 1.11$

3.5 mg/mL collagen, pH 7.4, (1:2 mass fraction of labeled to unlabeled)

	Stock conc.	**Final conc.**	**Volume**
Unlabelled collagen	9.9 mg/mL	2.33 mg/mL	23.57 µL
Labelled collagen	3.33 mg/mL	1.17 mg/mL	35.04 µL
PBS	10x		$\left(\frac{S_{\text{adj}}}{10}\right) \times (V_{\text{total}} - V_{\text{labeled}})$ 7.67 µL
MQ (milliQ water)			28.72 µL
NaOH	0.1 M	5%	5 µL
			Total: 100 µL

Salt adjustment
$\frac{2}{30} \times 0.3504 + \frac{S_{\text{adj}}}{10} \times 0.6496 = \frac{1}{10}$ (10x PBS)
$S_{\text{adj}} = 1.18$

A.2. Labeled collagen gel structure and mechanics

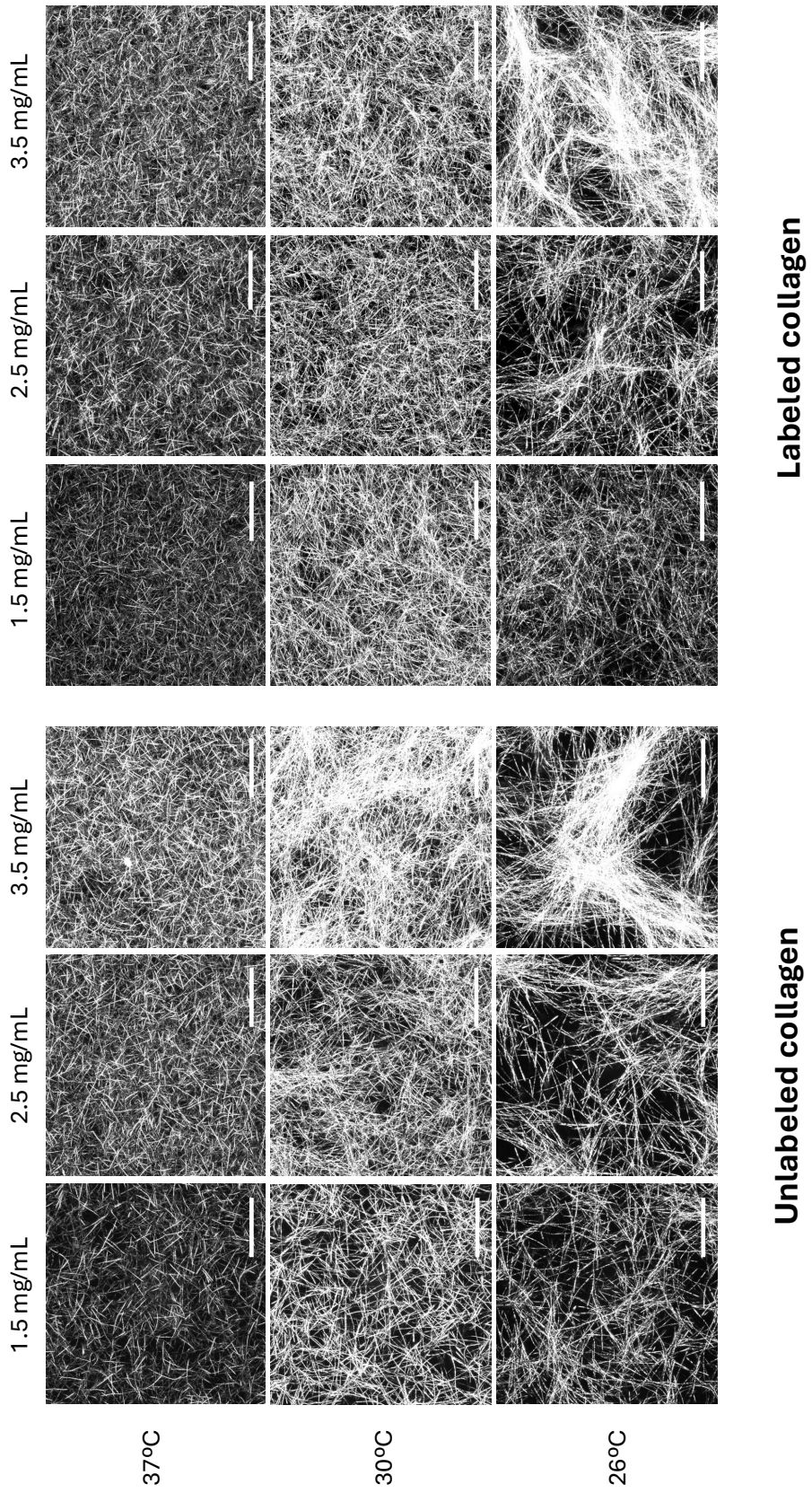

Figure A.1: Labeled collagen networks show little differences in microstructure compared to the unlabeled collagen networks. Maximum intensity projection of confocal reflectance images of the collagen gels prepared with (top) or without labeling (bottom) over a depth of 9.9 µm, with a 1:2 mass fraction of Dylight 550 labeled to unlabeled collagen monomers for the labeled networks. The scale bar represents 30 µm, and the total image size is 112 µm.

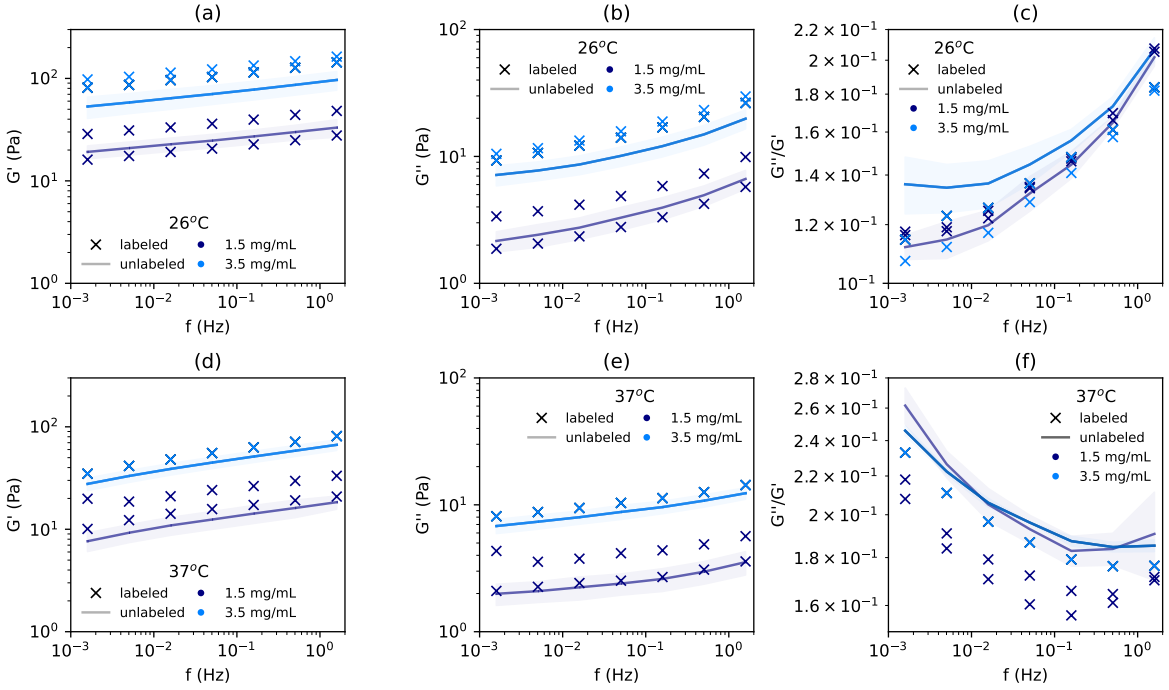

Figure A.2: Frequency sweep with 1:2 labeled or unlabeled collagen gel. The storage G' (a,d), loss modulus G'' (b,e), and loss tangent G''/G' (c,f), plotted as a function of the oscillation frequency for 1.5 mg/mL and 3.5 mg/mL networks polymerized at 26^{o}C (a-c), and at 37^{o}C (d-f). Each curve represents a separate sample for the labeled collagen. The average curve over N=4 samples is shown for the unlabeled collagen with the error bars representing the standard deviation. For the 3.5 mg/mL unlabeled network polymerized at 37^{o}C, N=2 samples is shown.

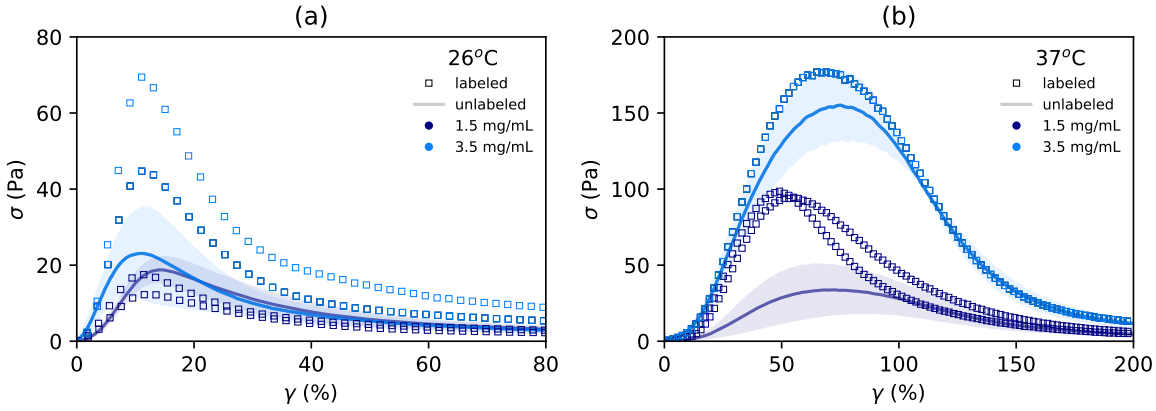

Figure A.3: Strain ramp with 1:2 labeled or unlabeled collagen gel. The stress-strain response during a strain-controlled ramp at $\dot{\gamma}$= 0.1%/s for 1.5 mg/mL and 3.5 mg/mL collagen networks polymerized at 26^{o}C (a), and at 37^{o}C (b). Each curve represents a separate sample for the labeled collagen. The average curve over N=4 samples is shown for the unlabeled collagen with the error bars representing the standard deviation. For the 3.5 mg/mL unlabeled collagen at 37^{o}C, the average results of N=2 samples is shown.

A.3. Synthetic networks

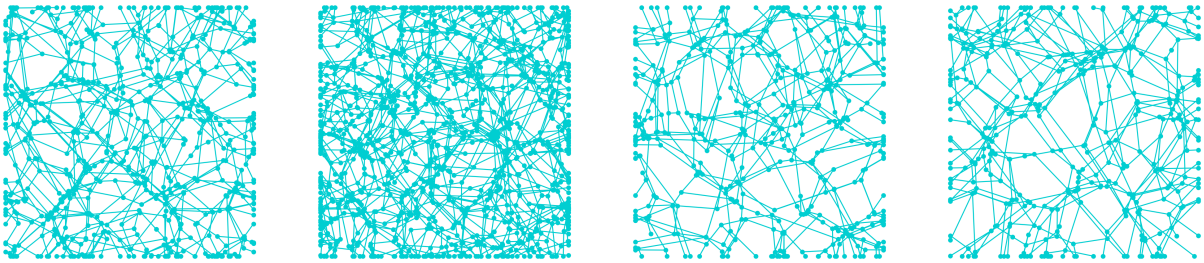

Figure A.4: Synthetic networks. A representative network is shown (left to right) for each of the average connectivity <z> = 3.12, 3.20, 3.36, 3.56.

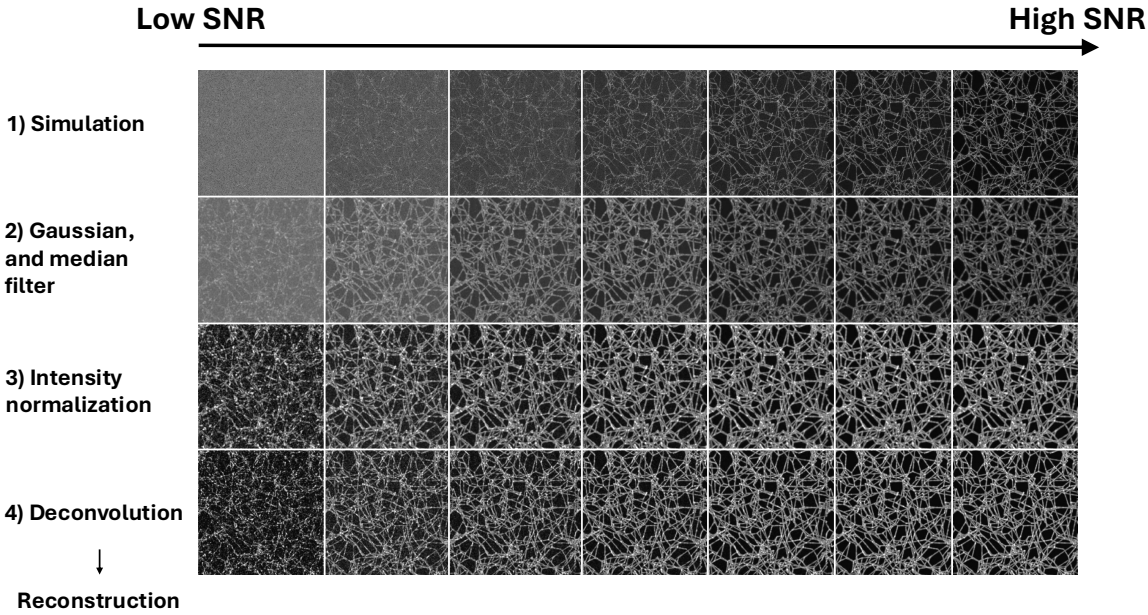

Figure A.5: Overview of the pre-processing step for the simulated confocal images.

Step	Process	Parameters
Pre-processing	Smoothing	Gaussian: sigma=2.5 truncate=0.2
	Intensity normalization	Lower: (manually determined), Upper: 0.9999-th percentile
	Deconvolution	2 iterations of the Richardson-Lucy algorithm (Gaussian PSF)
	Intensity normalization	Lower: 0, Upper: 0.9999-th percentile
DisPerSe	Tracing	cut: 40, smooth: 100, assemble: 30, trimBelow: 15
Skeleton refinement	Custom functions	$\theta_{thr} = \frac{\Pi}{3}$, l_{thr} = 0.4 µm

Table A.2: Parameter values for the ToFiE workflow for the reconstruction of synthetic networks. The corresponding image voxel size is 0.1x0.1x0.1 µm.

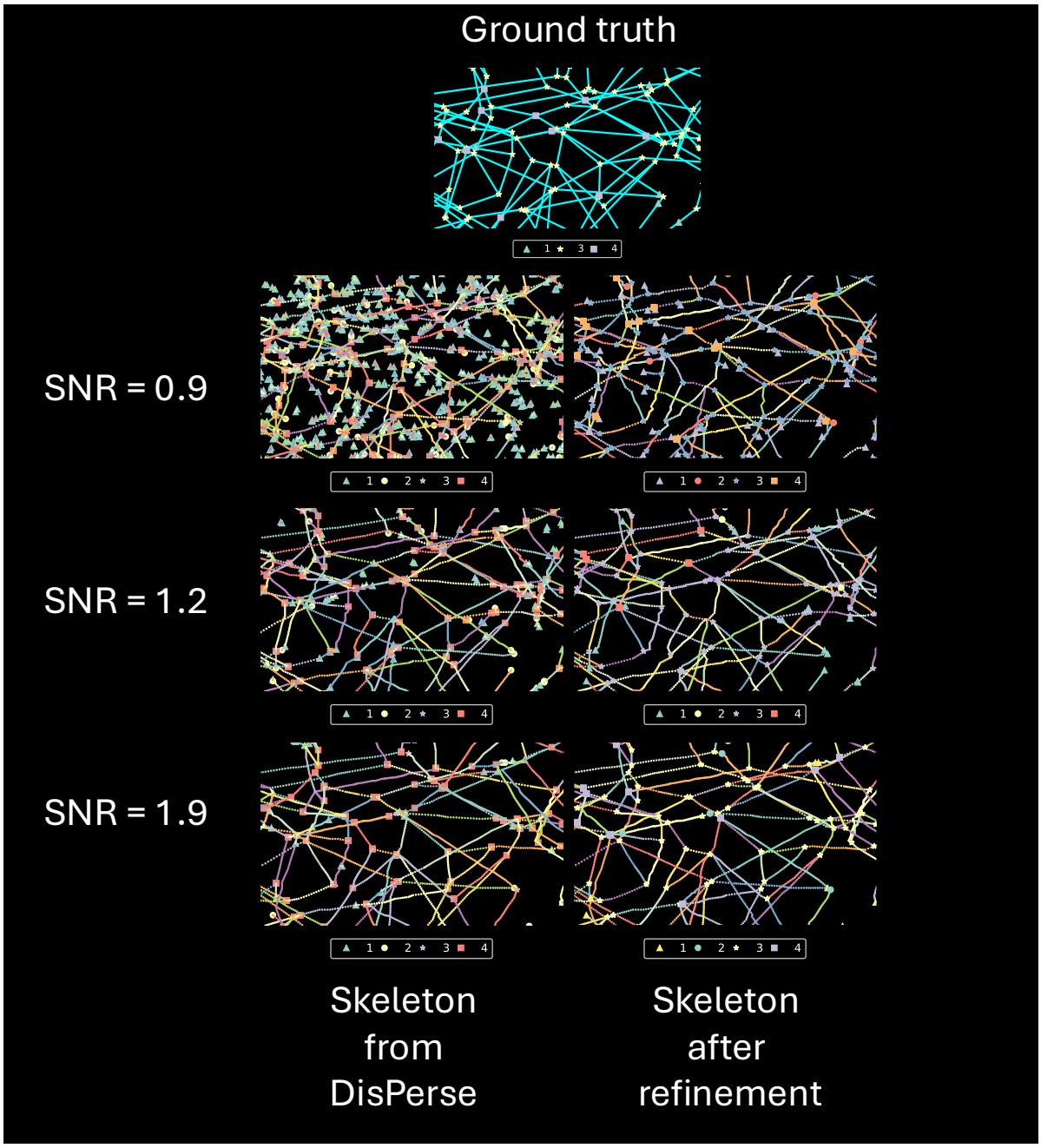

Figure A.6: Network reconstruction before and after the skeleton refinement step at different signal to noise ratios. The ground truth synthetic network is shown above (cyan). Below it are the skeleton reconstructions from DisPerSe (left) and the skeleton reconstructions after refinement with the parameters $\theta_{thr} = \frac{\Pi}{3}$ and $l_{thr} = 0.4$ µm (right). The marker shapes represent the identified connectivities of junctions in the skeleton.

A.4. Collagen image library

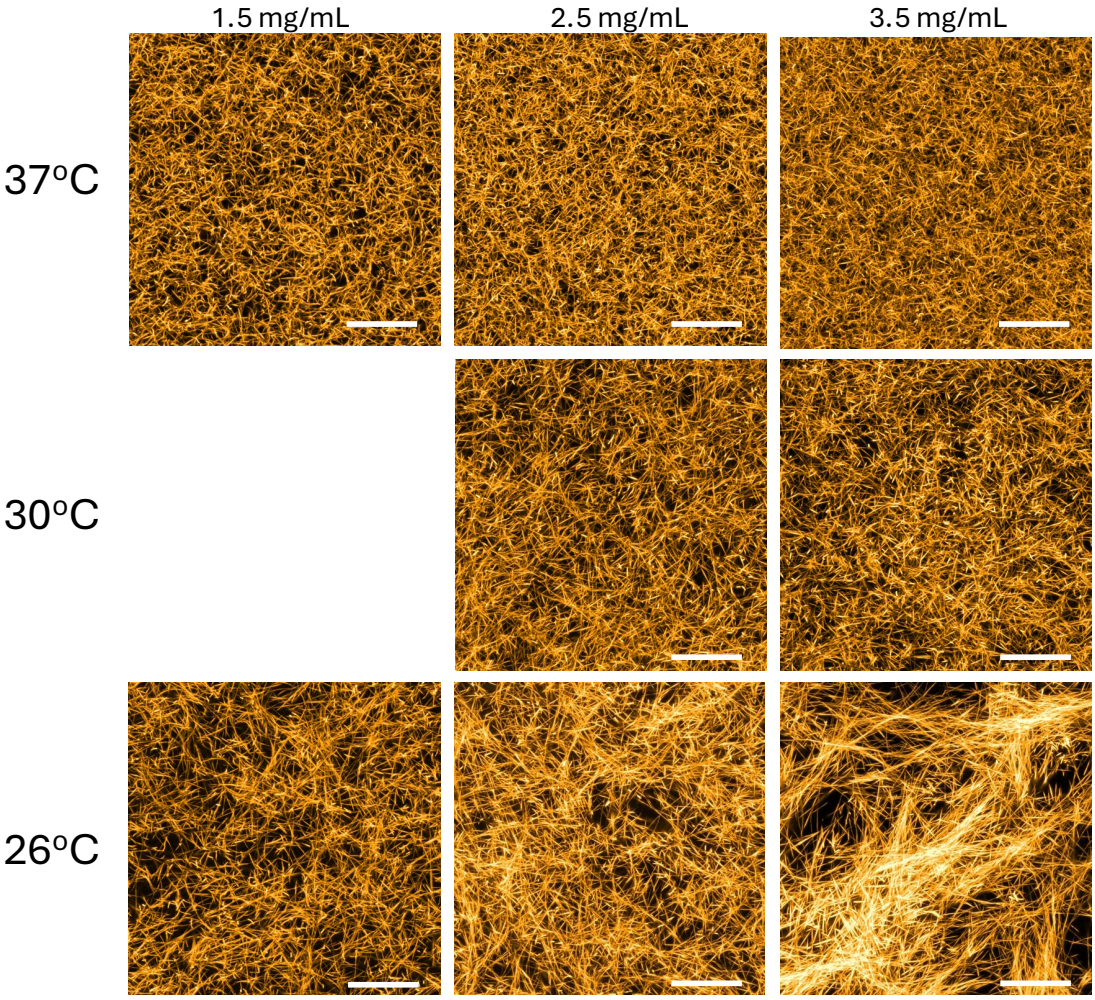

Figure A.7: 3D image library of collagen microstructures (N=2). The maximum intensity projection of processed confocal fluorescence images of the collagen gels (concentration: 1.5, 2.5, 3.5 mg/mL, polymerization temperature: 26°C, 30°C, 37°C) prepared with 1:2 mass fraction of Dylight 550 labelled and unlabeled collagen monomers are shown over a depth of 4.95 µm. Scale bar represents 25 µm, and the image size is 112 µm with an isotropic pixel size of 0.1 µm.

A.4.1. Collagen network reconstruction

Step	Process	Parameters
Pre-processing	Smoothing	Gaussian: sigma=2.5 truncate=0.1
	Intensity normalization	Lower: 0, Upper: 0.999995-th percentile
	Deconvolution	4 iterations of the Richardson-Lucy algorithm (Gaussian PSF)
	Intensity normalization	Lower: 0, Upper: 0.9999-th percentile
DisPerSe	Tracing	cut: 20, smooth: 100, assemble: 30, trimBelow: 10
Skeleton refinement	Custom functions	$\theta_{thr} = \frac{\Pi}{3}$, l_{thr} = 0.4 µm

Table A.3: Parameter values for the ToFiE workflow for the reconstruction of collagen networks. The corresponding image voxel size is 0.11x0.11x0.11 µm.

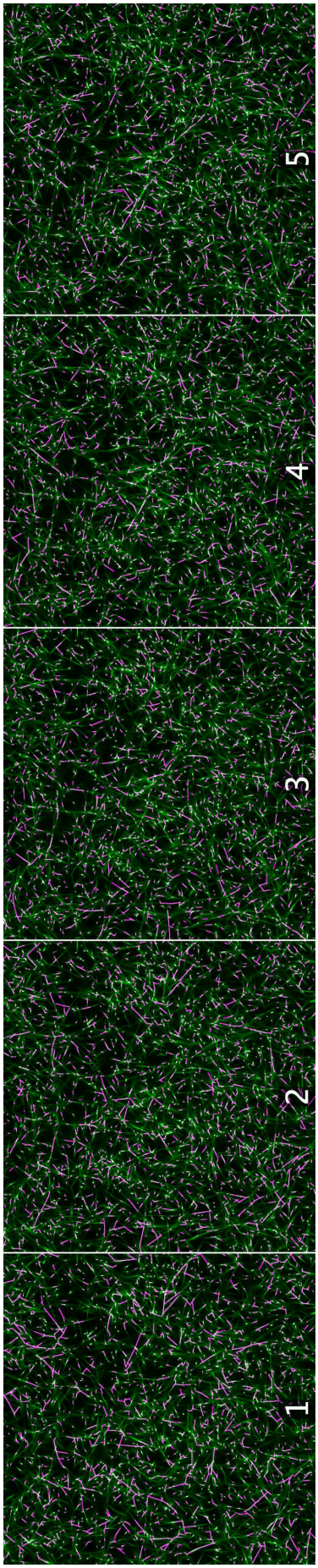

Figure A.8: Montage of the fiber tracing video. The imaged collagen network is shown in green, and the reconstructed network with the cut parameter value of 20 is overlaid on top in magenta. Each frame represents the maximum intensity projection across a depth of 0.55 µm. The image size is 112 µm.

A.5. Strain-controlled ramp

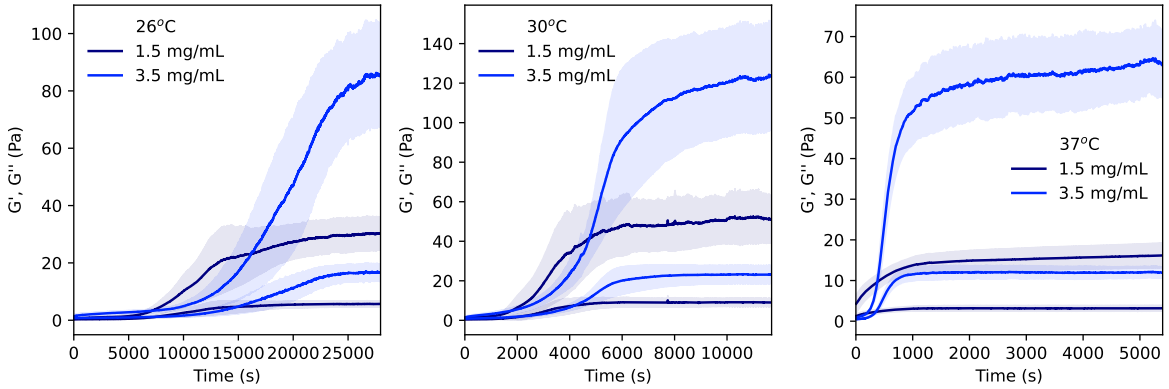

Figure A.9: Polymerization time sweep of atelocollagen I networks at different temperatures. The storage G' and loss G" modulus is plotted as a function of time. N=4 samples shown, except for the 3.5 mg/mL network polymerized at 30^{o}C (N=3 samples) and 3.5 mg/mL network polymerized at 37^{o}C (N=2 samples). The error bar represents the standard deviation.

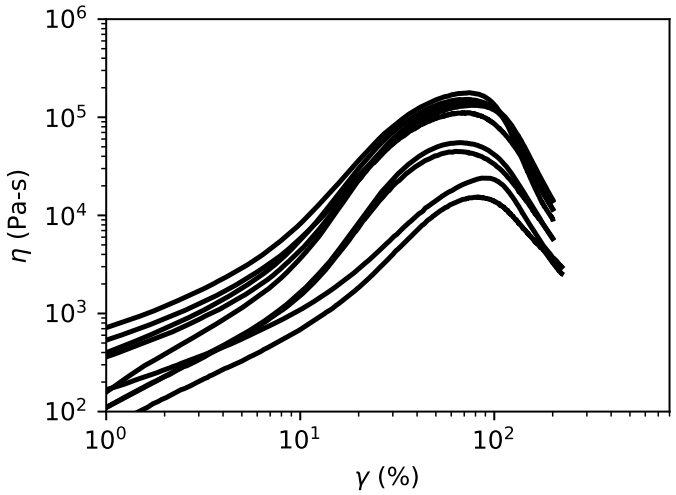

Figure A.10: Apparent viscosity during the strain-controlled ramp. Atelocollagen networks with different collagen concentrations (1.5, 2.5, 3.5 mg/mL) polymerized at 37^{o}C are subject to a strain-controlled ramp at $\dot{\gamma} = 0.1\%/s$. The apparent viscosity defined as $\eta = \frac{\sigma}{\dot{\gamma}}$ is plotted as a function of γ. Each curve represents a different sample.

A.6. Stress-controlled ramp

A.6.1. Linear stress ramp

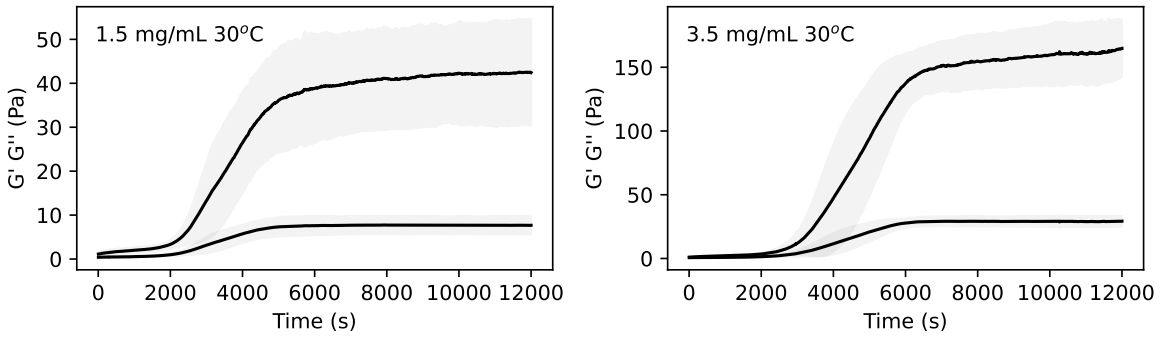

Figure A.11: Polymerization time sweep of atelocollagen I networks at 30°C. The average storage G' and loss G" modulus is plotted as a function of time. N=12 samples are shown for each collagen concentration. The error bar represents the standard deviation.

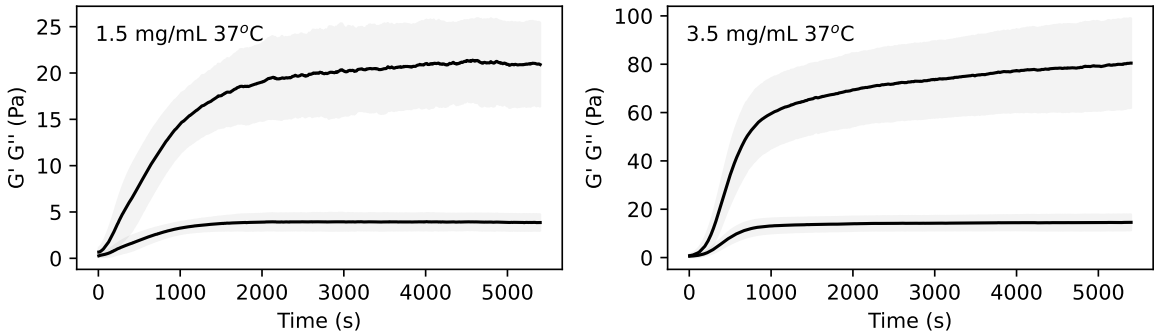

Figure A.12: Polymerization time sweep of atelocollagen I networks at 37°C. The average storage G' and loss G" modulus is plotted as a function of time. N=12 samples are shown for each collagen concentration. The error bar represents the standard deviation.

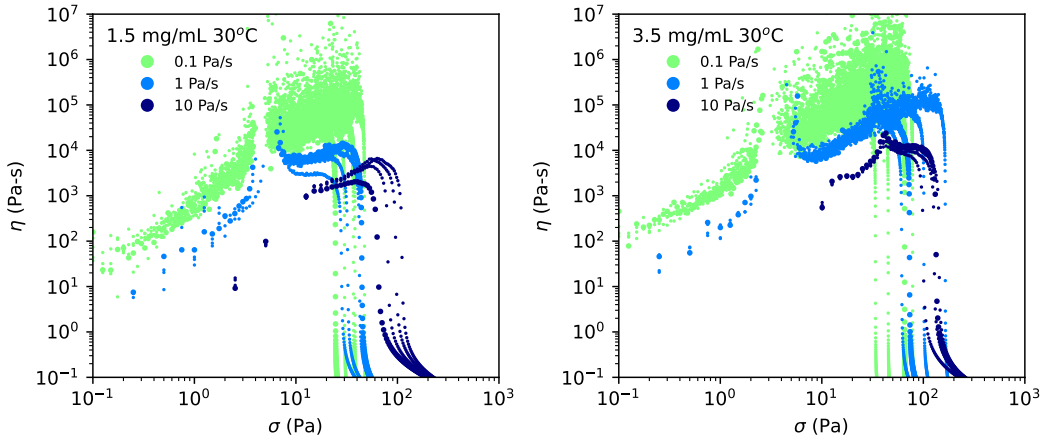

Figure A.13: Stress ramp with atelocollagen networks polymerized at 30°C. Each curve represents a different sample. N=4 samples for each loading rate.

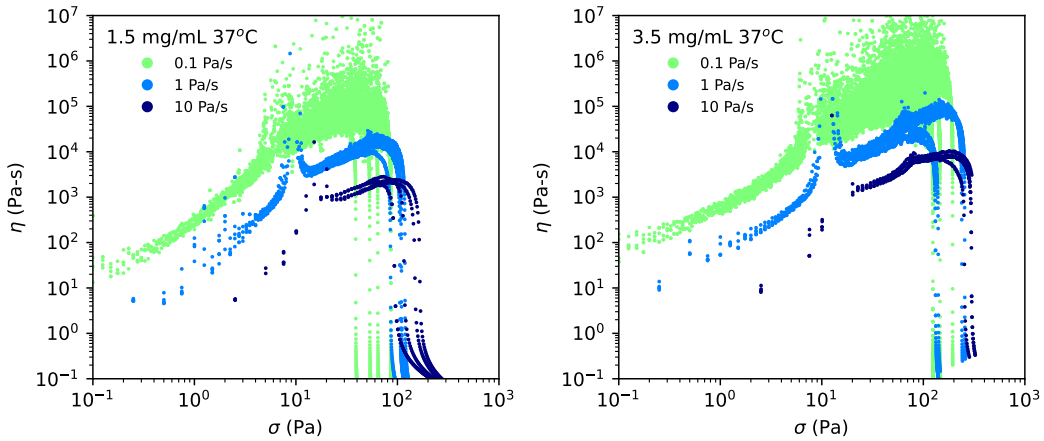

Figure A.14: Stress ramp with atelocollagen networks polymerized at 37°C. Each curve represents a different sample. N=4 samples for each loading rate.

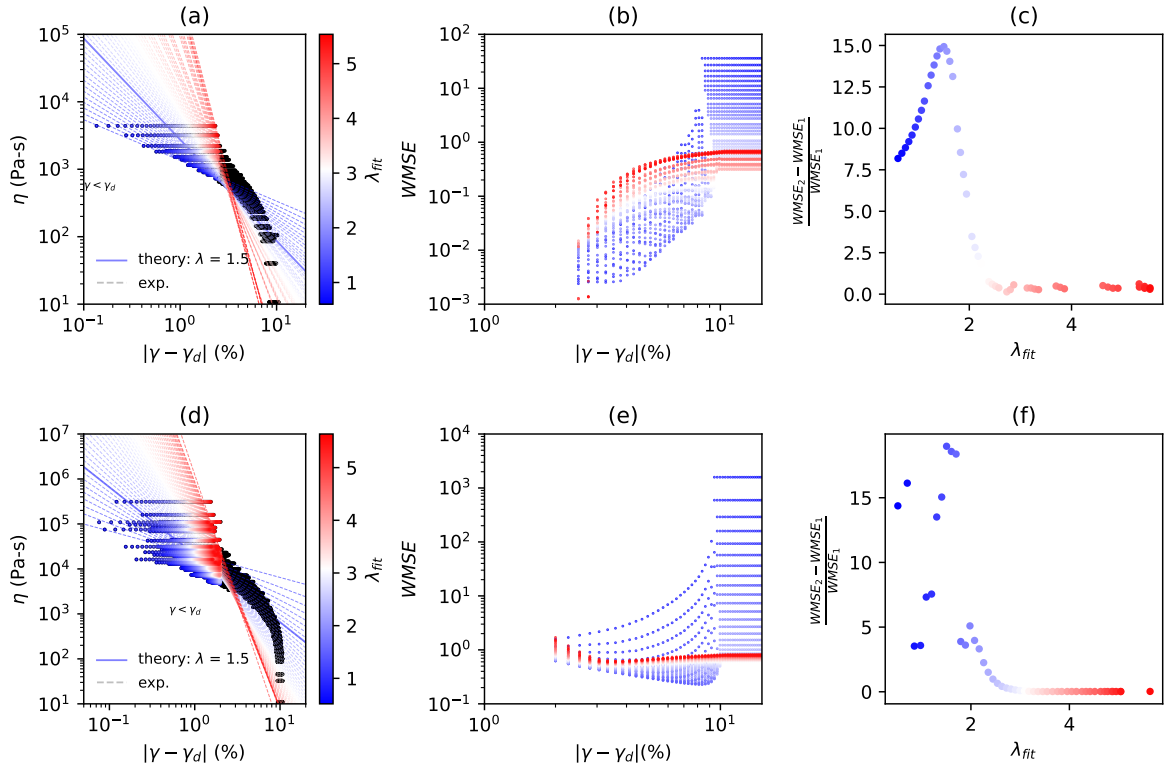

Figure A.15: Experimental determination of the critical exponent λ at the first peak in dissipation. A representative sample of the 3.5 mg/mL atelocollagen networks polymerized at 37^{o}C with the ramp at $\dot{\sigma} = 1$ Pa/s is shown in (a-c), or $\dot{\sigma} = 0.1$ Pa/s in (d-f). (a,d) The black markers represent the datapoints where $\gamma < \gamma_d$, shown for all possible values of the divergence strain γ_d between the manually determined nearest two datapoints flanking the divergence in viscosity. The datapoints where $|\gamma - \gamma_d| \leq 2.5$ (a), or $|\gamma - \gamma_d| \leq 2$ (d), are fitted to determine the critical exponent λ in the relation $\eta \propto |\gamma - \gamma_d|^{-\lambda}$, resulting in a different λ for each value of γ_d, shown with the dashed line. The theoretical fit with $\lambda = 1.5$ from the simulations of Shivers et. al. is plotted as the solid line [2]. (b,d) The weighted mean square error WMSE, defined as WMSE(λ) $= \frac{1}{k}\sum_{i=1}^{k} \frac{1}{\eta_i^2}(\eta_i - \eta_{fit,i}(\lambda))^2$, is calculated between the datapoints and the fitted line for each λ, and is plotted here as a function of the distance $|\gamma - \gamma_d|$ from the divergence. (c,f) For specific values of λ, the WMSE jumps up beyond a certain distance $|\gamma - \gamma_d|$, indicating the end of the divergence region. The WMSE right before and after this transition is defined as WMSE_1 and WMSE_2, respectively. The relative size of the jump $\frac{WMSE_2 - WMSE_1}{WMSE_1}$ is plotted for each λ. The best fit λ is chosen as the value which maximizes the size of the jump, indicating a good fitting for the divergence, and a poor fitting beyond the divergence.

A.6.2. Cyclic stress ramp

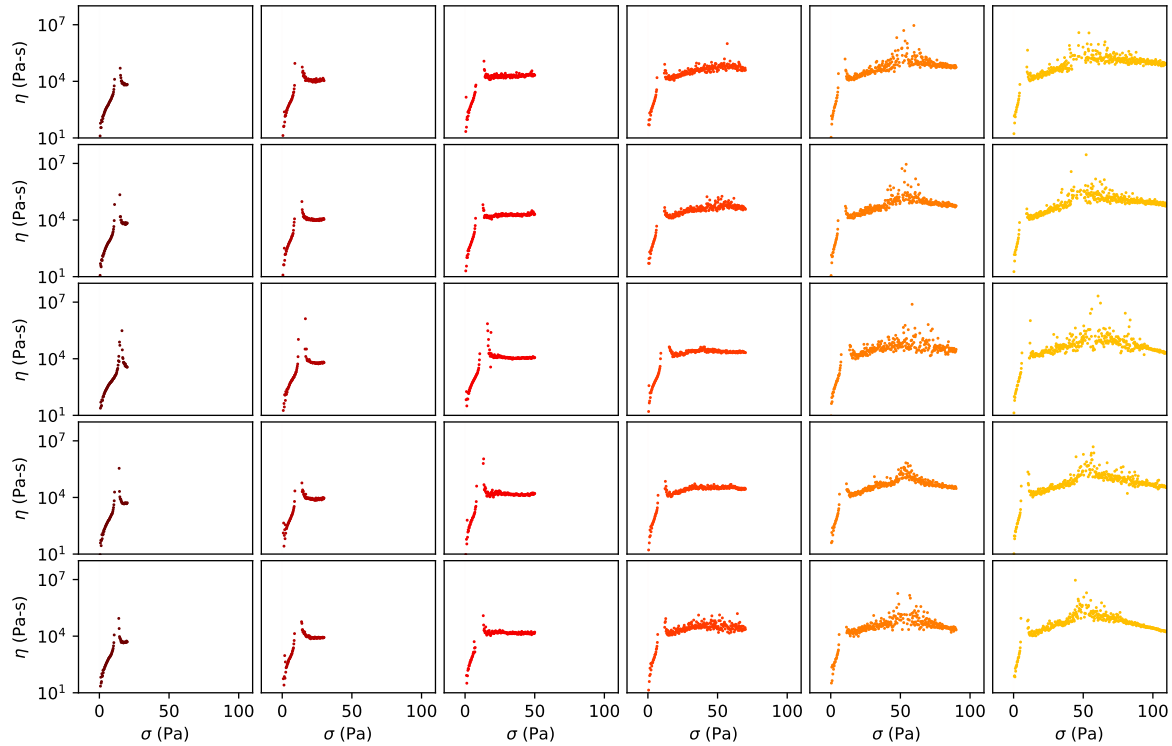

Figure A.16: Cyclic stress ramp with 3.5 mg/mL atelocollagen networks polymerized at 37°C. The cyclic loading protocol in Figure 2.6d is carried out. Each row represents a different sample. Each column represents the $\eta(\sigma)$ response as a function of σ for the loading part of one cycle, with increasing final stress magnitude of 20, 30, 50, 70, 90, 110 Pa (from left to right).

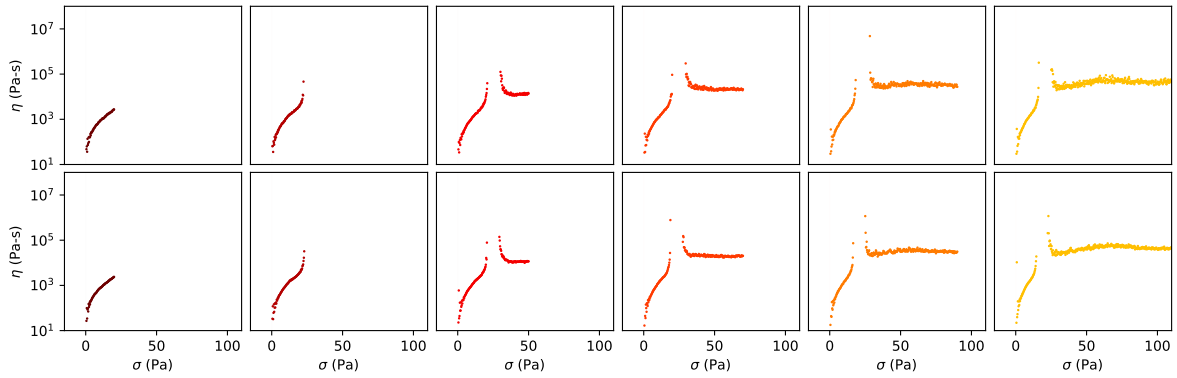

Figure A.17: Cyclic stress ramp with 3.5 mg/mL telocollagen networks polymerized at 37°C. The cyclic loading protocol in Figure 2.6d is carried out. Each row represents a different sample. Each column represents the $\eta(\sigma)$ response as a function of σ for the loading part of one cycle, with increasing final stress magnitude of 20, 30, 50, 70, 90, 110 Pa (from left to right).

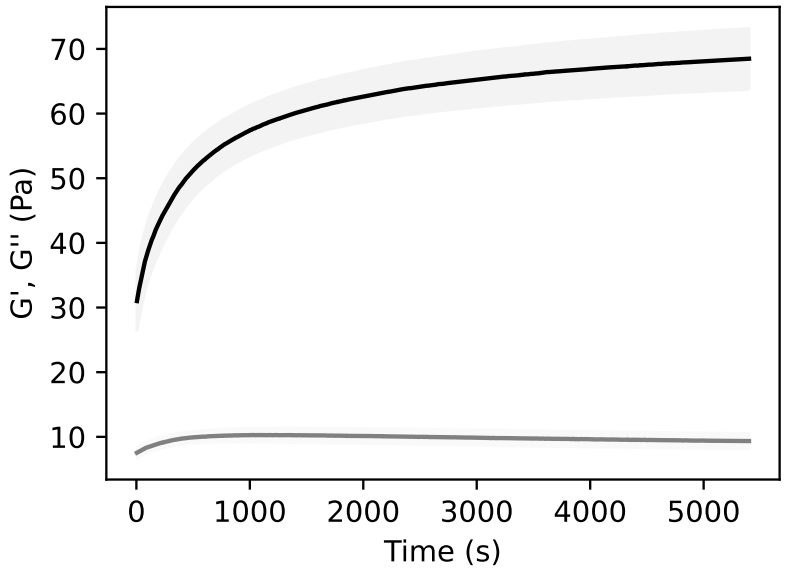

Figure A.18: Polymerization time sweep of 3.5 mg/mL telocollagen networks at 37°C. The average storage G' and loss G'' modulus is plotted as a function of time. N=4 samples are shown. The error bar represents the standard deviation.

A.6.3. Linear stress ramp with larger cone head diameters (30 mm and 40 mm)

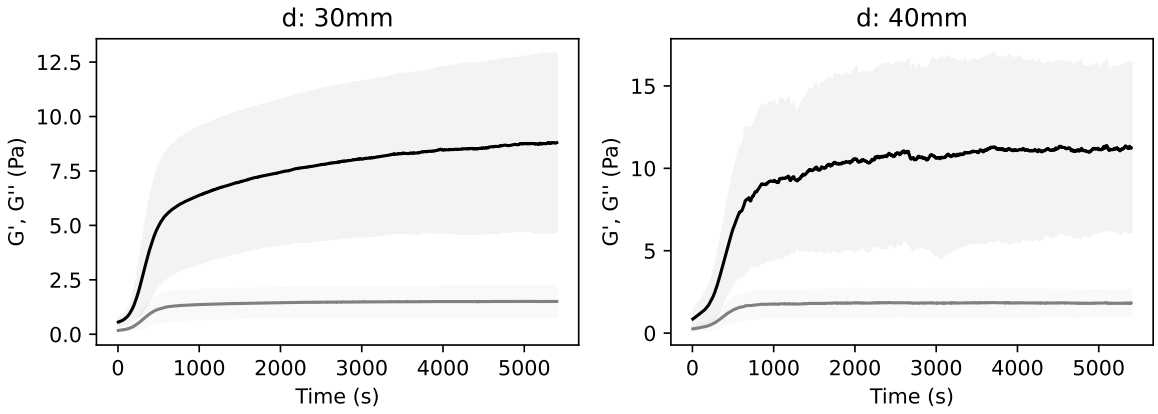

Figure A.19: Polymerization of 1.5 mg/mL atelocollagen networks at 37^{o}C with the cone head diameter d = 30 mm (N=7) or d = 40 mm (N=5). The average storage G' and loss G" modulus is plotted as a function of time. The samples all turned out to be on the softer side compared to what is expected for this condition (G' ≈15-25 Pa) and the sample to sample variations are large, so the stress ramp results in Figure A.20 should be carefully considered.

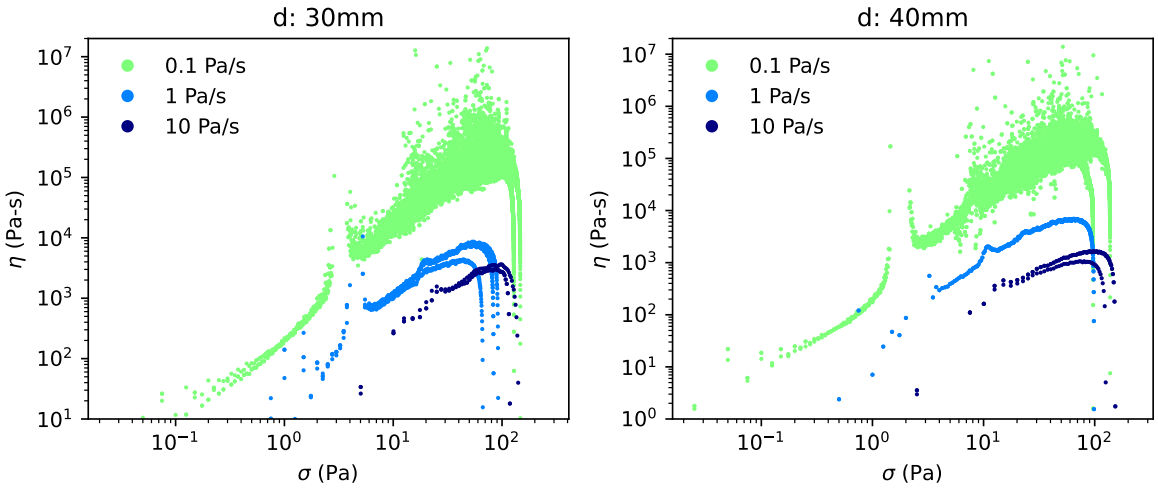

Figure A.20: Stress ramp with 1.5 mg/mL atelocollagen networks polymerized at 37^{o}C, with the cone head diameter d = 30 mm or d = 40 mm. The apparent viscosity η is shown as a function of σ. Each curve represents a single sample.

A.7. Pre-strain frequency sweep test

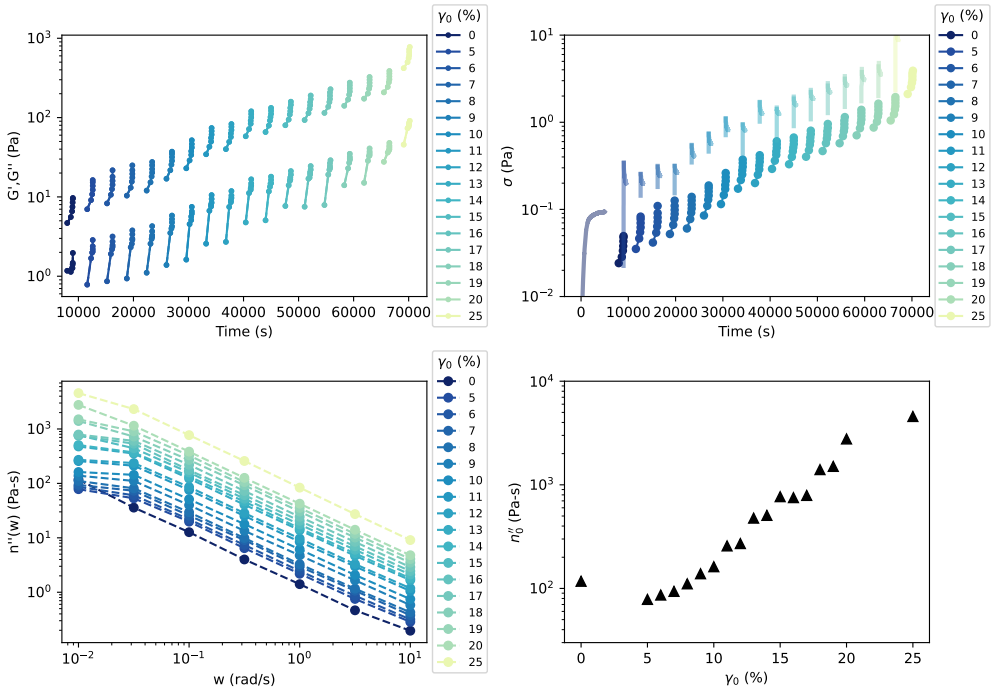

Figure A.21: Pre-strain frequency sweep test with a 2 mg/mL atelocollagen network polymerized at 37^{o}C. The pre-strain frequency sweep test in Figure 2.6e is carried out. One representative sample is depicted. Colors represent the pre-strain value γ_0. The storage G', loss G'' modulus and stress σ is plotted as a function of time. The zero-shear viscosity $\eta_0''(\gamma_0)$ is determined as the limit of dynamic viscosity $\eta''(\omega, \gamma_0) = \frac{G''(\omega,\gamma_0)}{\omega}$ as ω approaches zero as defined in Shivers et al. (Eq. 2.5) [2].

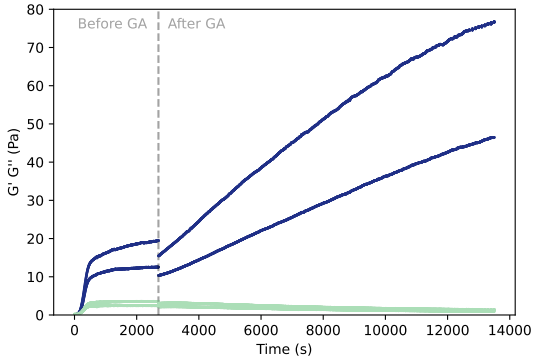

Figure A.22: Polymerization of 2 mg/mL atelocollagen network at 37^{o}C with crosslinking agent glutaraldehyde GA. The storage G' (dark blue) and loss modulus G'' (light green) is plotted as a function of time. 0.001% w/v of GA in 1X PBS is added around the cone head after 45 minutes of polymerization, and the G' and G'' is monitored for another 3 hours. Each line represents a single sample.

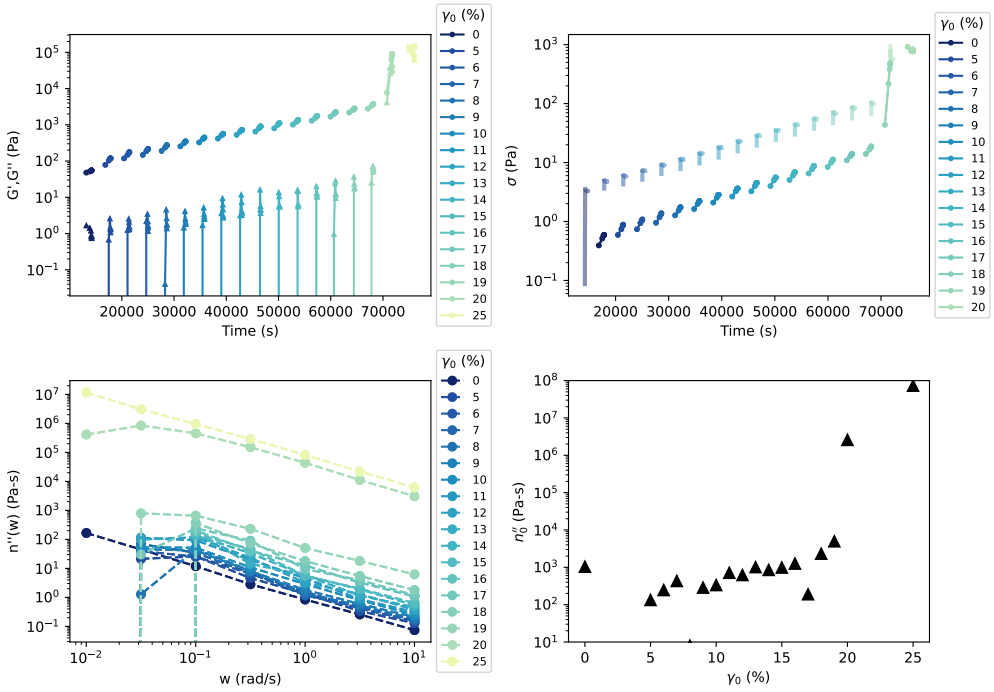

Figure A.23: Pre-strain frequency sweep test with 0.001% GA-crosslinked 2 mg/mL atelocollagen network polymerized at 37°C. The pre-strain frequency sweep test in Figure 2.6e is carried out. One representative sample is depicted. Colors represent the pre-strain value γ_0. The storage G', loss G" modulus and stress σ is plotted as a function of time. The zero-shear viscosity $\eta_0''(\gamma_0)$ is determined as the limit of dynamic viscosity $\eta''(\omega, \gamma_0) = \frac{G''(\omega,\gamma_0)}{\omega}$ as ω approaches zero as defined in Shivers et al. (Eq. 2.5) [2].

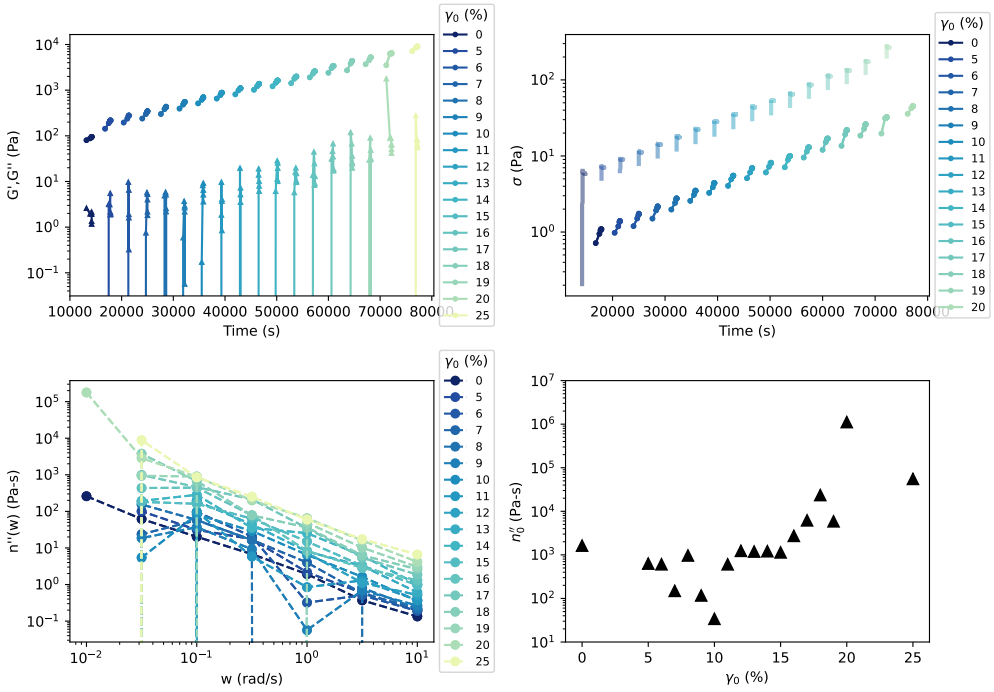

Figure A.24: Pre-strain frequency sweep test with 0.001% GA-crosslinked 2 mg/mL atelocollagen network polymerized at 37°C. The pre-strain frequency sweep test in Figure 2.6e is carried out. One representative sample is depicted. Colors represent the pre-strain value γ_0. The storage G', loss G" modulus and stress σ is plotted as a function of time. The zero-shear viscosity $\eta_0''(\gamma_0)$ is determined as the limit of dynamic viscosity $\eta''(\omega, \gamma_0) = \frac{G''(\omega,\gamma_0)}{\omega}$ as ω approaches zero as defined in Shivers et al. (Eq. 2.5) [2].

A.8. Pre-strain stress relaxation test

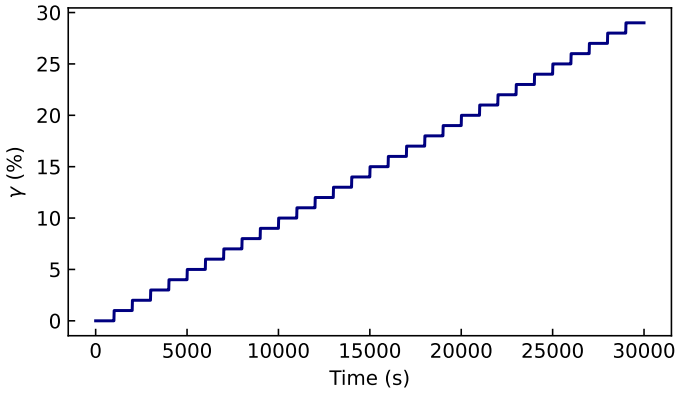

Figure A.25: Pre-strain stress relaxation test implementation. The stress-relaxation test proposed by Shivers et al. [2], is carried out at step-wise increasing pre-strain values γ_0 surrounding the critical strain. Each γ_0 is held for 1000s, during which the stress relaxation curve is recorded.

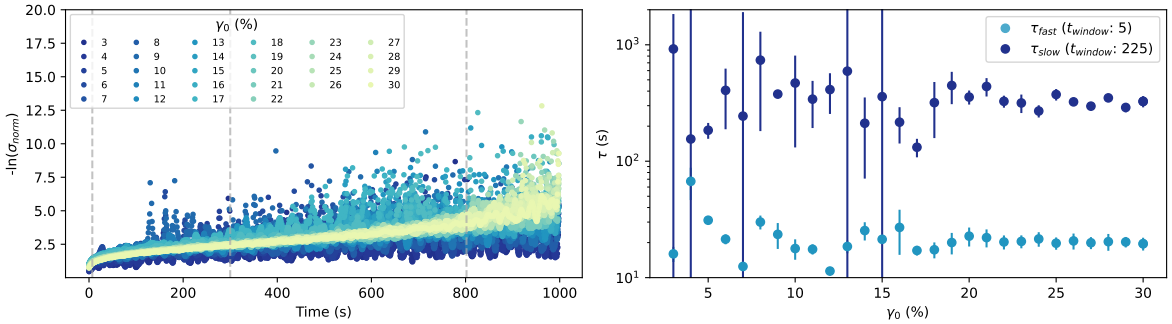

Figure A.26: Pre-strain stress relaxation test with 2 mg/mL atelocollagen network polymerized at 37^{o}C. One representative sample is depicted. The stress-relaxation curve is obtained at every γ_0. We compute the normalized stress difference $\sigma_{norm.}$ as $\sigma_{norm.} = \delta\sigma(t) - \delta\sigma_\infty/\delta\sigma(0)$, where $\delta\sigma_\infty \approx \delta\sigma(1000s)$ [2]. On the left, we plot the $-ln(\sigma_{norm.})$ as a function of time. The reciprocal of the slope of this curve is equal to the relaxation time τ. As the stress in the system tends to decay with multiple relaxation times, the log-linear plot is not completely straight. τ_{fast} dominates the initial response, and the slowest relaxation time τ_{slow} dominates the terminal region of the curve. On the right, we plot the τ_{fast} and τ_{slow} as a function of γ_0. τ_{fast} is computed as the average of the linear fits to the points from t=0s to t=7s with a sliding window size of $t_{window} = 5$s. The τ_{slow} is computed as the average of the linear fits to the datapoints between t=300s and t=800s, with a sliding window size of $t_{window} = 225$s. The error bars represent the standard deviation. Because of noise in the data, it is difficult to obtain reliable fits.

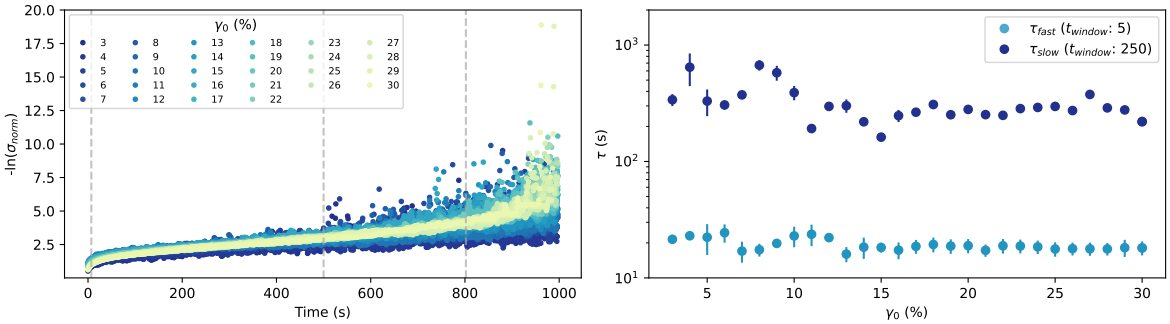

Figure A.27: Pre-strain stress relaxation test with 2 mg/mL atelocollagen network polymerized at 37^{o}C. One representative sample is depicted. The stress-relaxation curve is obtained at every γ_0. We compute the normalized stress difference $\sigma_{norm.}$ as $\sigma_{norm.} = \delta\sigma(t) - \delta\sigma_\infty / \delta\sigma(0)$, where $\delta\sigma_\infty \approx \delta\sigma(1000)$. On the left, we plot the $-ln(\sigma_{norm.})$ as a function of time. The reciprocal of the slope of this curve is equal to the relaxation time τ. As the stress in the system tends to decay with multiple relaxation times, the log-linear plot is not completely straight. τ_{fast} dominates the initial response, and the slowest relaxation time τ_{slow} dominates the terminal region of the curve. On the right, we plot the τ_{fast} and τ_{slow} as a function of γ_0. τ_{fast} is computed as the average of the linear fits to the points from t=0s to t=7s with a sliding window size of $t_{window} = 5$s. The τ_{slow} is computed as the average of the linear fits to the datapoints between t=500s and t=800s, with a sliding window size of $t_{window} = 250$s. The error bars represent the standard deviation. Because of noise in the data, it is difficult to obtain reliable fits.

A.9. Preliminary trials with the rheo-confocal setup

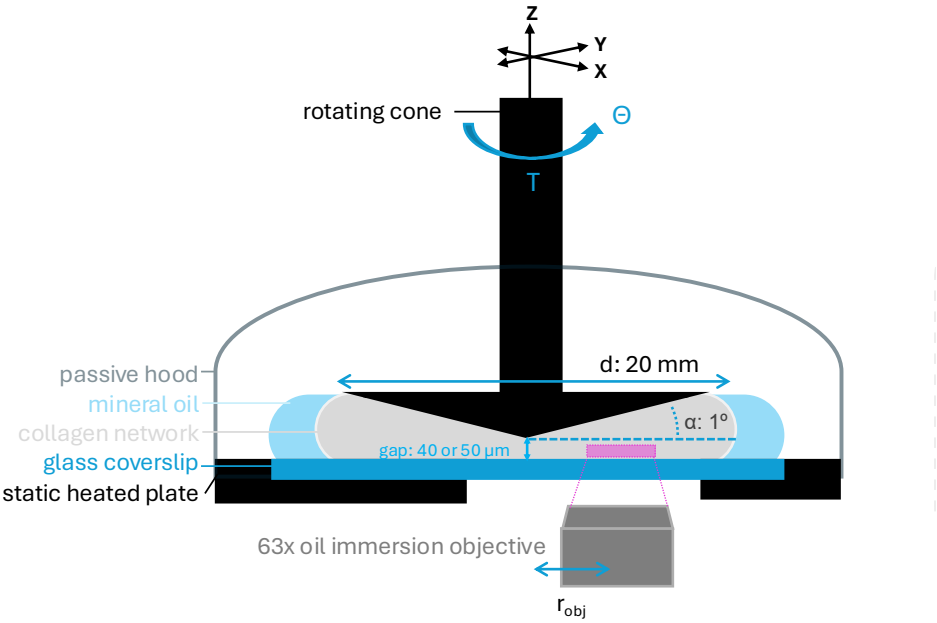

Figure A.28: Schematic of the rheo-confocal setup with a cone-head and bottom glass coverslip geometry (cone angle $\alpha = 1^o$, diameter $d = 20mm$). The collagen network polymerizes *in situ* between the cone head and the glass coverslip. The gap in the heated bottom plate allows the objective lens, positioned r_{obj} off the cone-head rotation axis, to image the collagen network through the glass coverslip.

A.9.1. Method

The rheo-confocal setup consists of a DSR-502 Anton Paars head mounted on the LSM 710 (Zeiss Observer Z.1 inverted microscope) with a heated bottom plate (Figure A.28). The bottom heated Peltier plate is removed to screw the 63x oil immersion objective lens (Zeiss, Plan-APOCHROMAT NA 1.4) onto the microscope. The Peltier plate is screwed back on, and several drops of immersion oil (Zeiss, 518 F) are applied over the objective lens through the hole in the Peltier plate. A glass coverslip,centered with the rheometer head, is fixed onto the Peltier plate by applying glue to fully cover its edges. The glue is left to dry for ten minutes. The stainless-steel rheometer cone head with an angle of 1^o and diameter of 20 mm (part no. 3274, serial no. 16798) is inserted into the rheometer, and the XY position of the head is adjusted with the side knob such that 0 is aligned with 5 mm on the knob. The zero gap is manually set by moving the head down until it makes contact with the coverslip, and the normal force reads 0.1 N. The inertia and motor check are carried out on the rheometer. Image settings are adjusted on the imaging computer using the ZEN software. For confocal fluorescence imaging, the 514 nm laser line is used with the MBS 458/514 excitation filter, and emission in the range of 515-797 nm is collected. The exact image acquisition settings used are described in more detail in the caption (Appendix A.30,A.32,A.34). The rheology protocol is set with the Rheoplus software on the computer connected to the rheometer. Fluorescently labeled collagen networks are prepared as described in Appendix A.1 and in Chapter 2 2.2.2.1, and 40 µL of sample is pipetted onto the glass coverslip, centered with the rheometer head. The head is manually moved to the gap position (40 µm) and mineral oil is added around the sample to

prevent evaporation. The sample is enclosed with the hood, and it is double-checked to make sure there is no contact of the hood with the rheometer head. The inside of the hood is lined with wet tissue to maintain a humid environment. The rheometer measurement and imaging are started at the same time after sample preparation. As in Chapter 2, the polymerization of the sample is monitored by applying small oscillatory strain of amplitude dγ=1% to the sample and measuring the storage G' and loss G" modulus. After complete polymerization of the sample (G' and G" reaches a plateau value), the stress ramp at the loading rate of $\dot{\sigma} = 0.1$ Pa/s (Figure 2.6c) and timelapse imaging are carried out at the same time until sample rupture. For each new sample, the rheometer head and the previous glass coverslip is removed and a new coverslip is glued in place. The zero gap setting, inertia and motor check is carried out again after reinserting the rheometer cone head.

A.9.2. Preliminary trials

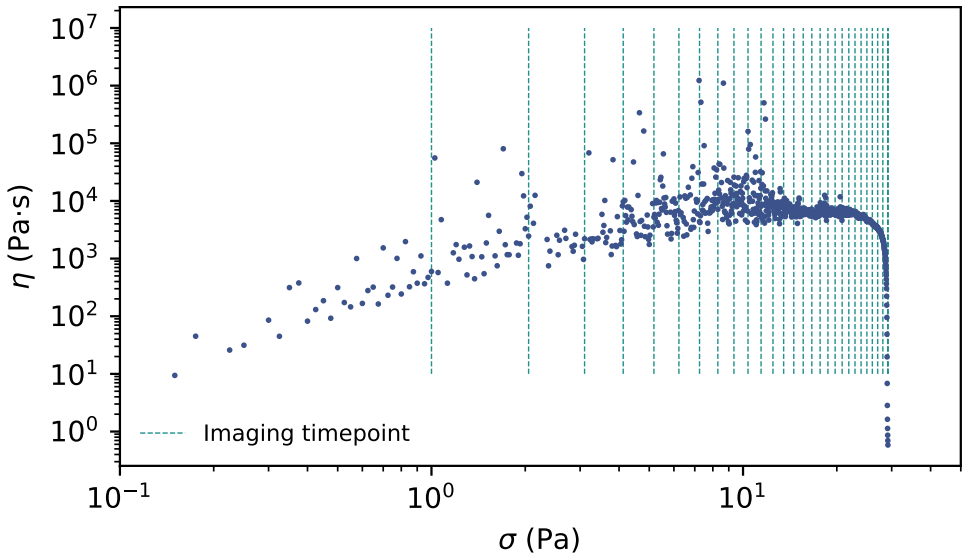

Figure A.29: Stress-controlled ramp is conducted at $\dot{\sigma} = 0.1$ Pa/s with a fluorescently-labeled 1.5 mg/mL atelocollagen network in the rheo-confocal setup. The labeled network consists of a 1:2 mass fraction of DyLight 550 labeled to unlabeled collagen monomers. The apparent viscosity η is plotted as a function of stress σ. Images are acquired every 10 s during the stress ramp (dashed line), and the corresponding image montage is shown in Figure A.30.

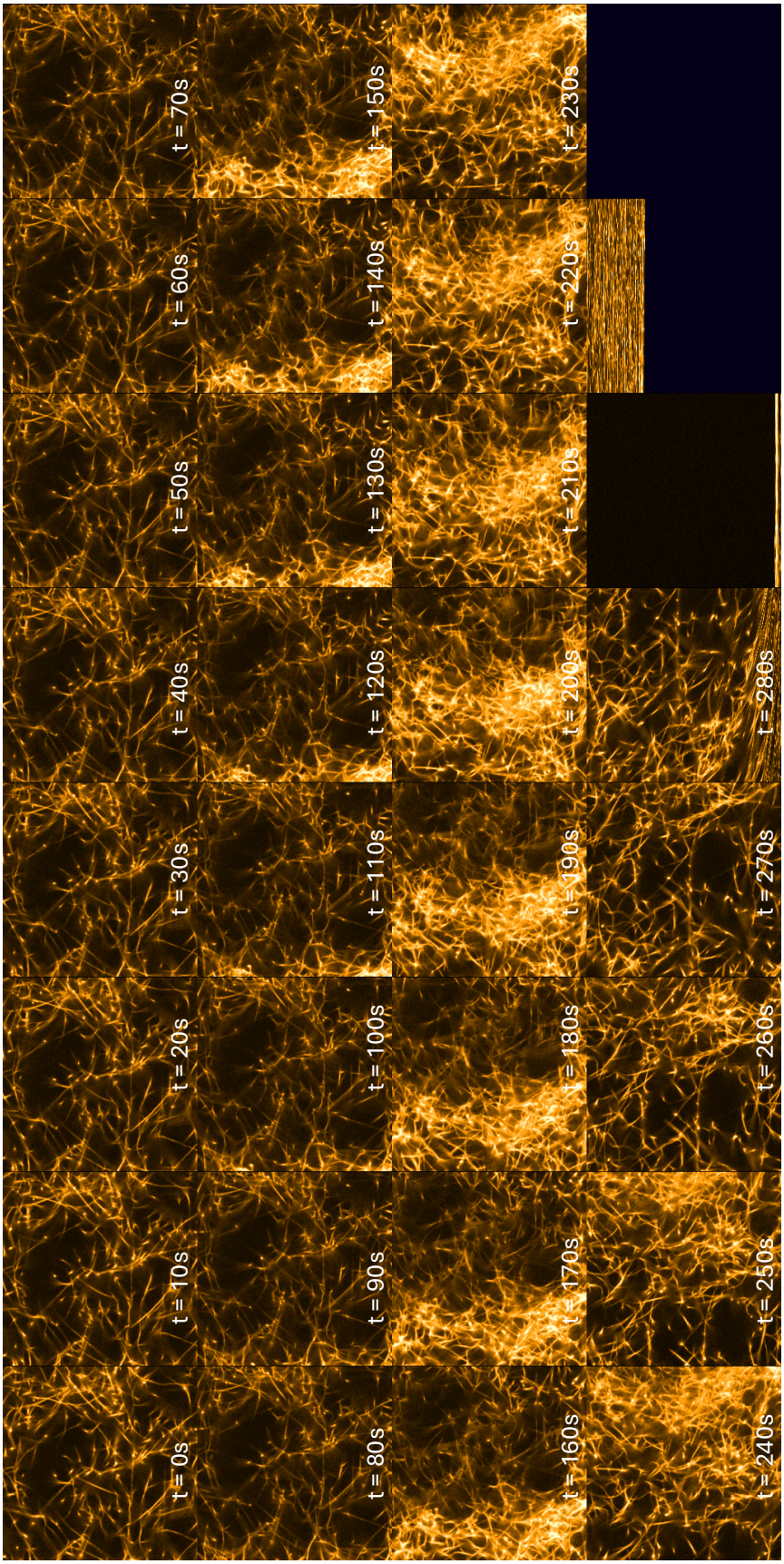

Figure A.30: Montage of 2D timelapse images of a fluorescently-labeled 1.5 mg/mL atelocollagen network during the stress-controlled ramp at $\dot{\sigma} = 0.1$ Pa/s in the rheo-confocal setup. The labeled network consists of a 1:2 mass fraction of DyLight 550 labeled to unlabeled collagen monomers. The field of view is 50x50 µm with a pixel size of 0.2 µm. The laser scanning speed of 4 results in frame acquisition time of 7.71s and the laser power of 25% is used. The corresponding viscosity η and stress σ of the sample at each time point is shown in A.29.

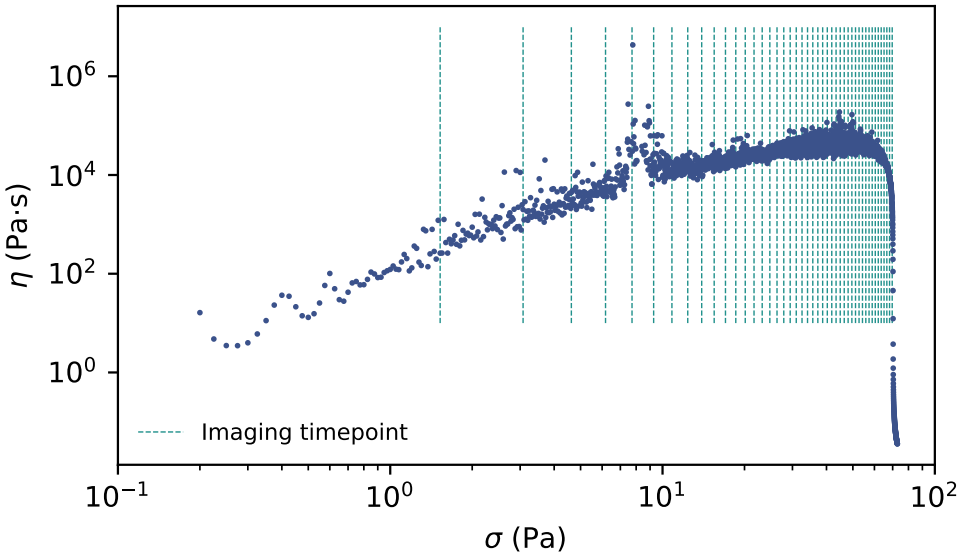

Figure A.31: Stress-controlled ramp at $\dot{\sigma} = 0.1$ Pa/s with a fluorescently-labeled 1.5 mg/mL atelocollagen network in the rheo-confocal setup. The labeled network consists of a 1:2 mass fraction of DyLight 550 labeled to unlabeled collagen monomers. The apparent viscosity η is plotted as a function of stress σ. Images are acquired every 15 s during the stress ramp (dashed line), and the corresponding image montage is shown in Figure A.32.

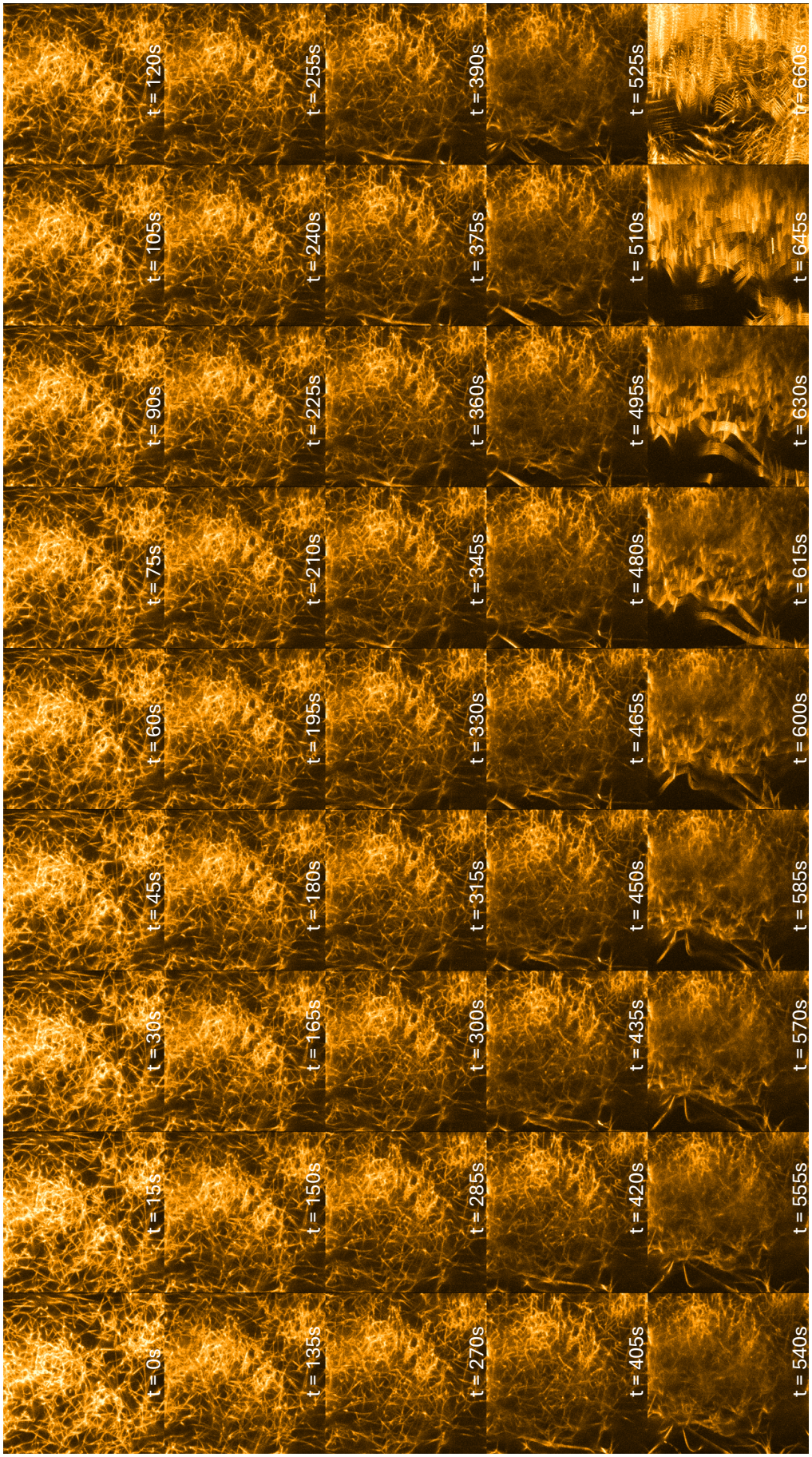

Figure A.32: Montage of 3D timelapse images of a fluorescently-labeled 1.5 mg/mL atelocollagen network during the stress-controlled ramp at $\dot{\sigma} = 0.1$ Pa/s in the rheo-confocal setup. The labeled network consists of a 1:2 mass fraction of DyLight 550 labeled to unlabeled collagen monomers. The field of view shown is the maximum intensity z-projection of the 3D image (dimensions are 50 x 50 x 2 µm with a voxel size of 0.2 x 0.2 x 0.18 µm), which is acquired every 15s. The laser scanning speed of 7 and the laser power of 25% is used. The corresponding viscosity η and stress σ of the sample at each time point is shown in A.31.

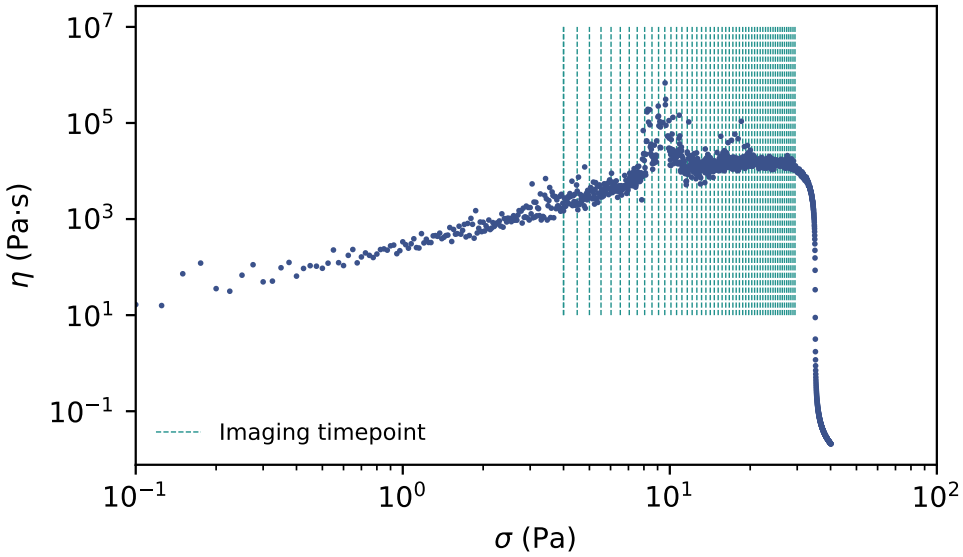

Figure A.33: Stress-controlled ramp at $\dot{\sigma} = 0.1$ Pa/s with a fluorescently-labeled 1.5 mg/mL atelocollagen network in the rheo-confocal setup. The labeled network consists of a 1:2 mass fraction of DyLight 550 labeled to unlabeled collagen monomers. The apparent viscosity η is plotted as a function of stress σ. Images are acquired every 5 s during the stress ramp (dashed line), and the corresponding image montage is shown in Figure A.34.

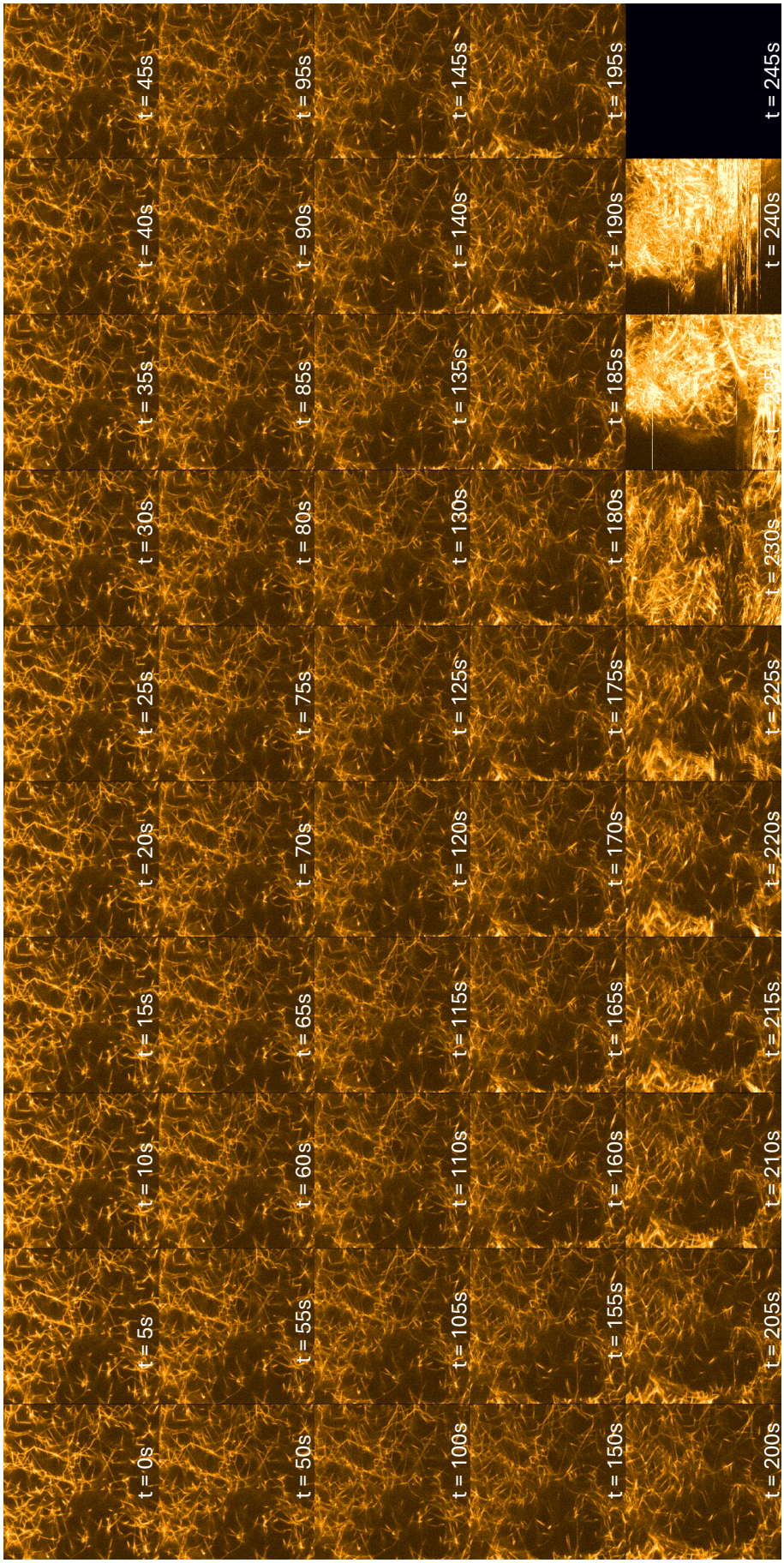

Figure A.34: Montage of 3D timelapse images of a fluorescently-labeled 1.5 mg/mL atelocollagen network during the stress-controlled ramp at $\dot{\sigma} = 0.1$ Pa/s in the rheo-confocal setup. The labeled network consists of a 1:2 mass fraction of DyLight 550 labeled to unlabeled collagen monomers. The field of view shown is the maximum intensity z-projection of the 3D image (dimensions are 50 x 50 x 2 µm with a voxel size of 0.2 x 0.2 x 0.46 µm), which is acquired every 5s. The laser scanning speed of 7 and the laser power of 25% is used. The corresponding viscosity η and stress σ of the sample at each time point is shown in A.33.